

AD-A256 187



WL-TR-92-3041

UNIFORM ROUGHNESS STUDIES

D.E. KLETT
M. KITHCART

Mechanical Engineering Department
North Carolina Agricultural and Technical State University
Greensboro, North Carolina 27411

May 1992

Final Report for Period September 1987 to March 1992

Approved for public release; distribution is unlimited.

DTIC
ELECTE
OCT 16 1992
S A D

FLIGHT DYNAMICS DIRECTORATE
WRIGHT LABORATORY
AIR FORCE SYSTEMS COMMAND
WRIGHT-PATTERSON AIR FORCE BASE, OHIO 45433-6553



92 10 13 129

444914

92-27275



830x

NOTICE

When Government drawings, specifications, or other data are used for any purpose other than in connection with a definitely Government-related procurement, the United States Government incurs no responsibility or any obligation whatsoever. The fact that the government may have formulated or in any way supplied the said drawings, specifications, or other data, is not to be regarded by implication, or otherwise in any manner construed, as licensing the holder, or any other person or corporation; or as conveying any rights or permission to manufacture, use, or sell any patented invention that may in any way be related thereto.

This report is releasable to the National Technical Information Service (NTIS). At NTIS, it will be available to the general public, including foreign nations.

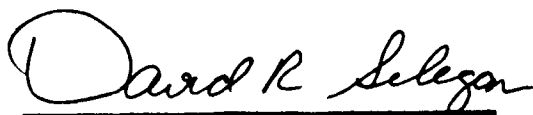
This technical report has been reviewed and is approved for publication.



EDMUND BROWN-EDWARDS
WL/FIMGB



VALENTINE DAHLEM, Chief
High Speed Aero Performance Branch
Aeromechanics Division



DAVID R. SELEGAN, Actg Chief
Aeromechanics Division
Flight Dynamics Directorate

If your address has changed, if you wish to be removed from our mailing list, or if the addressee is no longer employed by your organization please notify WL/FIMG, WPAFB, OH 45433-6553 to help us maintain a current mailing list.

Copies of this report should not be returned unless return is required by security considerations, contractual obligations, or notice on a specific document.

REPORT DOCUMENTATION PAGE			Form Approved OMB No. 0704-0188	
Public reporting burden for this collection of information is estimated to average 1 hour per response, including the time for reviewing instructions, searching existing data sources, gathering and maintaining the data needed, and completing and reviewing the collection of information. Send comments regarding this burden estimate or any other aspect of this collection of information, including suggestions for reducing this burden, to Washington Headquarters Services, Directorate for Information Operations and Reports, 1215 Jefferson Davis Highway, Suite 1204, Arlington, VA 22202-4302, and to the Office of Management and Budget, Paperwork Reduction Project (0704-0188), Washington, DC 20503.				
1. AGENCY USE ONLY (Leave blank)		2. REPORT DATE May 1992	3. REPORT TYPE AND DATES COVERED Final 30 Sep 87 to 20 Mar 92	
4. TITLE AND SUBTITLE Uniform Roughness Studies			5. FUNDING NUMBERS C - F33615-C-87-3022 PE - 62201F PR - 2404 TA - 07 WU - A6	
6. AUTHOR(S) D.E. Klett M. Kithcart				
7. PERFORMING ORGANIZATION NAME(S) AND ADDRESS(ES) Mechanical Engineering Department North Carolina Agricultural and Technical State University Greensboro NC 27411			8. PERFORMING ORGANIZATION REPORT NUMBER	
9. SPONSORING / MONITORING AGENCY NAME(S) AND ADDRESS(ES) Edmund G. Brown-Edwards (513-255-2052) Flight Dynamics Directorate (WL/FIMG) Wright Laboratory Wright-Patterson AFB OH 45433-6553			10. SPONSORING / MONITORING AGENCY REPORT NUMBER WL-TR-92-3041	
11. SUPPLEMENTARY NOTES				
12a. DISTRIBUTION / AVAILABILITY STATEMENT Approved for public release, distribution is unlimited.			12b. DISTRIBUTION CODE	
13. ABSTRACT (Maximum 200 words) Heat transfer, skin friction, turbulence intensity, and velocity profile data were obtained for 22 different rough surfaces in turbulent subsonic boundary layer air flow. The rough surfaces consisted of hemispherical dimples, hemispherical protrusions, and rectangular protrusions. The rectangular roughness plates were tested with the tops of the elements flush with the upstream smooth surface and with the tops protruding above the smooth surface. The surfaces with protrusions were designed to have values of the Simpson roughness shape/spacing parameter that bracket the peak in the equivalent sand-grain correlation. The data was used for comparison with predictions from a discrete element rough surface boundary layer code in an attempt to improve the code's performance for cases of closely spaced roughness elements when wakes behind individual elements overlap. An anomaly was discovered in the code that causes wide variations in predicted drag and heat transfer for small variations in element drag coefficient Cd. The problem lies in the effect of Cd on the velocity calculation giving rise to inflections in the calculated velocity profile near the crests of the roughness elements. A remedy to the problem has not, as yet, been found.				
14. SUBJECT TERMS Turbulent Boundary Layer Machined Roughness Subsonic			15. NUMBER OF PAGES 79	
			16. PRICE CODE	
17. SECURITY CLASSIFICATION OF REPORT UNCLASSIFIED	18. SECURITY CLASSIFICATION OF THIS PAGE UNCLASSIFIED	19. SECURITY CLASSIFICATION OF ABSTRACT UNCLASSIFIED	20. LIMITATION OF ABSTRACT UL	

GENERAL INSTRUCTIONS FOR COMPLETING SF 298

The Report Documentation Page (RDP) is used in announcing and cataloging reports. It is important that this information be consistent with the rest of the report, particularly the cover and title page. Instructions for filling in each block of the form follow. It is important to *stay within the lines* to meet optical scanning requirements.

Block 1. Agency Use Only (Leave blank).

Block 2. Report Date. Full publication date including day, month, and year, if available (e.g. 1 Jan 88). Must cite at least the year.

Block 3. Type of Report and Dates Covered.

State whether report is interim, final, etc. If applicable, enter inclusive report dates (e.g. 10 Jun 87 - 30 Jun 88).

Block 4. Title and Subtitle. A title is taken from the part of the report that provides the most meaningful and complete information. When a report is prepared in more than one volume, repeat the primary title, add volume number, and include subtitle for the specific volume. On classified documents enter the title classification in parentheses.

Block 5. Funding Numbers. To include contract and grant numbers; may include program element number(s), project number(s), task number(s), and work unit number(s). Use the following labels:

C - Contract	PR - Project
G - Grant	TA - Task
PE - Program Element	WU - Work Unit Accession No.

Block 6. Author(s). Name(s) of person(s) responsible for writing the report, performing the research, or credited with the content of the report. If editor or compiler, this should follow the name(s).

Block 7. Performing Organization Name(s) and Address(es). Self-explanatory.

Block 8. Performing Organization Report Number. Enter the unique alphanumeric report number(s) assigned by the organization performing the report.

Block 9. Sponsoring/Monitoring Agency Name(s) and Address(es). Self-explanatory.

Block 10. Sponsoring/Monitoring Agency Report Number (If known)

Block 11. Supplementary Notes Enter information not included elsewhere such as: Prepared in cooperation with...; Trans. of...; To be published in... When a report is revised, include a statement whether the new report supersedes or supplements the older report.

Block 12a. Distribution/Availability Statement. Denotes public availability or limitations. Cite any availability to the public. Enter additional limitations or special markings in all capitals (e.g. NOFORN, REL, ITAR).

DOD - See DoDD 5230.24, "Distribution Statements on Technical Documents."

DOE - See authorities.

NASA - See Handbook NHB 2200.2.

NTIS - Leave blank.

Block 12b. Distribution Code.

DOD - Leave blank.

DOE - Enter DOE distribution categories from the Standard Distribution for Unclassified Scientific and Technical Reports.

NASA - Leave blank.

NTIS - Leave blank.

Block 13. Abstract. Include a brief (*Maximum 200 words*) factual summary of the most significant information contained in the report.

Block 14. Subject Terms. Keywords or phrases identifying major subjects in the report.

Block 15. Number of Pages. Enter the total number of pages.

Block 16. Price Code. Enter appropriate price code (*NTIS only*).

Blocks 17. - 19. Security Classifications. Self-explanatory. Enter U.S. Security Classification in accordance with U.S. Security Regulations (i.e., UNCLASSIFIED). If form contains classified information, stamp classification on the top and bottom of the page.

Block 20. Limitation of Abstract. This block must be completed to assign a limitation to the abstract. Enter either UL (unlimited) or SAR (same as report). An entry in this block is necessary if the abstract is to be limited. If blank, the abstract is assumed to be unlimited.

TABLE OF CONTENTS

List of Figures	iv
List of Tables	viii
Acknowledgements	ix
Nomenclature	x
Summary	1
Introduction	2
Description Of The Experiment	6
Results and Discussion	12
Rough Surface Boundary Layer Code	16
Summary	24
References	26
Appendix A (Literature Review)	29
Figures	38

Accession For	
NTIS CRA&I	<input checked="" type="checkbox"/>
DTIC TAB	<input type="checkbox"/>
Unannounced	<input type="checkbox"/>
Justification	
By	
Distribution /	
Availability Codes	
Dist	Avail and/or Special
A-1	

DTIC QUALITY INSPECTED 1

LIST OF FIGURES

Fig. No.	Page
1. Schematic of Wind Tunnel and Drag Balance	38
2. Calibration Method for Drag Balance	39
3. Location of Thermocouples in Test Plate	40
4. Schematic of Hemispherically Dimpled Plates	41
5. Schematic of Rectangular Roughness Plates	42
6. Velocity Profiles on Smooth Test Plate	43
7. Turbulence Profiles on Smooth Test Plate	43
8. Smooth Plate Drag, Comparison of Measured Vs Predicted	43
9. Smooth Plate Stanton Number Measurement	43
10. Cd for Dimpled Plates	44
11. Drag Augmentation for Dimpled Roughness	44
12. Stanton Number for Dimpled Roughness	44
13. Heat Transfer Augmentation for Dimpled Roughness	44
14. Resistance Coefficient of Circular Cavities of Varying Depth in a Flat Plate as Measured by Wieghardt	45
15. Velocity Profiles for Plate D1	46
16. Turbulence Profiles for Plate D1	46
17. Velocity Profiles for Plate D2	46
18. Turbulence Profiles for Plate D2	46
19. Velocity Profiles for Plate D3	47
20. Turbulence Profiles for Plate D3	47
21. Velocity Profiles for Plate D4	47
22. Turbulence Profiles for Plate D4	47
23. Velocity Profiles for Plate D5	48
24. Turbulence Profiles for Plate D5	48
25. Velocity Profiles for Plate D6	48
26. Turbulence Profiles for Plate D6	48
27. Velocity Profiles for Plate D7	49
28. Turbulence Profiles for Plate D7	49
29. Velocity Profiles for Plate D8	49

LIST OF FIGURES CONTINUED

Fig. No.	Page
30. Turbulence Profiles for Plate D8	49
31. Comparison of Velocity Profiles at Rear of Plates D4 and D5	50
32. Comparison of Velocity Profiles at Rear of Dimpled Roughness Plates	50
33. Comparison of Turbulence Profiles at Rear of Dimpled Roughness Plates ..	50
34. Drag Augmentation for Hemispherical Roughness	51
35. Heat Transfer Augmentation for Hemispherical Roughness	51
36. Velocity Profiles for Plate H1	52
37. Turbulence Profiles for Plate H1	52
38. Velocity Profiles for Plate H2	52
39. Turbulence Profiles for Plate H2	52
40. Velocity Profiles for Plate H3	53
41. Turbulence Profiles for Plate H3	53
42. Velocity Profiles for Plate H4	53
43. Turbulence Profiles for Plate H4	53
44. Velocity Profiles for Plate H5	54
45. Turbulence Profiles for Plate H5	54
46. Velocity Profiles for Plate H6	54
47. Turbulence Profiles for Plate H6	54
48. Velocity Profiles for Plate H7	55
49. Turbulence Profiles for Plate H7	55
50. Velocity Profiles for Plate H8	55
51. Turbulence Profiles for Plate H8	55
52. Comparison of Vel. Prof. at Rear of Hemispherical Roughness Plates	56
53. Comparison of Turb. Prof. at Rear of Hemispherical Roughness Plates	56
54. Drag Augmentation for Rectangular Roughness	57
55. Heat Transfer Augmentation for Rectangular Roughness	57
56. Vel. Prof. for Plate R1 with the Elements Flush with the BL Plate	58
57. Turb. Prof. for Plate R1 with the Elements Flush with the BL Plate	58
58. Vel. Prof. for Plate R1 with the Elements Above the BL Plate	58
59. Turb. Prof. for Plate R1 with the Elements Above the BL Plate	58

LIST OF FIGURES CONTINUED

Fig. No.	Page
60. Vel. Prof. for Plate R2 with the Elements Flush with the BL Plate	59
61. Turb. Prof. for Plate R2 with the Elements Flush with the BL Plate	59
62. Vel. Prof. for Plate R2 with the Elements Above the BL Plate	59
63. Turb. Prof. for Plate R2 with the Elements Above the BL Plate	59
64. Vel. Prof. for Plate R3 with the Elements Flush with the BL Plate	60
65. Turb. Prof. for Plate R3 with the Elements Flush with the BL Plate	60
66. Vel. Prof. for Plate R3 with the Elements Above the BL Plate	60
67. Turb. Prof. for Plate R3 with the Elements Above the BL Plate	60
68. Vel. Prof. for Plate R4 with the Elements Flush with the BL Plate	61
69. Turb. Prof. for Plate R4 with the Elements Flush with the BL Plate	61
70. Vel. Prof. for Plate R4 with the Elements Above the BL Plate	61
71. Turb. Prof. for Plate R4 with the Elements Above the BL Plate	61
72. Vel. Prof. for Plate R5 with the Elements Flush with the BL Plate	62
73. Turb. Prof. for Plate R5 with the Elements Flush with the BL Plate	62
74. Vel. Prof. for Plate R5 with the Elements Above the BL Plate	62
75. Turb. Prof. for Plate R5 with the Elements Above the BL Plate	62
76. Vel. Prof. for Plate R6 with the Elements Flush with the BL Plate	63
77. Turb. Prof. for Plate 66 with the Elements Flush with the BL Plate	63
78. Vel. Prof. for Plate R6 with the Elements Above the BL Plate	63
79. Turb. Prof. for Plate R6 with the Elements Above the BL Plate	63
80. Comparison of Vel. Prof. at Rear of Rectangular Roughness Plates with the Elements Flush with the Boundary Layer Plate	64
81. Comparison of Vel. Prof. at Rear of Rectangular Roughness Plates with the Elements Above the Boundary Layer Plate	64
82. Comparison of Turb. Prof. at Rear of Rectangular Roughness Plates with the Elements Flush with the Boundary Layer Plate	65
83. Comparison of Turb. Prof. at Rear of Rectangular Roughness Plates with the Elements Above the Boundary Layer Plate	65
84. Comparison of Measured and Predicted Drag Using the Original TCH Cd Correlation	66
85. Comparison of Measured and Predicted Heat Transfer Using the Original TCH Nusselt No. Correlation	66

LIST OF FIGURES CONTINUED

Fig. No.	Page
86. Comparison of Measured and Predicted Drag Force Using Eqn (4) and Variable Initial Step Size	67
87. Comparison of Measured and Predicted Heat Transfer Using Eqn (5) and Variable Initial Step Size	67
88. Variation of Predicted Drag with Constant Cd Value	68
89. Velocity Profiles Predicted with ROUGH Near Front of Plate	68
90. Definition of Dimensions for Square Roughness Elements	69
A1. The Effect of Roughness Density on the Law of the Wall Intercept	69
A2. Simpson's Equivalent Sand-Grain Correlation	70
A3. Dirling's Equivalent Sand-Grain Correlation	70

LIST OF TABLES

Table No.	Page
1. Parameters for Dimpled Roughness Plates	11
2. Parameters for Hemispherical Roughness Plates	11
3. Parameters for Rectangular Roughness Plates	11

ACKNOWLEDGMENT

This work was supported by U. S. Air Force Contract No. F33615-87-C-3022. D. E. Klett was the principal investigator and Mark Kithcart served as research assistant on the project. Dr. Edmund G. Brown-Edwards of the Flight Dynamics Directorate, Wright Laboratory, served as the program Technical Monitor. The authors would like to express their appreciation to Dr. Brown-Edwards for his assistance, encouragement and patience during the duration of this project.

NOMENCLATURE

A	Boundary layer profile constant
A_e	Average roughness area
A_{fp}	Total hole footprint area of dimpled roughness plate
A_p	Roughness element projected frontal area
A_s	Total surface area of plate or total smooth area of plate
A_{ws}	Roughness element windward surface area
B	Boundary layer profile constant
C	Boundary layer profile constant
C_d	Local element drag coefficient
C_f	Local skin friction coefficient
\bar{C}_f	Total skin friction coefficient
D	Dimple roughness hole diameter
d	Dimple roughness depth
$d(y)$	Local roughness element diameter
F_d	Drag force on roughness element
k	Roughness height
k_s	Equivalent sand-grain roughness
l	roughness element spacing
L	Streamwise element spacing
l	Transverse element spacing
K	Thermal conductivity
Nu_d	Local element Nusselt number
Pr	Prandtl number
Q	Rate of heat transfer to/from a roughness element
Re	Freestream Reynolds number
Re_k	Roughness Reynolds number
Re_d	Local roughness Reynolds number
St	Stanton number
T	Fluid temperature
T_R	Roughness element temperature
u	Streamwise velocity component
U	Freestream velocity

u_*	Friction velocity, $\sqrt{\tau_0/\rho}$
$\Delta U/u_*$	Downward shift in velocity profile
V	Volts
W	Width
x	Streamwise coordinate
y	Normal coordinate
α	Flow blockage coefficient
K	Von Karman constant ≈ 0.40
δ_*	Boundary layer displacement thickness
λ	Dirling roughness density parameter
λ_k	Simpson roughness density parameter $= A_s/A_p$
ν	Kinematic viscosity
ρ	Density
τ_0	Wall shear stress

SUMMARY

Heat transfer, skin friction, turbulence intensity, and velocity profile data were obtained for 22 different rough surfaces in turbulent subsonic boundary layer air flow, with freestream Reynolds Numbers up to 2,000,000. The rough surfaces consisted of hemispherical dimples, hemispherical protrusions, and rectangular protrusions. The rectangular roughness plates were tested as both "d" and "k" type surfaces, i.e., with the tops of the elements flush with the upstream smooth surface and protruding above the smooth surface, respectively. The surfaces with protrusions were designed to have values of the Simpson roughness shape/spacing parameter that bracket the peak in the equivalent sand-grain correlation. The data was used for comparison with predictions from the Taylor, Coleman, Hodge discrete element rough surface boundary layer code in an attempt to improve the code's performance for cases of closely spaced roughness elements when wakes behind individual elements overlap. An anomaly was discovered in the code that causes wide variations in predicted drag and heat transfer for small variations in element drag coefficient C_d . The problem lies in the effect of C_d on the velocity calculation giving rise to inflections in the calculated velocity profile near the crests of the roughness elements. A remedy to the problem has not, as yet, been found and the code should not be used for design purposes for cases that approximate the roughness geometries tested here.

INTRODUCTION

This report describes the results of a series of measurements of flow parameters for fully-rough turbulent boundary layer flow of air over flat test plates roughened with three-dimensional roughness elements of three different types; hemispherical dimples, hemispherical protrusions and rectangular parallelepiped protrusions. The parameters measured included total skin friction, total Nusselt and Stanton numbers, and velocity and turbulence profiles at several locations over the test plates. The report also describes attempts to improve an existing discrete element, rough surface boundary layer code developed by Taylor, Coleman and Hodge in 1984 (ref 1).

The objective of the work was to add to the existing data base for rough surface boundary layer flow, particularly for flow over closely-spaced uniform roughness, and to utilize this data to improve the code to allow better predictions of skin friction and drag for cases of closely-spaced roughness elements when wakes from individual elements overlap and interact. A brief historical background of the development of rough surface boundary layer calculations is presented below. A more detailed treatment of this development is provided in the Appendix for the interested reader.

The effect of surface roughness on fluid flow parameters such as friction and heat transfer has been a major topic of study in the field of fluid dynamics. Beginning in the 1930's with the important experimental work of Nikuradse and Schlichting, whose primary concerns were the effects of rough walls on pipe flow resistance and drag on ship hulls, respectively, to the present, where knowledge of the effects of roughness is now applied to heat exchangers, turbine blades, re-entry vehicles, etc., the goal has always been to find methods which allow for the accurate prediction of flow parameters, but do not involve large investments of time and money.

Nikuradse (ref 2) performed the first detailed experimental study of rough wall turbulent flow by gluing sand grains of different uniform sizes to the inside walls of pipes in the most dense arrangement possible. By measuring the pressure drop of water flow through the roughened pipes, Nikuradse developed an empirical equation relating sand grain height, Reynold's number, and pipe diameter to the flow resistance.

Schlichting (ref 3) designed and built a channel flow test rig, in an effort to offer an alternative to the testing of ship hulls in towing tanks. Plates roughened with uniform, three-dimensional roughness of various geometric shapes were tested in turbulent, fully developed water flow. Using the data collected for each plate (friction coefficients and velocity profiles), Schlichting devised the "equivalent sand grain roughness" parameter, k_s , which allows one to obtain skin friction data (from a graph devised by Prandtl and Schlichting for rough flat plates) for non-sand-grain surface if the equivalent sand grain size is known. The work of Nikuradse and Schlichting provided the foundation for the development of rough-wall friction correlations, most notably those by Dvorak (ref 4), Dirling (ref 5), and Simpson (ref 6), which are discussed in more detail in the Appendix.

The first rough surface heat transfer experiments took place around 1911, but not until Cope's results in 1941 (ref 7) did any data show a discernible effect of roughness on heat transfer. Nunner (ref 8) in 1956 conducted the first in-depth study of air flow over 2-D roughness in pipes. In 1963 Owen and Thomson (ref 9) and Dipprey and Sabersky (ref 10) published the results of their respective experiments on rough wall heat transfer in tubes. Each group put forth similar hypotheses on the mechanism of heat transfer in the vicinity of a rough surface, stating that vortical flow in the regions between protrusions was responsible for increased convective activity. More recently, extensive research on rough, flat plate flow has been carried out by Betterman in 1966 (ref 11), Coleman (ref 12), Pimenta (ref 13), Healzer (ref 14), and Ligrani (ref 15) at Stanford University from 1974 to 1979, and by Hosni, Coleman, and Taylor in 1989 (ref 16).

With the advent of digital computers came the opportunity for fluid flow modeling and prediction with accuracy, speed and reduced cost, compared to the expense involved in experimental work. Previous to that time, correlations for prediction of roughness effects on boundary layer flow were based primarily on the work of Nikuradse and Schlichting, as mentioned earlier. Therefore, it is not surprising that in the absence of more definitive data, the first codes developed used these databases as their foundation.

One of the first widely known rough wall codes was developed by Dvorak (ref 4). Using a correlation he devised relating non-sand-grain roughness to a rough wall friction coefficient equation derived by Clauser (ref 17), Dvorak calculated boundary layer parameters (momentum thickness and shape factor) for rough surfaces using the momentum integral method. Also of note are the finite difference method codes created by Cebeci and Chang (ref 18), and Wilcox (ref 19). In these models, the effects of surface roughness are accounted for by specifying algebraic "boundary conditions" at the wall which implicitly include the sand grain parameter k_s . A drawback to this approach, however, along with that of Dvorak, is the fact that there can be no detailed description of the physical nature of the roughness, i.e., shape, spacing, etc. which, in light of Schlichting's experimental results, are important factors in understanding the effects of roughness on boundary layer flow.

Taking into consideration the concerns expressed above, many researchers have recently turned to the discrete element approach as a way of more accurately modeling, and therefore predicting, rough wall flows. This concept, as originally stated by Schlichting, involves taking into account the contribution of each roughness element, along with the smooth surface between elements, to the overall friction (or flow resistance) of a rough surface. This method is then useful as a way of predicting heat transfer also, since it allows for modeling of the fluid flow in the vicinity of the elements. Therefore, realistic convective boundary conditions can be prescribed, without resorting to analogies.

Finson (ref 20), followed by others such as Christoph (ref 21), and Hodge and Adams (ref22), were the first to incorporate a discrete element model into their respective rough wall boundary layer codes. However, these early models still relied on the equivalent sand grain parameter, k_s , as a means of describing roughness geometry and spacing. Subsequent work by Finson and Clarke (ref 23), Christoph and Pletcher (ref 24), and Taylor, Coleman and Hodge (ref 1) have resulted in models which allow for the input of actual element geometries and relative spacings. Taylor, Coleman and Hodge was the only group to calculate heat transfer without the use of an analogy between friction and heat transfer rate.

The one shortcoming of the discrete method is the requirement that correlations for form drag and convective coefficients are necessary for any rough surface made up of discrete elements, which has not already been tested experimentally and used in a database. This, therefore, limits both accuracy and the applicability of discrete method codes in prediction of rough wall flows. As an example, Taylor, Coleman and Hodge as well as Tarada (ref 25) as recently as 1990, have had only fair success in predicting flows over closely spaced uniform roughness, due mainly to the lack of data for these types of roughness configurations. The experiment described here was designed to add to the limited existing database in order to improve correlations used in discrete element boundary layer codes.

The following sections describe the experimental procedures and results and the efforts to modify the rough surface boundary layer code developed by Taylor, Coleman and Hodge.

DESCRIPTION OF THE EXPERIMENT

The equipment used in the experiment includes a 12-m (40-ft) long, open circuit, subsonic wind tunnel, with a 3.05-m \times 0.51-m \times 0.71-m (120-in \times 20-in \times 28-in) test section. The tunnel, manufactured by Aerolab, is equipped with a 50-hp variable speed drive, producing test section velocities from 0 to 40 m/s (132 ft/s). The test section has a flexible adjustable ceiling that was set to achieve a zero pressure gradient in the test section. Mounted in the test section is a 0.71-m (28-in) wide, 2.4-m (94-in) long boundary layer plate, made of 1.27-cm (0.5-in) thick plexiglas. The boundary layer plate is supported 5-cm (2-in) above the floor of the test section on aluminum channel stock. A 0.305-m \times .61-m (12-in \times 24-in) hole was cut in the boundary layer plate, on the centerline of the test section beginning 0.76-m (30-in) from the leading edge. Test plates were inserted in this hole flush with the upper surface of the boundary layer plate as shown in Figure 1.

At the leading edge of the boundary layer plate is the slot opening for the boundary layer suction system formed by the plate leading edge and an entrance ramp. This system was installed to create a new boundary layer starting at the leading edge of the boundary layer plate, and to eliminate the possibility of flow separation near the leading edge. The suction is provided by a high pressure blower driven by a 5 hp electric motor. The inlet of the blower is connected to the wind tunnel test section with a 15.24-cm (6-in) diameter flexible hose. Control of the rate of suction is accomplished by adjusting a manual gate valve installed between the blower inlet and the test section. Pressure taps on the boundary layer plate and near the entrance of the suction slot are connected to a digital differential pressure transducer. For a given velocity, the valve is adjusted until the difference in the pressures is ± 0.01 mpsi. When this is achieved, the velocities above and below the boundary layer plate are equal, and a dividing streamline is centered at the front edge of the boundary layer plate. The boundary layer developing on the floor of the tunnel contraction is removed by suction below the dividing streamline. A 1.6-mm (0.0625-in) diameter trip wire was installed on the boundary layer plate 5-cm (2-in) downstream of the suction

slot. The trip wire had to be removed before adjusting the slot suction rate for each new freestream velocity. The wire was then replaced prior to testing at the new velocity.

Mounted below the test section, enclosed in an air-tight plexiglas box, is an air bearing drag balance. A Dover model 100 air bearing, on which the test plates are mounted, is connected to a Kistler-Morse model DSC 6 deflection sensor, using a small chain (Fig. 2). The deflection sensor provides a voltage proportional to the magnitude of the drag force applied to the test plates. The voltage output of the deflection sensor is monitored with a digital voltmeter and a digital data acquisition system when skin friction measurements are being made. Calibration of the drag measuring apparatus is achieved using known forces applied to the drag balance by suspending weights on a thread in the manner shown in Figure 2. In this way, bias error can be eliminated from the drag measuring system before taking skin friction data. The drag balance was designed at NASA Langley, and is essentially the same device used by Bandyopadhyay (ref 26).

Six 12.7-cm x 17.8-cm (5-in x 7-in) rubber-encased electric heating pads were used to heat the test plates during heat transfer tests. The heating pads were placed between a sheet of 2.54-cm (1-in) thick polyisocyanurate insulation, and the test plate. Power was supplied to the heating pads by a 110-V variac, and was monitored by a digital voltmeter and an ammeter. Twelve 30-gage Type T thermocouples were installed in the test plates in holes drilled in the bottom of the plates to within 0.4-mm (0.015-in) of the top surface. Thermocouples were also installed at several locations on the bottom of the test plate and in the boundary layer plate adjacent to the test plate to provide temperature data for calculating bottom and edge heat losses. The locations of the thermocouples in the test plates are shown in Figure 3. The thermocouple measurement system was checked by placing the thermocouples in a boiling water bath before being installed in a test plate.

Initially, a 32-channel chart recorder was used to acquire temperature

data, but questionable accuracy during early runs prompted a change to an Omega model DP460 digital thermocouple indicator with 0.1°F resolution and a manual thermocouple switch. While this increased the labor involved in obtaining heat transfer data, the accuracy of the readings was improved. An infrared surface temperature system was also tried. The infrared sensor was mounted on the tunnel's traversing mechanism and could be remotely positioned at any point over the plate. The infrared sensor gave good agreement with simultaneous thermocouple readings, but the resolution of the infrared system was only 1°F due to limitations in the analog-to-digital processor used in the system. Attempts to improve the resolution were unsuccessful; therefore, thermocouples were used for all temperature measurements.

The average plate surface temperature was calculated from the readings of the twelve plate thermocouples. Radiative heat transfer from the top surface was calculated based on the average surface temperature. Edge and bottom conductive heat losses were calculated from the readings of the thermocouples placed for that purpose around the periphery of the plate. The convective heat transfer could then be determined from the power input to the heaters less the conductive and radiative losses. The Stanton number was then calculated from the convective heat transfer using the relation

$$St = \frac{Q}{\rho A C_p U (T_w - T_\infty)}$$

where Q is the convective heat transfer, T_w is the average plate surface temperature, T_∞ is the freestream temperature, ρ is the air density at the film temperature (average of T_w and T_∞), A is the plate surface area, C_p is the air specific heat and U is the freestream velocity.

The test plates were machined from aluminum stock, and all had dimensions of 30.32-cm x 60.80-cm x 1.27-cm (11.938-in x 23.938-in x 0.5-in). Four types of surfaces were tested, a smooth surface, and surfaces roughened with hemispherical depressions, hemispherical protrusions, and rectangular parallelepiped protrusions. Eight plates had 1.6-mm-radius hemispherical dimples machined in the surfaces, each plate having a different uniform

element spacing. When testing was completed on the dimpled plates, 3.2-mm-(0.125-in-) diameter aluminum balls were placed in the dimples, creating hemispherical protrusions. The hemispherical test plates were given a light coat of flat black spray paint, which served two purposes; it provided a surface with known emissivity (0.95) for infrared temperature measurements, and it also served to hold the spheres in place in the depressions well enough to withstand the maximum tunnel velocity of 40 m/s (132 ft/s).

Six plates were milled such that each had uniformly spaced rectangular parallelepiped elements, with each plate having a different element spacing. The rectangular element height was chosen to be the same as the hemispherical element height, 1.59-mm (0.0625-in), and the element cross sectional area, 2.5-mm x 2.5-mm (0.0984-in x 0.0984-in), was chosen to give equal projected areas (facing the flow) for both types of elements. The element spacings were chosen to achieve A_s/A_p values for the plates that bracket the peak in the Simpson equivalent sand-grain correlation curve, viz. $A_s/A_p = 4.68$ where A_s is the total plate area and A_p is the total projected area of all elements facing the flow (see the Appendix for more detail). Typical specification drawings for the hemispherical and rectangular rough surfaces are shown in Figures 4 and 5, respectively. Unfortunately, there was some plate-to-plate variation in the depth of the hemispherical depressions milled in the surfaces. This caused deviation of the actual measured A_s/A_p from the design values for several plates which resulted in three plates having A_s/A_p values between 3 and 3.5, and three plates having values between 5 and 5.5.

Table 1 gives values of hole spacing and depth and the correlation parameter values ($A_s/A_p * d/D$ as described in the next section) for the dimpled plates. Table 2 gives values of element spacing and height and design and actual values of A_s/A_p for the hemispherical roughness plates. Table 3 gives the same information for the rectangular roughness plates.

Velocity profile and turbulence intensity data were obtained using a three-axis traversing mechanism along with a Dantec model 55D01 anemometer, model 55P11 boundary layer probes, model 55P14 right angle probes (used to

make measurements between roughness elements), and a digital data acquisition system. The data acquisition system consisted of a Metrabyte DASH 16 A/D board installed in an IBM AT PC. A custom data acquisition program controlled the z-axis position of the hot wire probe, the sampling rate and sample size, and also performed data reduction to provide rms and mean velocity values, and turbulence intensity. The tunnel freestream velocity was measured using a pitot tube connected to a Datametrics model 590 pressure sensor, with the output from the pressure sensor read on a Datametrics model 1400 electronic manometer. This system was also used for calibration of the hot wire probes. The electronic pressure measuring system was itself calibrated periodically against an inclined manometer.

TABLE 1
Parameters For Dimpled Roughness Plates

Plate No.	Hole Spacing (mm)	Avg Hole Depth (mm)	$A_s/A_p * d/D$
D1	3.45	1.62	0.274
D2	3.71	1.44	0.351
D3	3.96	1.37	0.438
D4	4.22	1.73	0.706
D5	4.45	1.58	0.765
D6	4.88	1.41	0.915
D7	5.64	1.32	1.303
D8	6.88	1.44	2.329

TABLE 2
Parameters For Hemispherical Roughness Plates

Plate No.	Element Spacing mm	Avg Element Height mm	Design A_s/A_p	Actual A_s/A_p
H1	3.45	1.56	3	3.15
H2	3.71	1.74	3.5	3.17
H3	3.96	1.81	4	3.43
H4	4.22	1.44	4.5	5.19
H5	4.45	1.60	5	5.04
H6	4.88	1.76	6	5.37
H7	5.64	1.86	8	6.81
H8	6.88	1.74	12	10.97

TABLE 3
Parameters For Rectangular Roughness Plates

Plate No.	Element Spacing (mm)	Groove Width (mm)	A_s/A_p
R1	3.28	0.79	2.74
R2	3.68	1.19	3.45
R3	4.08	1.59	4.26
R4	4.47	1.98	5.05
R5	4.87	2.38	6.02
R6	5.66	3.18	8.07

(Height is 1.59-mm and base dimensions are 2.49-mm x 2.49-mm for all elements)

RESULTS AND DISCUSSION

Before performing measurements on the rough plates, qualification tests were run on a smooth surface. This provided both insight into the viability of the test equipment and reference values of skin friction and heat transfer, and reference velocity and turbulence profiles. Figure 6 shows mean velocity profiles at the front, middle, and back of the smooth plate, and Figure 7 shows turbulence profiles at the same locations. The profiles indicate that the flow is fully turbulent over the length of the smooth plate. In Figure 8, measured drag values are plotted along with predicted values obtained from the Taylor, Coleman and Hodge boundary layer code. The agreement is very good. Experimental heat transfer data for the smooth plate is shown in Figure 9.

Figures 10 and 11 show values of C_d and drag augmentation, respectively, for the dimpled roughness plates. As mentioned in the previous section, there was some plate-to-plate variation of the depth of the depressions milled into the plates, and the effects of this can be seen in the figures. The two points which plot very close together represent plates D4 and D5 (Table 1). These surfaces produced nearly identical drag and heat transfer measurements, with good repeatability for both, since they were tested several times each to verify the seemingly anomalous results.

Various dimensionless spacing parameters were tried in an attempt to correlate the data. Based partly on the experimental results of Wieghardt, as summarized by Schlichting (ref 27), and in an attempt to correlate depression roughness in a manner similar to the methods used for protrusions, the parameter $A_s/A_{fp} * d/D$ was devised, where A_s is the smooth plate area remaining between dimples, A_{fp} is the total footprint area of the dimples, ($A_s + A_{fp} = A_{plate}$) D is the hole diameter, and d is the depth. As seen in Figures 10 and 11, the points for plates D4 and D5 correlate well with this parameter. In Figures 12 and 13, which show Stanton number and heating augmentation data, respectively, the correlation parameter collapses the heat transfer results for the two plates in a similar fashion.

Plate D4 has a hole spacing of 4.22 mm and an average hole depth of 1.73 mm. Plate D5 has a hole spacing of 4.45 mm and an average hole depth of 1.58 mm. One might predict on first consideration that the closer spacing and deeper holes of plate D4 would produce a significantly higher skin friction than for plate D5, but this was not the case. A possible explanation lies in the results of Wieghardt as reproduced in reference 27 and shown here in Figure 14. Wieghardt investigated the skin friction effect of square bottom holes of diameter d and depth h and his data displayed a pronounced peak at $h/d = 0.5$. Plate D4 has an h/d value of 0.55 while plate D5 has a value of 0.5, precisely at the peak. The depth-to-diameter ratio of the plate D4 dimples has apparently given rise to a 10 percent decrease in drag effect per dimple that offsets the 10 percent greater number of dimples compared to plate D5. Hole depth is obviously an important parameter along with hole diameter and spacing for correlating both skin friction and heat transfer data for dimpled roughness.

It is evident from the results shown in Figures 10-13 that for dimpled roughness there is no peak in skin friction or heat transfer as element spacing decreases as occurs for protrusion roughness. Skin friction and heat transfer both increase monotonically with decreasing hole spacing since the depressions do not produce overlapping wake regions between elements.

Mean velocity profiles and turbulence intensity profiles are shown in Figures 15-30 for the dimpled roughness plates. All measurements were made at a freestream velocity of 27 m/s (88 ft/s). The velocity profiles all exhibit a similar loss in momentum at the rear of the plates when compared to the profiles at the front of the plates. Figure 31 compares mean velocity profiles at the rear of plates D4 and D5. The profiles are almost identical, in keeping with the nearly identical drag and heat transfer results for the plates. Figures 32 and 33 compare mean velocity and turbulence profiles, respectively, at the rear of six of the dimpled plates. In general, closer hole spacing leads to greater momentum loss and higher turbulence throughout the boundary layer.

Figures 34 and 35 show drag and heat transfer augmentation, respectively, for the hemispherical roughness test plates. The fact that variations in roughness height are present shows in the way that the data are scattered. For example, plate H4 was designed to have an A_s/A_p of 4.5, and should have plotted at or near the peaks of the two graphs. However, with the actual A_s/A_p for the plate being 5.19, the point plots in the vicinity of the other plates having similar A_s/A_p values. Though it is possible to discern a peak in drag and heat transfer near the theoretical peak of about 4.7, the scatter in the data makes the true location of the peak difficult to pinpoint.

Figures 36-51 show mean velocity and turbulence intensity profiles for the hemispherical surfaces. As a means of comparison, Figures 52 and 53 are plots of the same data at the back of five of the rough plates and the smooth plate. Note that plates H5 ($A_s/A_p=5.04$) and H6 ($A_s/A_p=5.37$) exhibit the greatest momentum loss and the highest peak values of turbulence intensity, in keeping with these plates having the highest drag values (Figure 34). Notice also that plate H1 ($A_s/A_p=3.15$), with the closest element spacing, exhibits the smallest momentum loss and the lowest turbulence intensity level. This is likely the consequence of what Morris (ref 28) calls the quasi-smooth or "skimming flow" regime, where stable vortices exist in the areas between the roughness elements, and the main flow only interacts with the crests of the elements after the first few rows of roughness.

The rectangular roughness plates were tested as both "k-type" (the base of the elements flush with the boundary layer plate) and "d-type" (the tops of the elements flush with the boundary layer plate) surfaces. The A_s/A_p values for the plates are given in Table 3.

Figure 54 shows drag augmentation data for the rectangular roughness plates in the two positions described above. Both curves exhibit a definite peak value, though the peaks do not coincide with the theoretical value of 4.68. As would be expected, the drag augmentation is greater overall when the elements protrude above the boundary layer plate. In Figure 55 heat transfer augmentation values are shown. Again, peak values are in evidence, with the

peaks in drag and heating augmentation occurring for the same surface when the roughness protrudes above the boundary layer plate. In the "d-type" position, the peak in heating augmentation is shifted to the left (towards higher density). Also of note is the fact that for the three most dense surfaces, the heat transfer is almost equal for both positions. It is believed that quasi-smooth flow exists at these densities, which causes the flow to only interact with the tops of the elements when the elements are above the boundary layer plate. This in turn creates a flow regime in the region of the elements which is similar to that which occurs when the element tops are flush with the boundary layer plate, and results in similar convective conditions for the two positions.

Figures 56-79 show mean velocity and turbulence intensity profiles for the rectangular roughness plates at the positions described previously. Figures 80 and 81 compare velocity profiles at the rear of the six rectangular roughness plates with the elements flush and protruding above the boundary layer plate respectively. Figures 82 and 83 compare the turbulence profiles at the rear of the plates for the flush and protruding positions respectively. As with the hemispherical surfaces, the plate which produces the highest drag measurement ($A_s/A_p = 6.02$) also has the highest turbulence intensity and largest downward shift of the velocity profile.

ROUGH SURFACE BOUNDARY LAYER CODE

One of the primary original objectives of this study was to improve the existing rough surface boundary layer code developed with support from the Air force Armament Laboratory by R. Taylor, H. Coleman and B. Hodge at Mississippi State University in 1984 and reported on in several references (e.g. refs 1,29,30). Henceforth, this code will be referred to as either the TCH Code or program ROUGH. ROUGH is a discrete element roughness code which attempts to model the details of the flow around individual roughness elements and thereby account for the influence of individual elements on the total skin friction and heat transfer. The discrete element method obviously incorporates more physics in the treatment of rough-surface boundary layer flow than does the equivalent sand-grain approach. And, in addition, the problem of ill-defined wall boundary conditions encountered with equivalent sand-grain models can be avoided in finite difference calculations using the discrete element approach.

While the discrete element method was alluded to by Schlichting in his early pioneering work on flows over uniform surface roughness, the first practical computer code to fully implement the method was the TCH Code. The TCH code calculates flat-plate, incompressible, zero-pressure gradient flow over three-dimensional surface roughness elements. The boundary layer momentum and energy equations are formulated for a control volume including blockage coefficients to account for the portion of the volume blocked to flow by the presence of the roughness elements.

The momentum equation contains a momentum sink term, F_D , accounting for the form drag due to individual roughness elements. The form drag is cast in terms of a drag coefficient, C_d , which is a function of the local Reynolds number based on the local diameter of the roughness element at distance y above the base surface. The drag force relation is given by:

$$F_D = \frac{1}{2} \rho C_d u^2 A_p$$

where A_p is the projected frontal area of a roughness element.

The energy equation contains a heat sink/source term to account for heat transfer to or from individual elements based on a local Nusselt number, Nu , correlation which is dependent upon local Reynolds number as well as Prandtl number. The heat transfer term takes the form:

$$Q = \frac{K}{d} Nu A_e (T_R - T_\infty)$$

where K is the thermal conductivity, A_e is the roughness element surface area, T_R is the element surface temperature and T_∞ is the free stream temperature.

ROUGH employs a variable grid, finite difference solution method to calculate surface drag and heat transfer values. A Prandtl mixing length turbulence model with VanDriest damping is employed for the Reynolds stress term and a constant turbulent Prandtl number of 0.9 for the eddy heat flux term. The Appendix provides a somewhat more detailed description of the discrete element model used in the code while Reference 1 provides complete mathematical details.

The C_d and Nu correlations employed in the original TCH code were developed for roughness elements of circular cross section through calibrations against several existing data sets including Schlichting's data for spheres and spherical segments, corrected by Taylor, Coleman and Hodge to rectify errors in Schlichting's original data reduction methods (ref. 31). The code appears to perform well when compared with experimental data for roughness elements of circular cross sections that are relatively widely spaced. When applied to cases with closely-spaced roughness elements, i.e., when wake regions behind individual elements begin to overlap and interact, the agreement is less satisfactory.

The C_d and Nu correlations originally adopted in the TCH code are as follows. For C_d :

$$\left. \begin{aligned} \log(C_d) &= -0.125 \log(Re_d) + 0.375 & Re_d < 60,000 \\ C_d &= 0.6 & Re_d > 60,000 \end{aligned} \right\} \quad (1)$$

For Nu:

$$\left. \begin{aligned} Nu_d &= 2.475 Re_d^{0.4} Pr^{0.36} & Re_d < 100 \\ Nu_d &= 1.043 Re_d^{0.5} Pr^{0.37} & 100 < Re_d < 1000 \\ Nu_d &= 0.963 Re_d^{0.6} Pr^{0.36} & 1000 < Re_d < 200,000 \\ Nu_d &= 0.060 Re_d^{0.84} Pr^{0.36} & Re_d > 200,000 \end{aligned} \right\} \quad (2)$$

Where Re_d is the local Reynolds number based on roughness element diameter which varies in the direction normal to the wall:

$$Re_d = \frac{U(y) d(y)}{\nu}$$

These correlations were arrived at through numerical experimentation but are based on correlations and data of Zukauskas for tubes in cross-flow (ref. 32). The rationale for this approach is that a thin slice of a roughness element, as modeled in the finite difference calculations, approximates a section of a circular cylinder in cross-flow. The C_d correlation was reportedly tested up to Reynolds numbers of 25,000 and the Nu_d correlation up to Re_d of 1000 (refs 1, 29). In later work, Hosni, Coleman and Taylor (ref. 16) modified the Nu_d correlation to the form:

$$Nu_d = 1.7 Re_d^{0.49} Pr^{0.4} \quad (3)$$

without specifying a Re_d range of applicability, but reportedly tested up to Re_d of 2,200.

Figures 84 and 85 show the results of predictions of drag and Stanton number using ROUGH with the C_d and Nu correlations as given in equations (1) and (3) compared with the measured values for six hemispherical roughness test plates. Re_d in these cases ranges from 0 to 2,300. The agreement between predicted and measured values is in general not good, particularly for heat transfer. The erratic fluctuations in predicted drag and heat transfer will be discussed further below.

The version of ROUGH received from its originators contained several bugs that prevented execution of the code. These bugs were located and fixed and the program was run for cases paralleling the experiments that were conducted for this study. These cases all involve flow over an initial section of smooth wall followed by a step change to a rough wall. The code was modified to treat the transition from a smooth to a rough wall by "turning off" the roughness for a specified entrance length by setting the roughness diameter to zero for all streamwise computational stations over the smooth portion.

Difficulty was encountered with convergence in some cases. In particular, convergence problems were aggravated by conditions of close roughness element spacing, high freestream velocity and small initial y-direction (normal to the plate) grid spacing. Several changes were made to the code in an attempt to remedy this problem as follows: All data types were changed from single to double precision, the maximum number of allowed iterations was increased and the relaxation constant was adjusted downward. These changes helped but did not cure the problem.

The program employs a variable grid spacing in the y-direction to increase the number of grid points in the steep gradient region close to the surface. The initial step size is given the variable name SQUIG. Step size increases geometrically after the first step, and the value of SQUIG determines the number of grid points between the surface and the tops of the roughness elements. It was found that the code would run for all experimental cases if the initial step size was increased as the element spacing decreased.

The recommended value of SQUIG from reference (1) is 0.005. This value results in 57 grid points below the element crests for hemispherical roughness with $k = 1.6$ mm. The code would run without problem with this SQUIG value only for wide element spacings and low velocity. For the closest spacing and highest velocity a SQUIG value of 0.36 was required for successful execution. This large initial grid space reduced the number of grid points below the element crests to only eight.

Use of a variable SQUIG value and a C_d correlation modified to incorporate roughness element spacing by introducing an As/Ap function into the correlation resulted in calculated drag values that closely agree with the experimental values as illustrated in Figure 86. The C_d correlation used to obtain these results was arrived at through numerical experimentation and is given by:

$$C_d = \left\{ 4.36 \left[1 - \frac{Ap}{As} \right] \left[\frac{Ap}{As} \right]^{0.1} - 2.32 \right\} \left\{ 10^{-0.25 \log(Re_d) + 0.82} \right\} \quad (4)$$

Likewise, heat transfer results were obtained that agreed well with experimental values by letting SQUIG vary and developing, through numerical experimentation, a Nu correlation that contained an As/Ap dependency given by:

$$Nu_d = \left\{ 2.8691 \left[1 - \frac{Ap}{As} \right] \left[\frac{As}{Ap} \right]^{0.13} - 1.2 \right\} Re_d^{0.7} Pr^{0.4} \quad (5)$$

Figure 87 shows the comparison of predicted and experimental Stanton numbers resulting from the above expression.

While this approach succeeded in producing results in good agreement with the experiments, it has no usefulness for design purposes. One would have no way of knowing, a priori, an appropriate value of SQUIG for a given roughness geometry.

Discussions with R. P. Taylor, one of the original authors of the code, resulted in implementing the following scheme to lessen the

computational "shock" introduced by a step change from a smooth to a rough surface. Eight additional rows of roughness elements with gradually increasing height and base diameter are introduced immediately upstream of the leading edge of the test plate (rough plate). Let us refer to these added rows as the "roughness ramp". The first row of roughness elements in the ramp has a height of 10 percent of the actual roughness height. The second row has a height of 20 percent of the actual, and so on. Thus the velocity profile undergoes a more gradual transition from smooth to rough over a short distance. This scheme greatly improved the convergence problem and the code will now run for all of the experimental cases with a SQUIG value of 0.005.

Another problem exists with the code, however, that has not been solved and has precluded obtaining satisfactory results while maintaining a single value of SQUIG for all cases. Drag and heat transfer values predicted with a constant SQUIG fluctuate erratically in a manner illustrated by Figure 84. Efforts to determine the cause of this have not been successful. In attempting to arrive at a C_d correlation that would produce better agreement, many runs were made with constant values of C_d instead of an Re_d dependent relation. It was noted that slight variations in C_d , e.g., on the order of one percent, can produce large variations in predicted drag, e.g., on the order of fifty percent. This is illustrated in Figure 88 which shows predicted values of drag calculated with ROUGH for various values of constant C_d for two different test cases and a freestream velocity of 40 m/s. The fluctuations of drag with C_d grow worse with closer roughness spacing.

The drag variations result from significant differences in calculated velocity profiles for small differences in the C_d value as shown in Figure 89 which presents two velocity profiles for a location just behind the leading edge of the smooth to rough transition. In this case, an increase in C_d from 0.88 to 0.89 resulted in a predicted drag increase from 1.5 N to 1.8 N. Clearly, neither velocity profile is physically correct since they both display an inflection near the top of the roughness elements. The reason for the problem with velocity profile calculations has not been determined.

The version of ROUGH submitted as part of this effort has been made interactive and adapted for either hemispherical, conical or rectangular parallelepiped uniform roughness. For roughness elements of circular cross section, e.g., cones, spheres, and spherical segments, it is shown in reference 1 that the blockage coefficients in the x (streamwise) and y (normal) directions, α_x and α_y , are equal and are given by:

$$\alpha_x = \alpha_y = \frac{\pi d(y)^2}{L l} \quad (6)$$

where L is the x direction element spacing and l is the z direction (transverse) element spacing. The local element diameter, d(y), for cones, spheres and spherical segments are given by:

$$\text{Cones:} \quad d(y) = d_o \frac{k - y}{k} \quad (7)$$

$$\text{Spheres:} \quad d(y) = 2 \sqrt{(d_o/2)^2 - (y - d_o/2)^2} \quad (8)$$

$$\text{Spherical Segments:} \quad d(y) = 2 \sqrt{R^2 - (R - k + y)^2} \quad (9)$$

$$\text{where:} \quad R = [(d_o/2)^2 + k^2]/2k$$

d_o is the base diameter and k is the element height.

For a uniform array of square parallelepipeds with base dimensions a x a and height k, as illustrated in Figure 90, it is readily apparent that:

$$\alpha_y = a^2/Ll.$$

The blockage coefficient in the x direction is found by calculating the average of α_x over the length L and noting that $\alpha_x = 0$ for all x not encountering an element and $\alpha_x = a/l$ for all x encountering an element.

$$\alpha_x = \frac{1}{L} \int_0^L \alpha_x dx = \frac{1}{L} \int_0^a \frac{a}{l} dx = \frac{a^2}{Ll} \quad (10)$$

Thus $\alpha_x = \alpha_y$ for square parallelepipeds also.

When the program is run, it prompts the user for values of the following input variables:

- STRCH2 - Number of element rows encompassed in each x grid step over the rough surface (usually 1)
- CD - Element drag coefficient. Setting equal to 0 invokes the default Cd correlation. Setting not equal to 0 results in a constant Cd equal to the value set
- SHAPE - Element type; 1 = cones, 2 = hemispheres, 3 = square
- DO or A - Base diameter of cone or hemispherical element or width of square element (ft)
- ASAP - A_s/A_p value for surface
- UINF - Freestream velocity (ft/s)
- NPTS - Number of points in computational grid normal to the surface (120 recommended)
- NSTN - Number of streamwise computational stations
- RK - Roughness element height (ft)
- CL - Roughness element spacing (ft)
(length of surface = STRETCH2*NSTN*CL)
- SQUIG - Initial y-direction (normal) grid space (0.005 recommended)
- WIDTH - Width of rough surface (ft)
- TWALL - Wall surface temperature (°R)
- TINF - Freestream temperature (°R)

The code returns drag force (lbf), heat flux (Btu/hr) and Stanton number values for the test surface.

SUMMARY

Results have been presented for skin friction, heat transfer and velocity profile tests performed in a low speed wind tunnel on three classes of uniform roughness including hemispherical dimples, hemispherical protrusions and rectangular parallelepiped protrusions. Eight test plates were fabricated from aluminum with various spacings of 1.6-mm-radius hemispherical dimples. After testing the dimpled surfaces, 3.2-mm-diameter aluminum balls were inserted in the dimples to create hemispherical protrusion roughness patterns. Six aluminum plates with various spacings of 2.5-mm- x 2.5-mm- x 1.6-mm-high rectangular parallelepipeds were fabricated and tested. The spacings were chosen to produce A_s/A_p values for the protrusion roughness that would bracket the peak in the Simpson equivalent sand-grain roughness correlation.

The dimpled roughness patterns did not exhibit a peak in either skin friction or Stanton number (St). Both drag and heat transfer rate increased monotonically with decreasing hole spacing. The downward shift in the velocity profile and the turbulence level in the boundary layer also increased steadily with closer hole spacing. Plate-to-plate variations in hole depth gave rise to seemingly anomalous drag and St results that were successfully correlated with the inclusion of depth in the shape/spacing correlation parameter.

Both the hemispherical and the rectangular protrusion roughness patterns exhibited a peak in skin friction and St at element spacings in the range expected from the equivalent sand-grain correlations. The spacing that produced the highest drag also exhibits the largest downward shift of the velocity profile and highest turbulence level in the boundary layer. Element height variation caused by the hole depth variation resulted in several surfaces that had very similar A_s/A_p values and, consequently, similar skin friction and heat transfer results.

The drag and heat transfer data were used for comparison with the Taylor, Coleman and Hodge (TCH) discrete element roughness code to try and improve the accuracy for cases of closely spaced roughness elements when wakes from individual elements overlap and interact. Satisfactory results could be obtained only by increasing the y-direction (normal to the plate) initial step size as the element spacing decreased. When using a reasonable constant value of the initial y-step size, wide variations in predicted drag occur which were determined to result from the effect of the individual element drag coefficient, C_d , on the velocity calculation in the region near the element crests. The problem is exhibited by changes in the predicted drag of up to fifty percent resulting from changes in C_d on the order of one percent. Neither the specific cause of this problem nor a remedy for it has as yet been found, and therefore the code in its present form is unsuitable for design purposes.

REFERENCES

1. Taylor, R. P., Coleman, H. W., and Hodge, B. K., "A Discrete Element Prediction Approach for Turbulent Flow over Rough Surfaces," Mech. and Nuc. Eng. Dept., Mississippi State Univ., Report TFD-84-1, 1984.
2. Nikuradse, J., "Laws for Flows in Rough Pipes," VDI-Forschungsheft, Vol. 4, 1933; NACA TM 1292, 1950.
3. Schlichting, H., "Experimental Investigation of the Problem of Surface Roughness," NACA Translation, TM 823, 1937.
4. Dvorak, F. A., "Calculation of Turbulent Boundary Layers on Rough Surfaces with Pressure Gradient," *AIAA Journal*, Vol. 7, pp. 1752-1759, 1969.
5. Dirling, R. B., Jr., "A Method for Computing Rough Wall Heat Transfer Rates on Reentry Nosetips," AIAA Paper 73-763, 1973.
6. Simpson, R. L., "A Generalized Correlation of Roughness Density Effects on the Turbulent Boundary Layer," *AIAA Journal*, Vol. 11, pp. 242-244, 1973.
7. Cope, W. F., "The Friction and Heat Transmission Coefficients of Rough Pipes," *Proceedings of the Institute of Mechanical Engineers*, Vol. 45, p. 99, 1941.
8. Nunner, W., "Heat Transfer and Pressure Drop in Rough Tubes," VDI-Forschungsheft, No. 455, pp. 5-39, 1956.
9. Owen, P. R. and Thomson, W. R., "Heat Transfer Across Rough Surfaces," *Journal of Fluid Mechanics*, Vol. 15, pp. 321-334, 1963.
10. Dipprey, D. F. and Sabersky, R. H., "Heat and Momentum Transfer in Smooth and Rough Tubes at Various Prandtl Numbers," *International Journal of Heat and Mass Transfer*, Vol. 6, pp. 329-353, 1963.
11. Betterman, D., "Contribution a l'Etude de la Couche Limite Turbulente le long de Plaques Rugueuses," *International Journal of Heat and Mass Transfer*, Vol. 9, pp. 153-164, 1966.
12. Coleman, H. W., "Momentum and Energy Transport in the Accelerated Fully Rough Turbulent Boundary Layer," Ph.D Dissertation, Mech. Eng. Dept., Stanford University, 1976.

13. Pimenta, M. M., "The Turbulent Boundary Layer: An Experimental Study of The Transport of Momentum and Heat with the Effect of Roughness," Ph.D Dissertation, Mech. Eng. Dept., Stanford University, 1975.
14. Healzer, J. M., "The Turbulent Boundary Layer on a Rough, Porous Plate: Experimental Heat Transfer with Uniform Blowing," Ph.D Dissertation, Mech. Eng. Dept., Stanford University, 1974.
15. Ligrani, P. M., "The Thermal and Hydrodynamic Behavior of Thick, Rough-Wall, Turbulent Boundary Layers," Ph.D Dissertation, Mech. Eng. Dept., Stanford University, 1979.
16. Hosni, M. H., Coleman, H. W., and Taylor, R. P, "Measurements and Calculations of Rough Wall Heat Transfer in the Turbulent Boundary Layer," *International Journal of Heat and Mass Transfer*, Vol. 34, pp. 1067-1082, 1991.
17. Clauser, F., "The Turbulent Boundary Layer," *Advances in Applied Mechanics*, Vol. 4, 1956.
18. Cebeci, T. and Chang, K. C., "Calculation of Incompressible Rough-Wall Boundary-Layer Flows," *AIAA Journal*, Vol. 16, pp. 730-735, 1978.
19. Wilcox, D. C., "A Complete Model Of Turbulence Revisited," AIAA Paper 84-0176, 1984.
20. Finson, M. L., "A Reynold's Stress Model for Boundary Layer Transition with Application to Rough Surfaces," AFOSR-TR-0322, 1975.
21. Christoph, G. A., "Law of the Wall Analysis for Turbulent Heating on Rough Surfaces," AIAA Paper 82-0199, 1982.
22. Hodge, B. K. and Adams, J. C., "The Calculation of Compressible Transitional Turbulent and Relaminarizational Boundary Layers over Smooth and Rough Surfaces Using an Extended Mixing-Length Hypothesis," AIAA Paper 77-682, 1977.
23. Finson, M. L. and Clark, A. S., "The Effect of Surface Roughness Character on Turbulent Reentry Heating," AIAA Paper 80-1459, 1980.
24. Christoph, G. H. and Pletcher, R. H., "Prediction of Rough-Wall Skin Friction and Heat Transfer," *AIAA Journal*, Vol. 21, pp. 509-515, 1983.

25. Tarada, F., "Prediction of Rough-Wall Boundary Layers Using a Low Reynold's Number k - ϵ Model," *International Journal of Heat and Fluid Flow*, Vol. 11, pp. 331-345, 1990.
26. Bandyopadhyay, P. R., "Rough-Wall Turbulent Boundary Layers in the Transitional Regime," *Journal of Fluid Mechanics*, Vol. 180, pp. 231-266, 1987.
27. Schlichting, H., *Boundary-Layer Theory*, 7th Edition, McGraw-Hill Inc., New York, 1979.
28. Morris, H. M., *Applied Hydraulics in Engineering*, Ronald Press Co., New York, 1963.
29. Taylor, R. P., Coleman, H. W., and Hodge, B. K., "Prediction of Turbulent Rough-Wall Skin Friction And Heat Transfer Using a Discrete Element Approach," *Journal of Fluids Engineering*, Vol. 107, pp. 251-257, 1985.
30. Taylor, R. P., Coleman, H. W., and Hodge, B. K., "Prediction of Heat Transfer in Turbulent Flow over Rough Surfaces," *ASME Journal of Heat Transfer*, Vol. 111, pp. 568-572, 1989.
31. Coleman, H. W., Hodge, B. K., and Taylor, R. P., "A Reevaluation of Schlichting's Surface Roughness Experiment," *J. of Fluids Engineering*, Vol. 106, pp. 60-65, March, 1984.
32. Zukauskas, A., "Heat Transfer from Tubes in Crossflow," *Advances in Heat Transfer*, Academic Press, New York, 1972.
33. Seidman, M. H., "Rough Wall Heat Transfer In a Compressible Turbulent Boundary Layer," AIAA Paper 78-163 presented at the AIAA 16th Aerospace Sciences Meeting, Huntsville, Ala., Jan. 16-18, 1978.
34. Keel, A. G., "Influence of Surface Roughness on Skin Friction and Heat Transfer for Compressible Turbulent Boundary Layers," AIAA Paper 77-178, 1977.
35. Young, F. L., "Experimental Investigation of The Effects of Surface Roughness on Compressible Turbulent Boundary Layer Skin Friction and Heat Transfer," Univ. of Texas, Defense Laboratory Report DRL-532, 1965.
36. Chen, C. K., "Characteristics of Turbulent Flow Resistance in Pipes Roughened with Hemispheres," Ph.D Dissertation, Washington State Univ., 1971.

APPENDIX

LITERATURE REVIEW

Nikuradse (ref 2) conducted experiments in order to study the effects of surface roughness on turbulent boundary layer flow through pipes. Test sections were fabricated by gluing sand grains to the walls of pipes in the most dense arrangement possible. Six different sand grain sizes were tested, at Reynold's numbers (based on pipe diameter) from 500 to 1,000,000, and the results were plotted in terms of friction factor versus Reynold's number.

Nikuradse characterized rough-wall turbulent boundary layer flow based on the roughness Reynold's number, defined as:

$$Re_k = \frac{ku_*}{\nu}$$

where $u_* = \sqrt{\tau_w} / \rho$ is the friction velocity, k is the sand grain size, and ν is the fluid kinematic viscosity. For values of $Re_k < 5$, the flow is said to be hydraulically smooth. In other words, the size of the roughness is such that the elements do not extend above the viscous sublayer, and therefore the boundary layer is not affected by the presence of the rough surface. Transitionally rough flow exists when $5 < Re_k < 55-70$. Here, the roughness is just beginning to protrude through the viscous sublayer, and modification of the overall boundary layer flow parameters starts to take place. At $Re_k > 70$, the sublayer is thought to be destroyed by the roughness, consequently the rough wall has a major influence on flow parameters such as friction and heat transfer. The flow is defined as fully rough at this point.

In analyzing the effects of rough walls on boundary layer flow (especially shear stress and velocity profiles), Nikuradse began with the assumption that roughness effects were confined to the near-wall region of the boundary layer. He then elected to use the well known "law of the wall" equation as the basis for his analysis:

$$\frac{u}{u_*} = 5.75 \log \frac{yu_*}{\nu} + 5.5$$

Nikuradse assumed a modified version of this equation which took the

form:

$$\frac{u}{u_*} = 5.75 \log \frac{y}{k} + B$$

where k represents the roughness height, and B is a constant which is dependent upon the size of the roughness and the fluid flow regime (as an example, for fully rough flow, B has a value of 8.48). It was Nikuradse's belief that the logarithmic velocity profile obtained from flow over a rough surface should have the same slope as a profile one would see for a smooth wall (hence the same value of 5.75 for both equations), but that the y intercept should vary based on the nature of the roughness (the value of B then changes).

Schlichting (ref 3) studied fully-developed channel flow over uniform, three-dimensional roughness elements. Three sides of the rectangular test section were smooth, with the upper wall roughened. Test plates were roughened with spheres, spherical segments, cones, and long and short angles, with various relative spacings and roughness sizes. It was Schlichting's hope to be able to use Nikuradse's data base, along with the results from his own experiments, to relate non-sand grain roughness to an equivalent sand grain value which could then be used as a means of making Nikuradse's data more widely applicable. To that end, Schlichting devised the equivalent sand grain roughness parameter, k_s , by equating Nikuradse's logarithmic profile relation for fully-rough flow:

$$\frac{u}{u_*} = 5.75 \log \frac{y}{k_s} + 8.48$$

to a general equation:

$$\frac{u}{u_*} = 5.75 \log \frac{y}{k} + A$$

where u_* and the constant A were determined from experiment. Schlichting thus obtained:

$$\frac{k_s}{k} = 10^{(8.48 - A)/5.75}$$

Schlichting's method consisted of curve fitting velocity profiles from

non-sand grain surfaces to the logarithmic profile to obtain the value of A, and measuring the pressure drop in order to calculate the friction velocity. From these values, k_s/k could be found and, using the assumption of Prandtl that the logarithmic region of boundary layers is identical for both flat plates and circular pipes, Schlichting could then apply the pipe flow results of Nikuradse to flat plates. This procedure was necessary for determining k_s/k in the transitional flow regime where skin friction is a function of both Re and roughness size. For fully-rough flow, with skin friction independent of Re, Schlichting was able to provide the following correlations when k_s is known:

$$C_f = \left[2.87 + 1.56 \log \left(\frac{x}{k_s} \right) \right]^{-2.5}$$

and:

$$\bar{C}_f = \left[1.89 + 1.62 \log \left(\frac{1}{k_s} \right) \right]^{-2.5}$$

where C_f is a local friction coefficient based on the distance x from the leading edge of a rough surface, and \bar{C}_f is the friction coefficient for a rough surface of length 1. Both equations are valid over the range $200 < 1/k_s < 1,000,000$.

One shortcoming common to the analytical methods of both Nikuradse and Schlichting is the assumption that the logarithmic law of the wall velocity profile for rough surfaces would have the same slope as would the profile for a smooth wall. For a rough wall logarithmic profile to have the same slope as a smooth wall profile, the "y" term in the logarithmic equation must be incremented by some finite amount, which Nikuradse called " Δz ", and Schlichting called " Δy ". Schlichting calculated the virtual wall location from:

$$\Delta y = V/LW$$

where V is the volume occupied by roughness elements on a surface of dimension $L \times W$. This is the so-called "melt down" location and is the distance that the flow is displaced from the wall ($y=0$) due to the presence of roughness. Although this concept is helpful as applied to the equivalent sand grain

roughness method, it has no real physical basis, and is not useful when attempting to model rough-wall flow dynamics. Another shortcoming is the fact that there is no provision for including roughness geometry and spacing in the equivalent sand-grain method, even though Schlichting designed his experiment with these parameters in mind, and the resulting data showed that geometry and spacing were important influences on rough-wall flow behavior. In an attempt to extend the equivalent sand-grain roughness method to more contemporary experimental data sets, Dvorak, Simpson and Dirling presented correlations which were designed for use with rough surface boundary layer computer codes.

Dvorak's correlation (ref 4) was based upon the rough-wall skin friction equation developed by Clauser (ref 17):

$$\sqrt{\frac{2}{C_f}} = A \log \frac{u \delta^*}{\nu} + B - \frac{\Delta u}{u_*}$$

where $\Delta u/u_*$ represents the downward shift of a rough wall boundary layer profile in the logarithmic region, and is given by:

$$\frac{\Delta u}{u_*} = A \log k \frac{u_*}{\nu} + C$$

where k is the roughness height, and C represents some function $f(\lambda)$, which is dependent upon the roughness geometry and spacing, as specified by the roughness correlation parameter, λ , which represents the ratio of total surface area to roughness area. A graph of $\Delta u/u_*$ versus λ is shown in Figure A-1, plotted along with the data of Nikuradse, Schlichting, Betterman, and others. The vertex of the correlation, at a value of $\lambda = 4.03$, represents the point at which the maximum skin friction would occur for a given roughness type. Decreasing values of λ represent decreasing roughness spacing. Figure A-1 thus indicates a reduction in skin friction (relative to the maximum value) with decreasing spacing, a phenomenon first observed and reported by Schlichting (ref 3).

Simpson (ref 6) modified Dvorak's correlation to make it more applicable to three-dimensional roughness. This was accomplished by devising

a new roughness shape and spacing parameter, λ_k , which is defined as the ratio of the total surface area to the total roughness projected frontal area normal to the flow, A_s/A_p . This parameter was substituted into Dvorak's equations from Figure A-1, and the results were plotted as shown in Figure A-2. From this graph, Simpson was also able to derive an equation relating λ_k to the equivalent sand-grain roughness parameter k_s :

$$f(\lambda_k) = -3 - \left[\frac{1}{K} \right] \ln \left| \frac{k}{k_s} \right|$$

where K is the Karman boundary layer constant equal to 0.40, and k is the actual roughness height.

Dirling (ref 5) developed a correlation to calculate roughness augmented skin friction and heat transfer on reentry vehicle nose tips, using a compressible flow, momentum integral code. By plotting the equivalent sand-grain roughness data of Schlichting, Betterman, and Liu, et al. versus the roughness geometry/spacing parameter:

$$\lambda = \frac{d}{k} \left[\frac{A_{ws}}{A_p} \right]^{4/3}$$

where d is the spacing between elements, k is the roughness height, A_{ws} is the total windward surface area of the elements, and A_p is the projected windward surface area of the elements, Dirling derived the correlation:

$$\frac{k_s}{k} = \begin{cases} 0.0164 \lambda^{3.78}, & \lambda < 4.93 \\ 139 \lambda^{-1.9}, & \lambda > 4.93 \end{cases}$$

which is shown in Figure A-3.

It must be mentioned that although there is much similarity among the three roughness correlations discussed above, when put to actual use, significant differences become apparent. Taylor, Coleman, and Hodge (ref 1) have outlined the disadvantages of the sand-grain correlations, pointing out that the accuracy of the Dirling correlation, which is demonstrably the better of the three, is approximately $\pm 100\%$ compared to the data used in its

development. Also the sand-grain correlations do not differentiate between two-dimensional and three-dimensional roughness types which display quite different flow patterns in the region below the roughness crests. And, finally, the correlations rely heavily on Schlichting's data which have been shown by Taylor, Coleman, and Hodge to be flawed due to the fact that Schlichting neglected the contribution of the side walls of his channel to the measured shear stress, and his assumption of the existence of a "melt-down" location for computing C_f values.

In regards to the present experiments, the rough surfaces were designed to bracket the peak roughness based on Simpson's sand-grain correlation parameter, i.e., $A_s/A_p = 4.68$. The resulting surfaces all have Dirling parameters, $d/k(A_{ws}/A_p)^{4/3}$, greater than the correlation peak value of 4.93. The experimental results exhibit a peak in skin friction occurring for the surfaces tested at an A_s/A_p value between 4 and 6.

Dipprey and Sabersky (ref 10) studied the relationship between skin friction and heat transfer in tubes. Their stated goal was to extend Nikuradse's rough-wall skin friction analysis to heat transfer. To this end, the well known Reynold's analogy $St = C_f/2$ which relates smooth-wall skin friction to the heat transfer was used as the basis for their analysis. Tubes were plated with nickel in a manner which resulted in a surface that resembled closely packed sand grains, and water was used as the fluid. In extending the Reynold's analogy to rough surfaces, they correlated their data with the equation:

$$\frac{C_f}{2 St} = 1 + \left[\frac{C_f}{2} \right]^{1/2} [g(\epsilon^*) - 8.5]$$

where

$$\epsilon^* = \frac{u_* k_s}{\nu}$$

and for fully rough flow:

$$g = 5.19 (\epsilon^*)^{0.2} Pr^{0.44}$$

Building on the work of Owen and Thomson (ref 9), Seidman (ref 33)

derived the following correlation for rough wall, turbulent boundary layer heat transfer:

$$St = \frac{C_f}{2} \left[1 + 0.52 \left(\frac{C_f}{2} \right)^{0.725} (Re_k)^{0.45} (Pr)^{0.8} \right]^{-1}$$

This equation was in good agreement with the subsonic data of Pimenta (ref 13), as well as the supersonic data of Keel (ref 34) and Young (ref 35).

In studying the usefulness of the heat transfer correlations presented above, two disadvantages become apparent. One, without prior knowledge of the value of C_f the equations are not applicable; and two, since there is no evidence that the mechanisms of wall shear and heat transfer are in any way similar, there is reason to doubt the accuracy of any correlation which relies on a skin friction value, since this cannot fully account for the effects of roughness geometry and spacing, and their subsequent influence on flow dynamics in the vicinity of the roughness elements.

In light of the deficiencies found in the correlations for rough-wall skin friction and heat transfer, Taylor, Coleman, and Hodge sought to derive a prediction model based on the discrete element method. A few important aspects of their derivation will be highlighted below. For a complete description, the reader should consult Reference 1. For convenience, Taylor, Coleman and Hodge will hereafter be referred to using the abbreviation TCH.

In attempting to model the effects of roughness on boundary layer flow, TCH began with the concept of flow blockage. Due to their physical presence, roughness elements reduce the available area near the wall for fluid flow. For uniform arrays of elements of circular cross section, averaged over an area containing several elements, the blockage coefficient α in the x (streamwise), and y (normal) directions, are given by:

$$\alpha_x = \alpha_y = \frac{\pi d(y)^2}{4Ll}$$

where $d(y)$ represents the element diameter as a function of height above the base surface, L is the spacing between elements in the streamwise direction,

and l is the spacing in the transverse direction. These blockage coefficient values are then included in the boundary layer equations in the form $(1 - \alpha)$, so that when roughness elements are not present (either a smooth area between elements, or above the crests of the elements) the equations are unchanged. To represent the contribution of roughness elements to skin friction TCH included in the momentum balance the term:

$$F_d = \frac{1}{2} \rho C_d U^2 (\delta A_p)$$

where δA_p is the projected area of the roughness elements in the control volume which is a function of $d(y)$, the element diameter at height y above the base surface, and C_d is a drag coefficient for an individual roughness element. To represent the heat transfer contribution of the roughness, TCH include in the energy equation the term:

$$Q = \frac{K}{d} Nu_d A_e (T_R - T)$$

where d is the roughness element diameter, K is the fluid thermal conductivity, Nu_d is a local roughness element Nusselt number, A_e is the heat transfer area of the roughness elements in a control volume, and T_R is the element temperature.

Correlations for C_d and Nu_d were developed by using the data of Zukauskas (ref 32) for banks of cylinders in crossflow as a starting point. It was postulated by TCH that a differential "slice" through an array of elements of circular cross section would resemble the same from a bank of circular cylinders at a given height above the base of the elements. The correlations were then fine-tuned by calibration against existing rough wall skin friction and heat transfer data, in particular the data sets of Schlichting (ref 3), Chen (ref 36), and Coleman (ref 12), and more recently the heat transfer data of Hosni, et al. (ref 16). The correlations thus obtained are, for the drag coefficient:

$$\log C_d = -0.125 \log(Re_d) + 0.375, \quad Re_d < 60,000$$

$$\log C_d = 0.6, \quad Re_d > 60,000$$

And, for the element Nusselt number:

$$Nu_d = 1.7 Re_d^{0.49} Pr^{0.4}$$

where Re_d is the local Reynold's number based on the roughness diameter which varies with the distance y above the base surface:

$$Re_d = \frac{U d(y)}{\nu}$$

The TCH discrete element computer code implements the above concepts in a finite difference formulation using a variable grid spacing in the y direction. A Prandtl mixing length turbulence model with Van Driest damping is employed for the Reynolds stress term and a constant turbulent Prandtl number of 0.9 is assumed to model the eddy heat flux term.

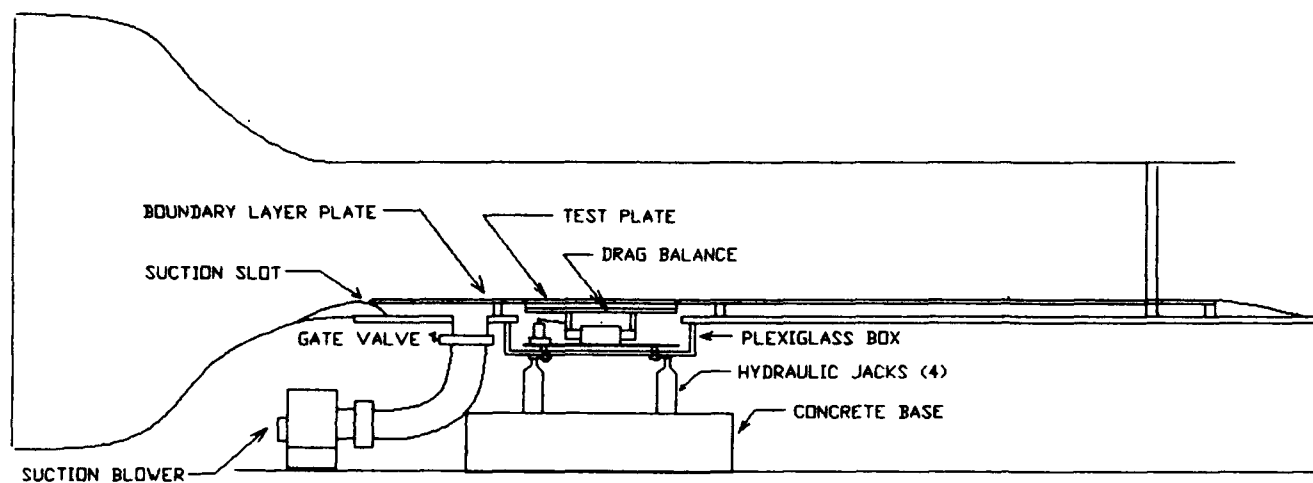


Figure 1 - Schematic of Wind Tunnel and Drag Balance

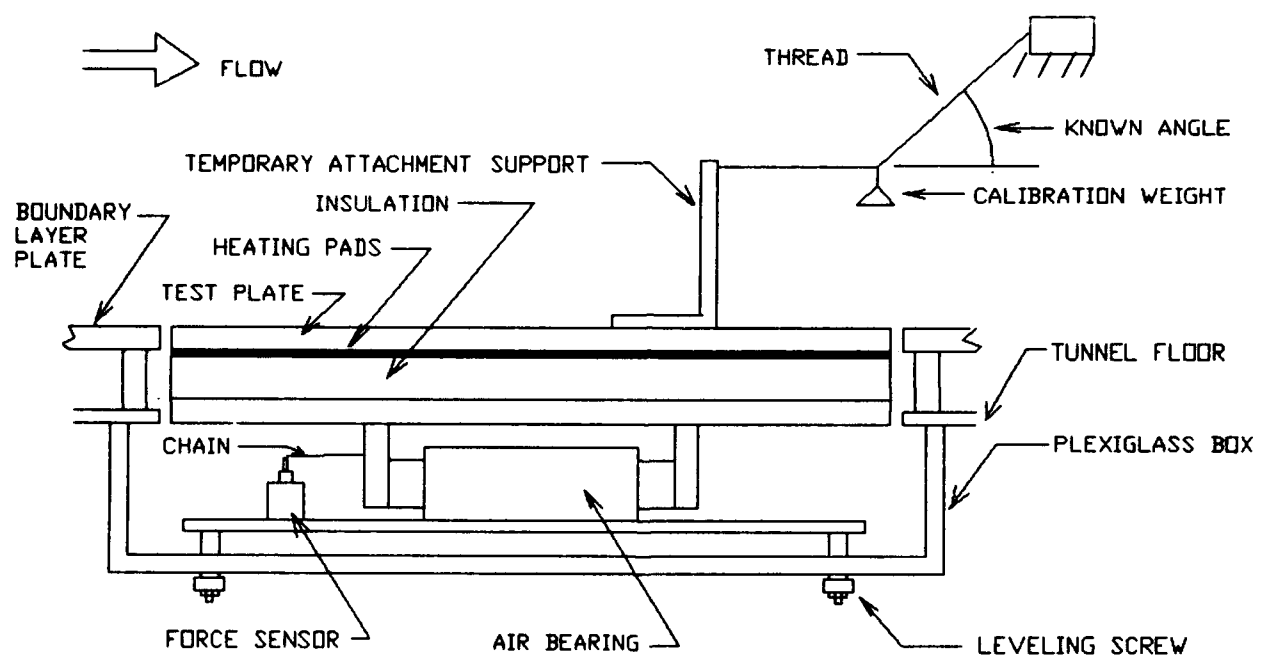
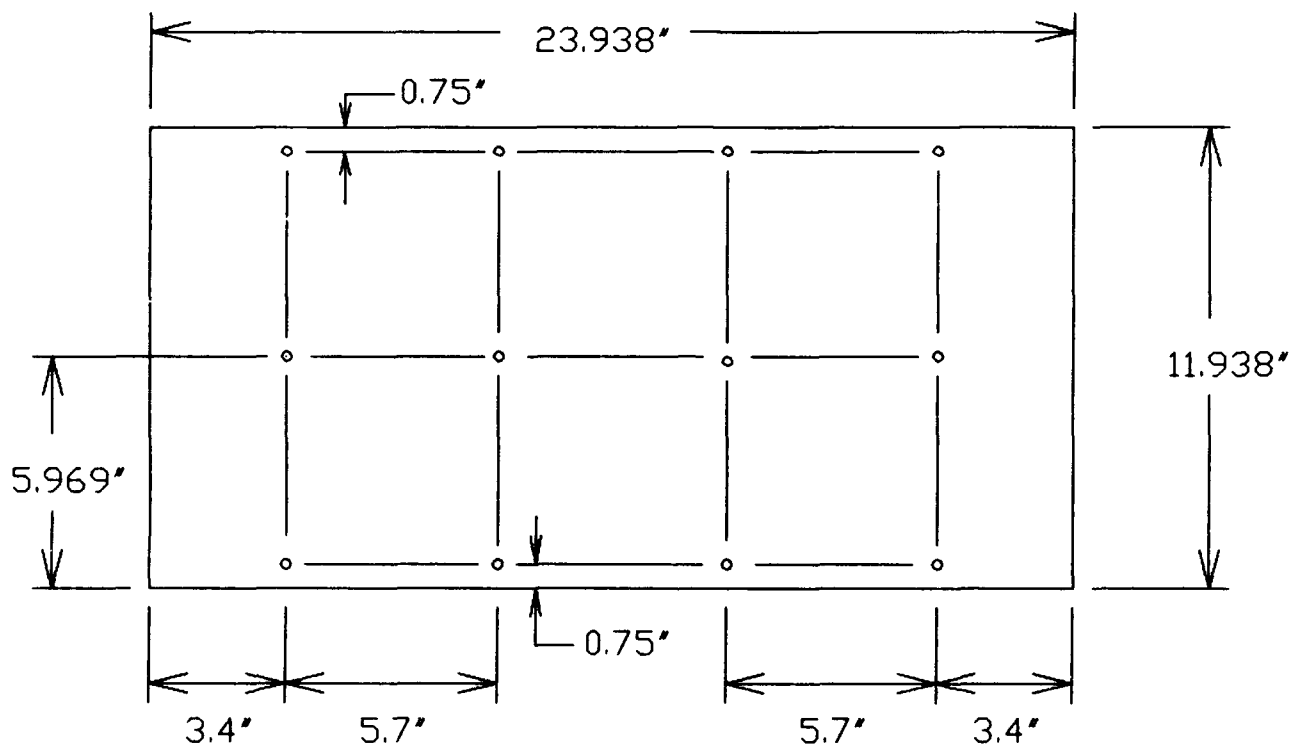
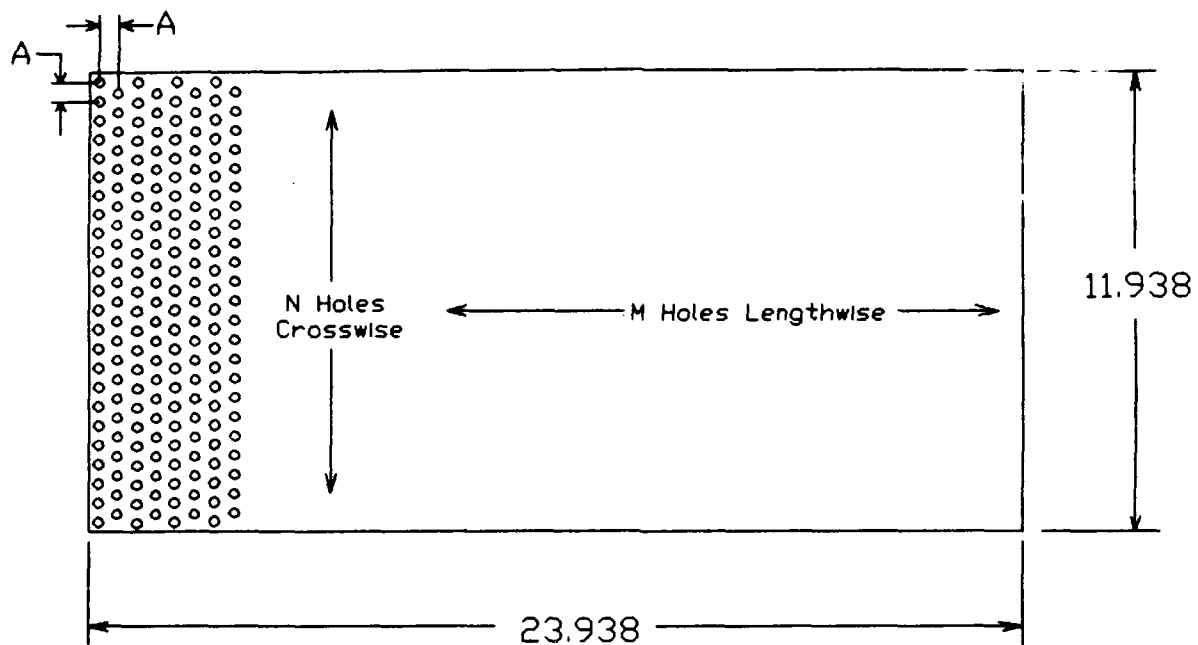


Figure 2 - Calibration Method For Drag Balance



Not to Scale

Figure 3 - Location of Thermocouples in Test Plate

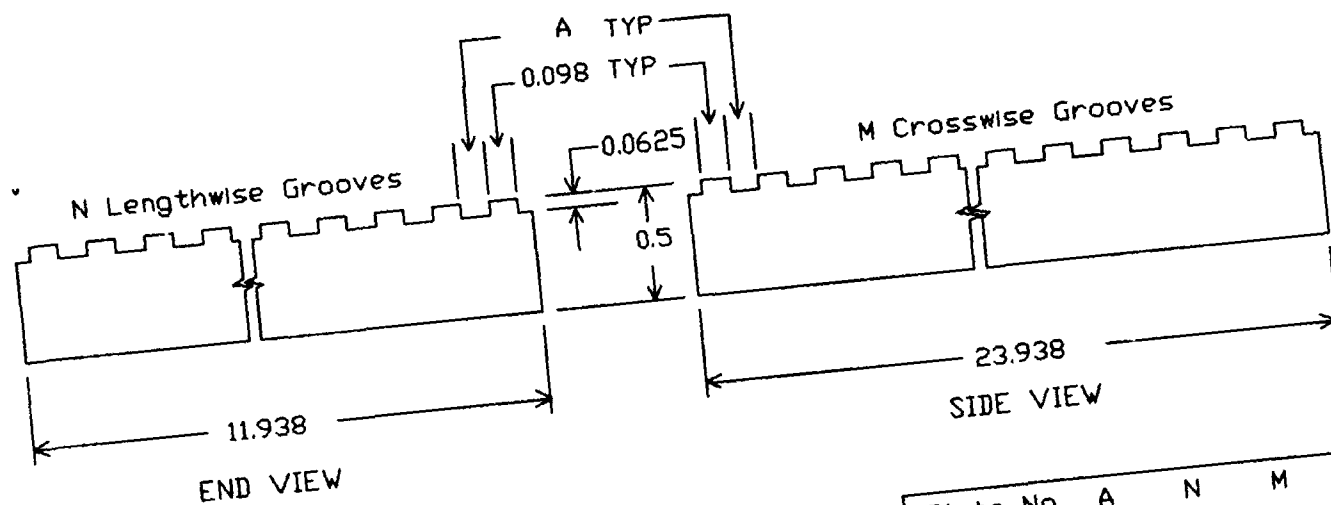


NOTES:

Not to scale
 Dimensions in inches
 1/2" Aluminum Plate
 Hemispherical Holes
 1/8" Dia. 1/16" Deep
 With Spacings as Indicated

Plate No.	A	N	M	No. of Holes
D1	0.136	87	175	15,138
D2	0.146	81	163	13,122
D3	0.156	76	153	11,552
D4	0.166	71	144	10,152
D5	0.175	68	136	9,180
D6	0.192	62	124	7,626
D7	0.222	53	107	5,618
D8	0.271	44	87	3,785

Figure 4 - Schematic of Hemispherically Dimpled Plates



NOTES:

Not to Scale

Dimensions in inches

1/2" Aluminum Plate

1/16" Deep Grooves Milled Lengthwise and Crosswise
With Spacings as Indicated

Plate No.	A	N	M
R1	1/32	91	184
R2	3/64	81	164
R3	1/16	73	147
R4	5/64	67	135
R5	3/32	61	124
R6	1/8	53	106

Figure 5 - Schematic of Rectangular Roughness Plates

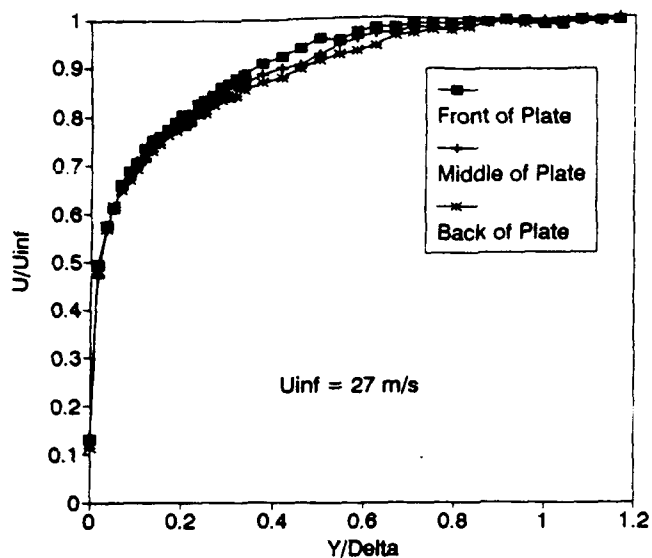


Figure 6 - Velocity Profiles On Smooth Test Plate

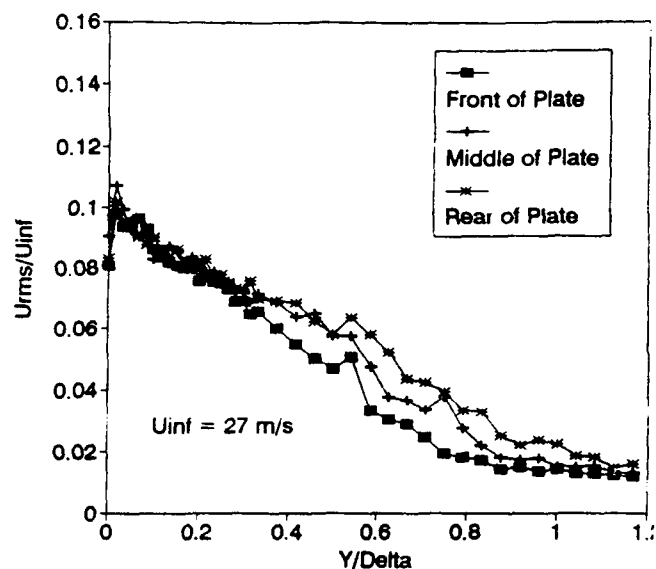


Figure 7 - Turbulence Profiles On Smooth Plate

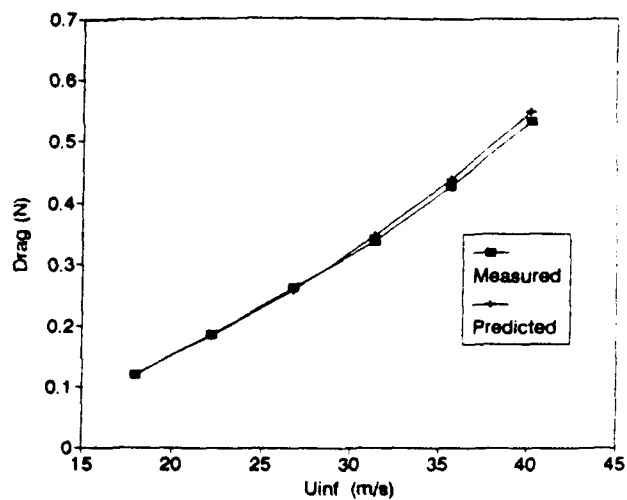


Figure 8 - Smooth Plate Drag. Comparison of Measured Vs Predicted

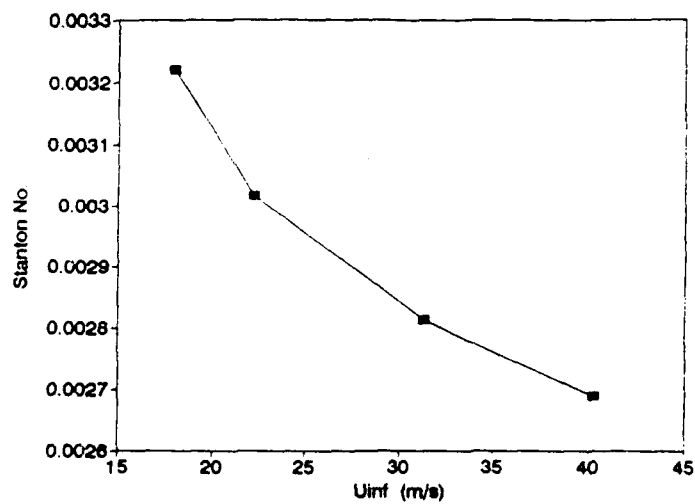


Figure 9 - Smooth Plate Stanton Number Measurement

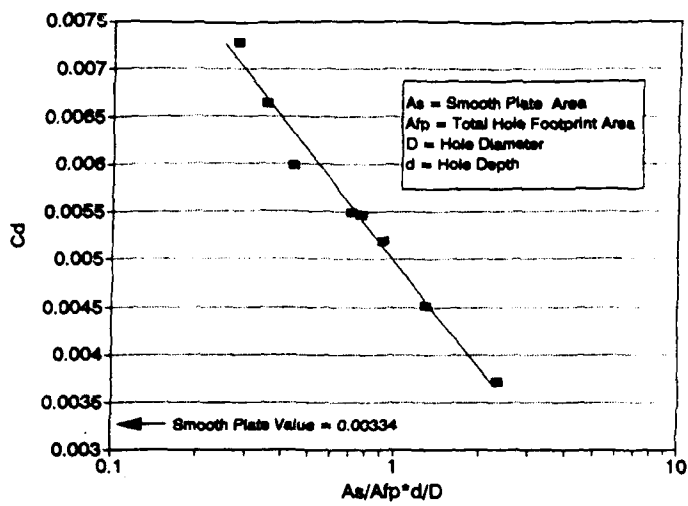


Figure 10 - C_d for Dimpled Plates

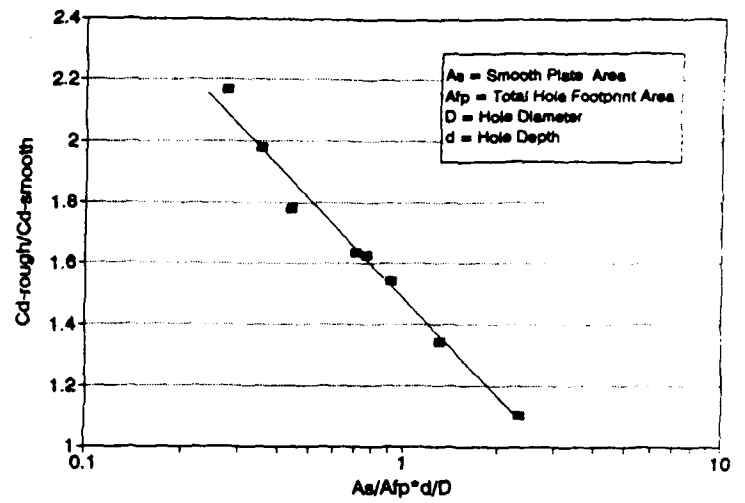


Figure 11 - Drag Augmentation for Dimpled Roughness

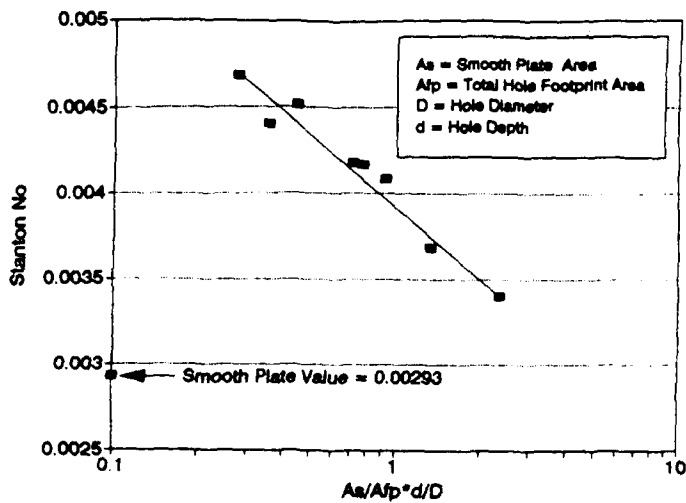


Figure 12 - Stanton Number For Dimpled Roughness

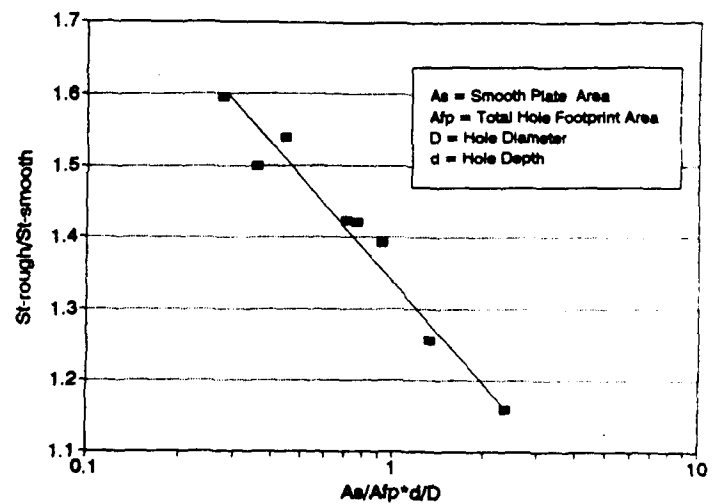


Figure 13 - Heat Transfer Augmentation for Dimpled Roughness

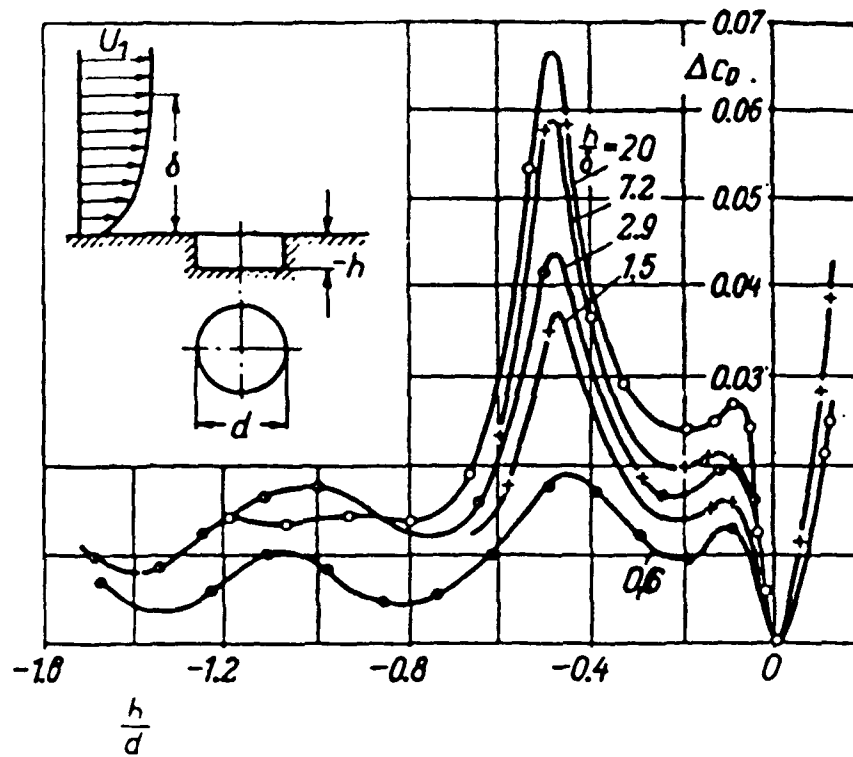


Figure 14 - Resistance Coefficient of Circular Cavities of Varying Depth in a Flat Plate as Measured by Wieghardt. Reproduced from Reference 27.

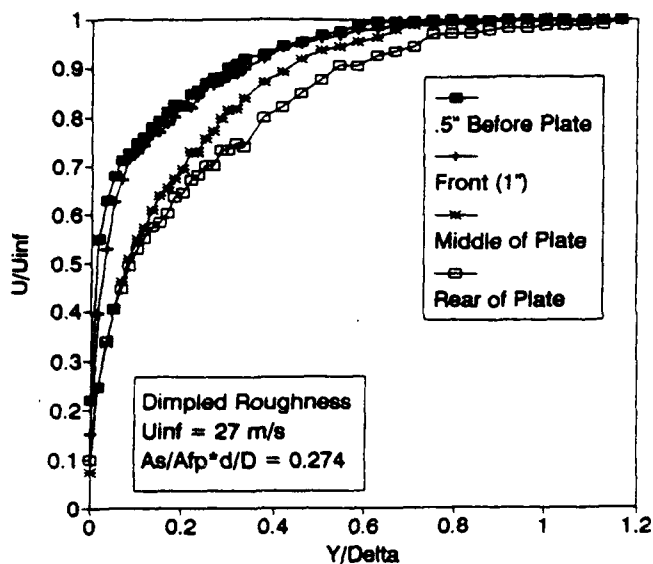


Figure 15 - Velocity Profiles for Plate D1

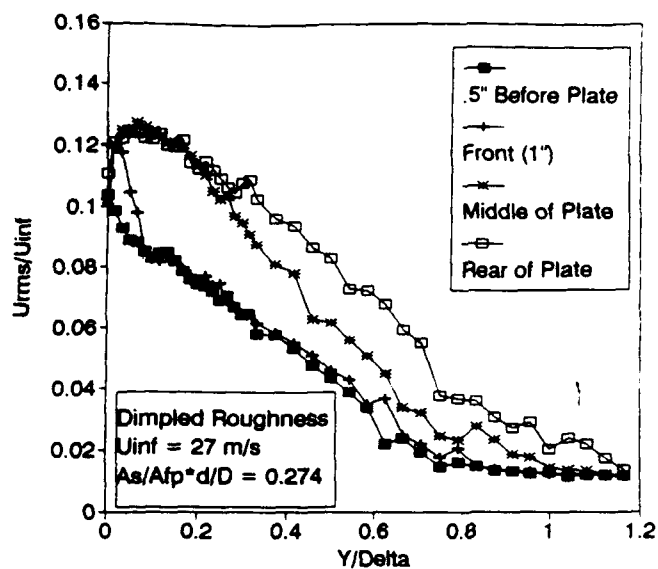


Figure 16 - Turbulence Profiles for Plate D1

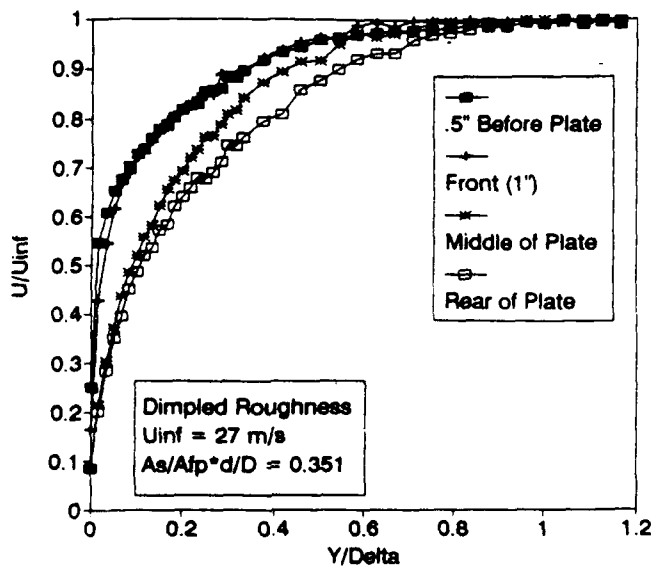


Figure 17 - Velocity Profiles for Plate D2

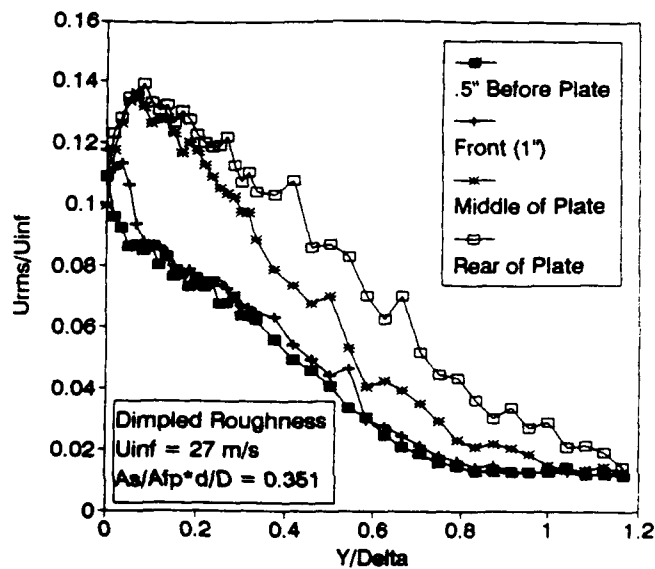


Figure 18 - Turbulence Profiles for Plate D2

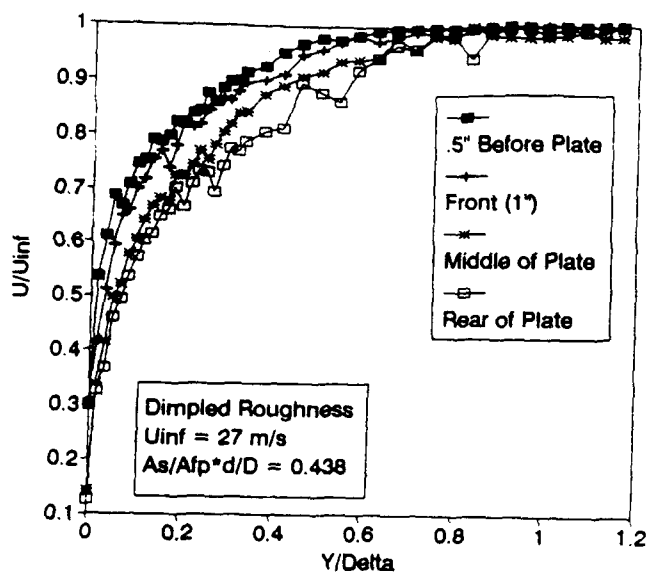


Figure 19 - Velocity Profiles for Plate D3

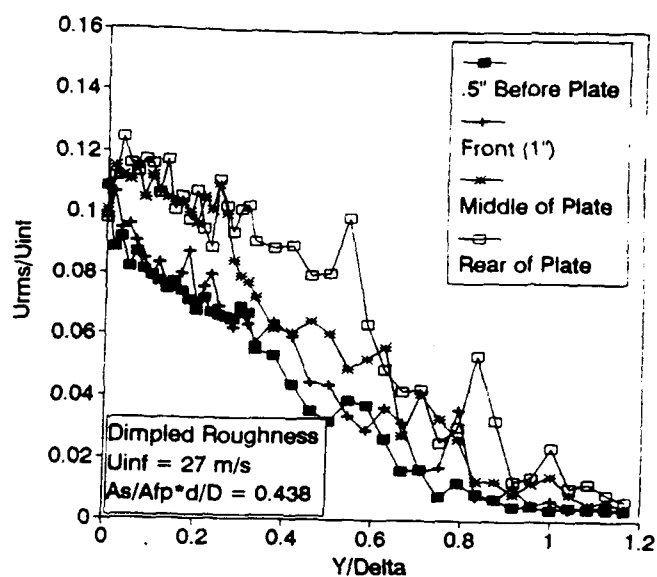


Figure 20 - Turbulence Profiles for Plate D3

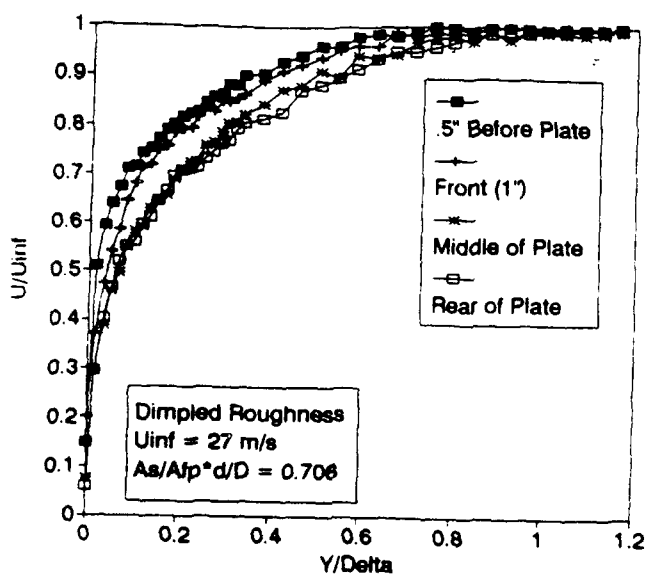


Figure 21 - Velocity Profiles for Plate D4

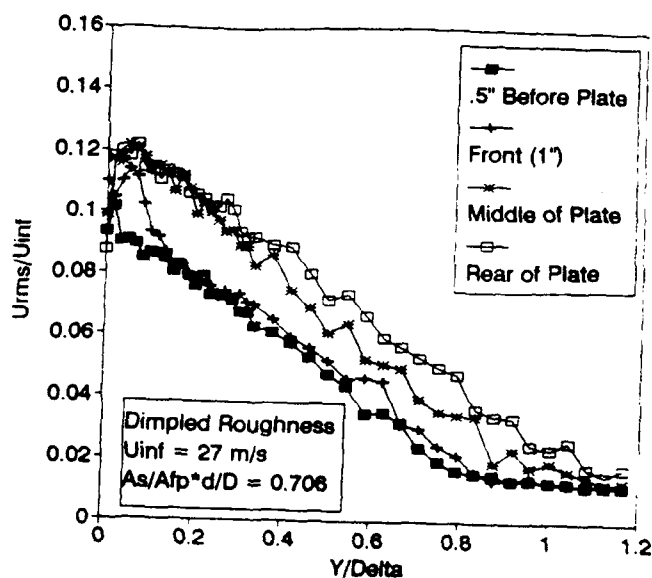


Figure 22 - Turbulence Profiles for Plate D4

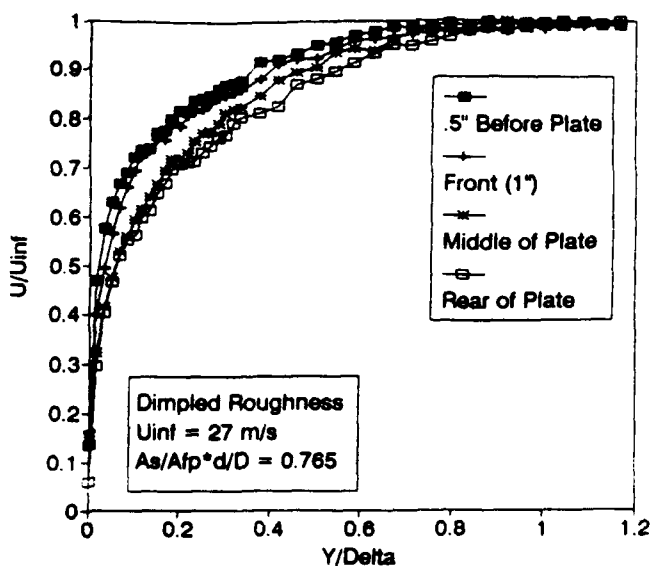


Figure 23 - Velocity Profiles for Plate D5

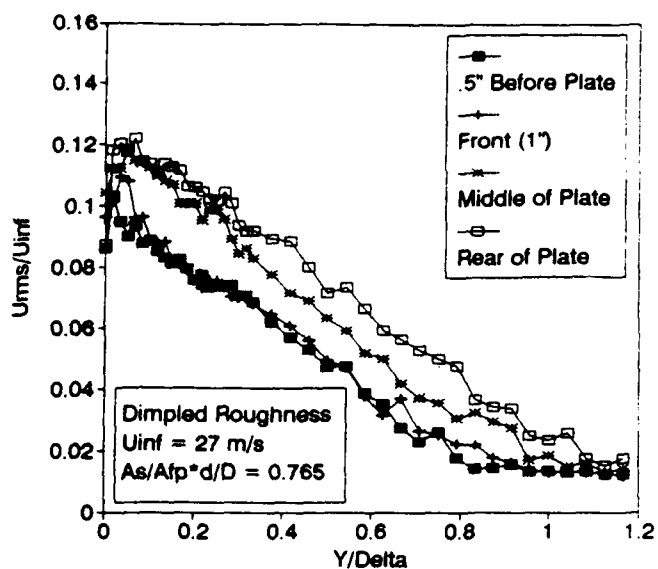


Figure 24 - Turbulence Profiles for Plate D5

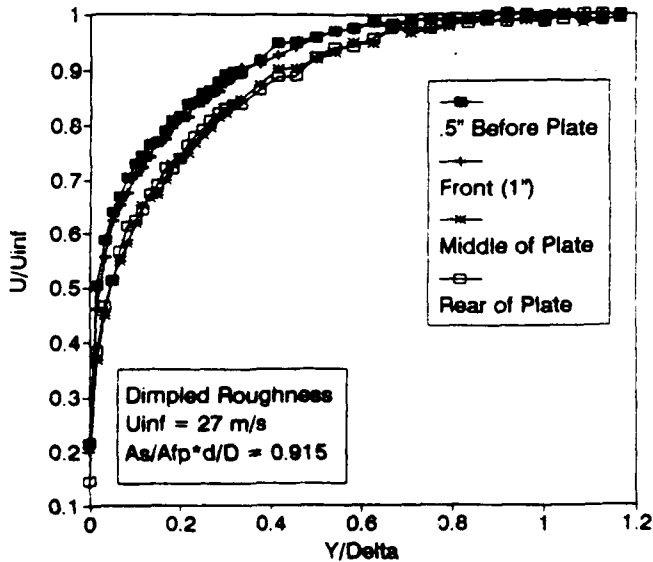


Figure 25 - Velocity Profiles for Plate D6

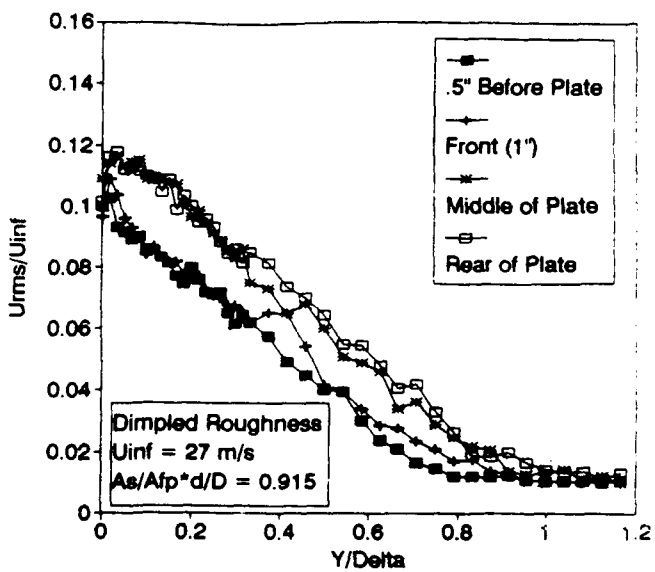


Figure 26 - Turbulence Profiles for Plate D6

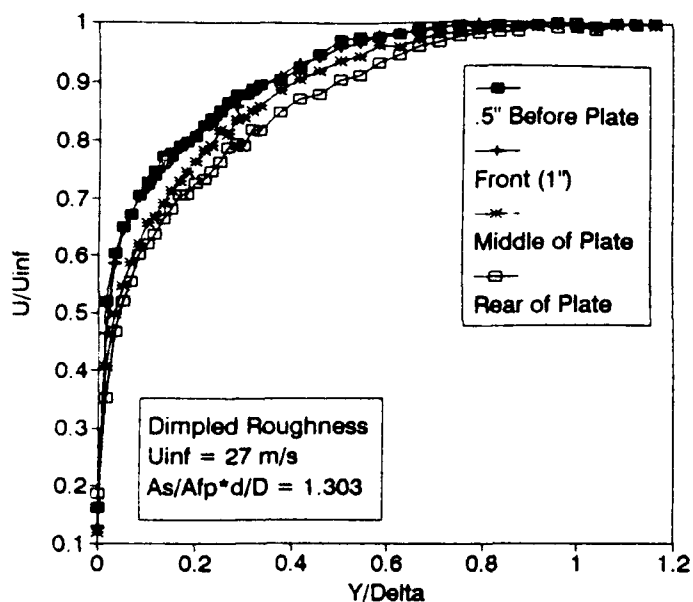


Figure 27 - Velocity Profiles for Plate D7

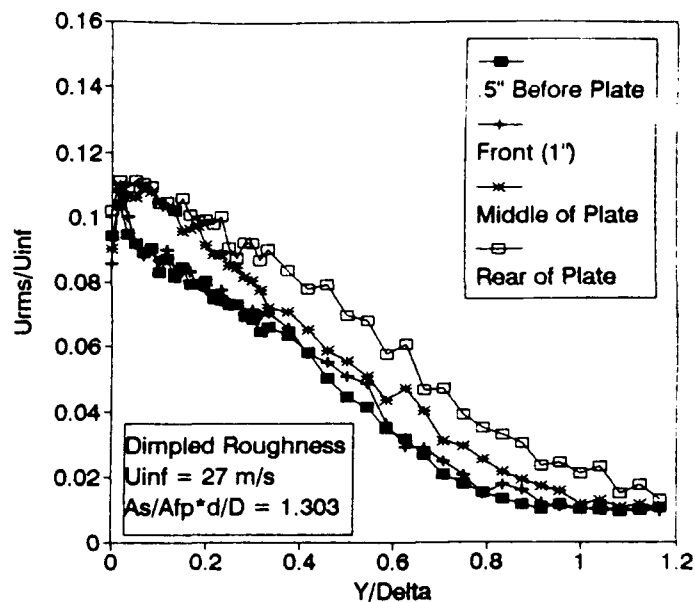


Figure 28 - Turbulence Profiles for Plate D7

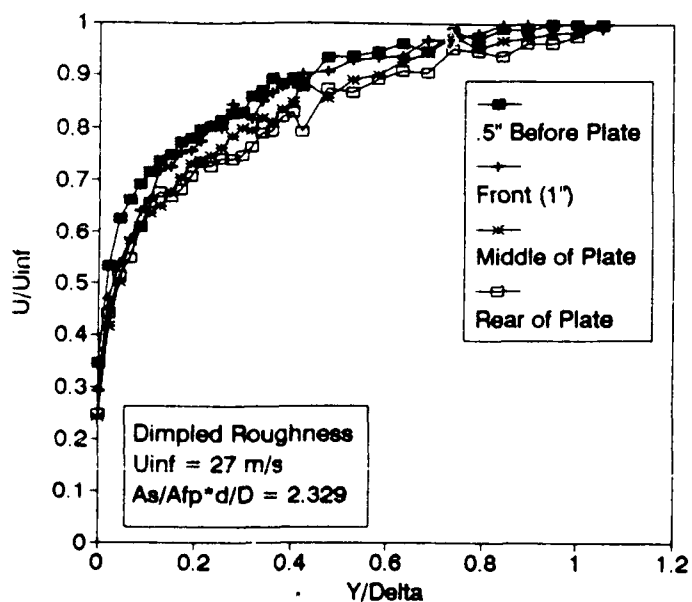


Figure 29 - Velocity Profiles for Plate D8

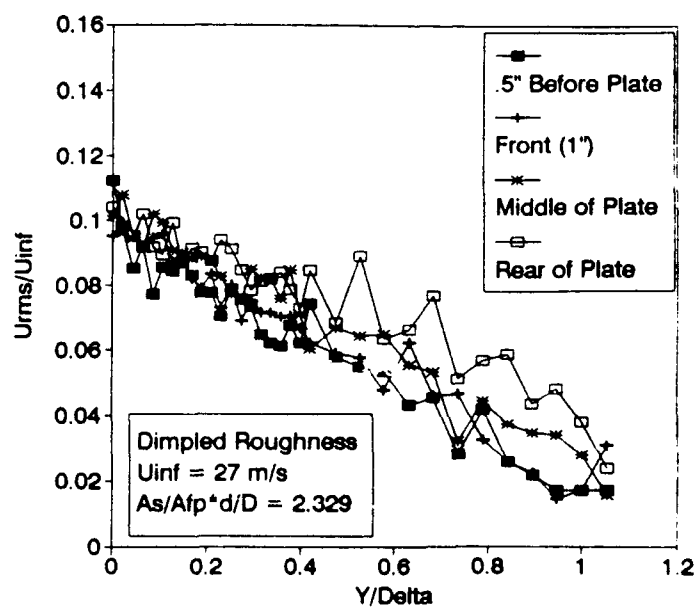


Figure 30 - Turbulence Profiles for Plate D8

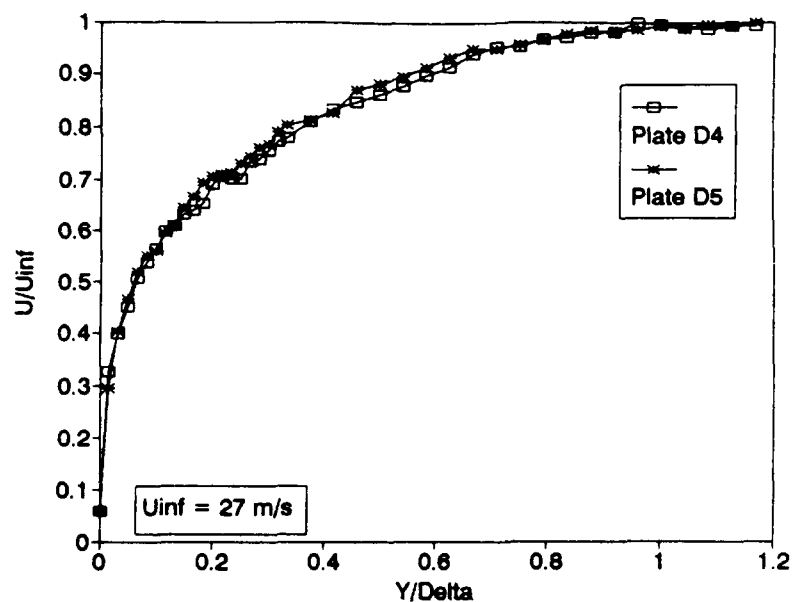


Figure 31 - Comparison of Velocity Profiles at Rear of Plates D4 and D5

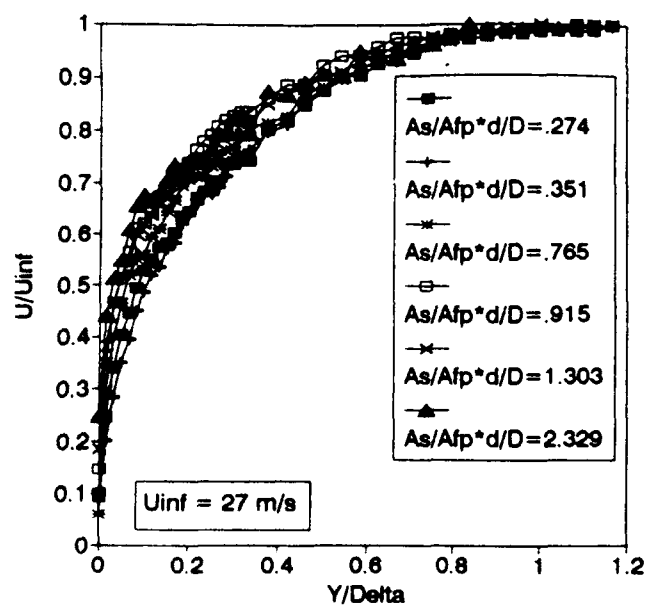


Figure 32 - Comparison of Velocity Profiles at Rear of Dimpled Roughness Plates

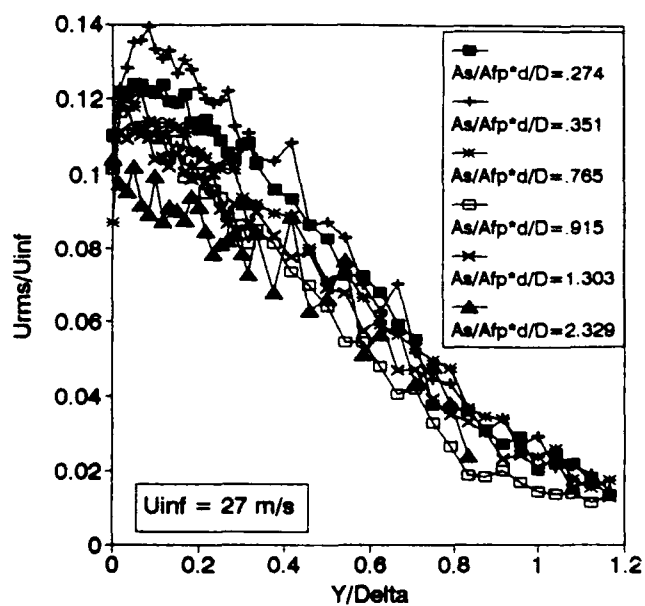


Figure 33 - Comparison of Turbulence Profiles at Rear of Dimpled Roughness Plates

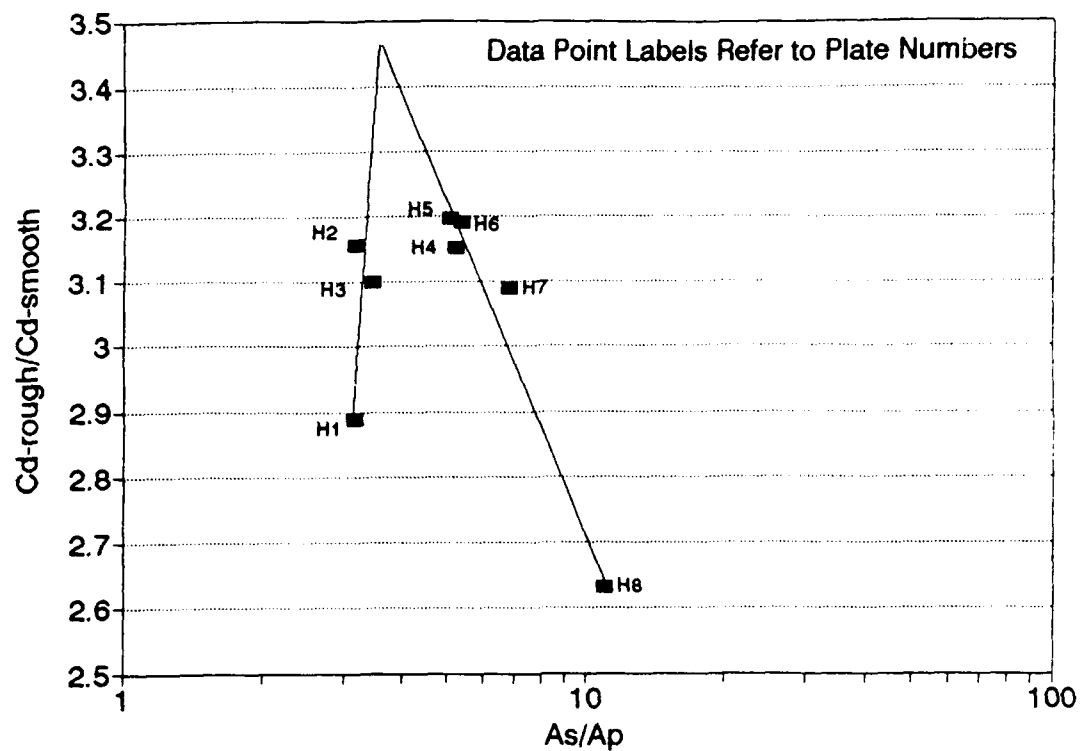


Figure 34 - Drag Augmentation for Hemispherical Roughness

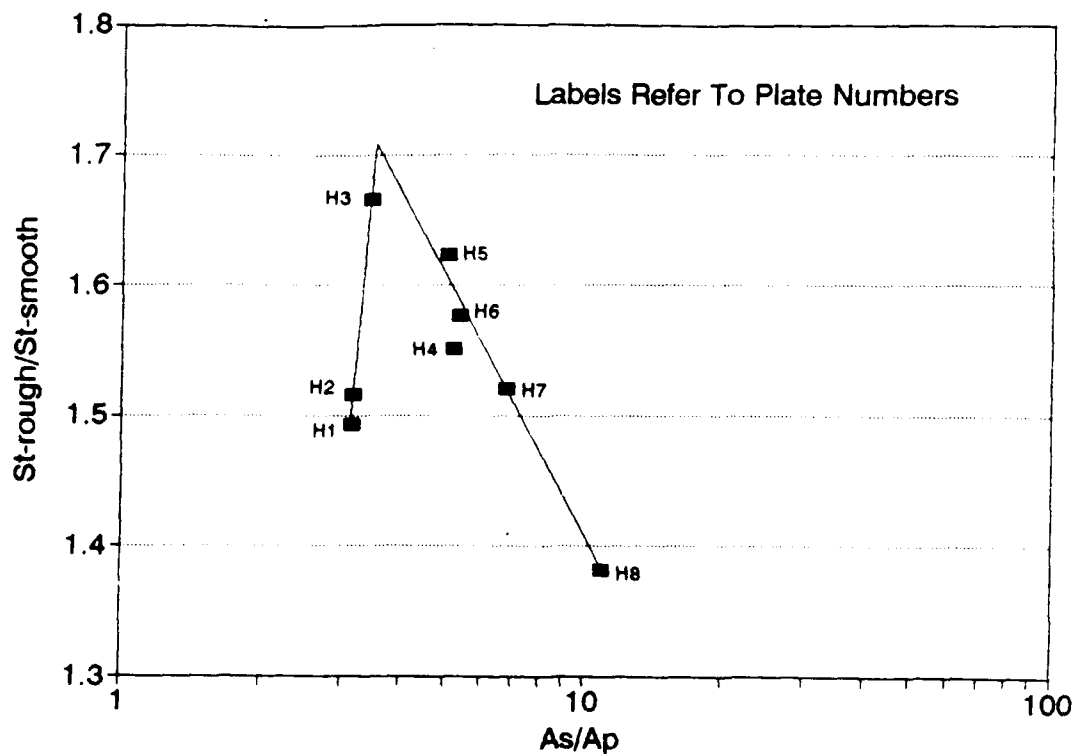


Figure 35 - Heat Transfer Augmentation for Hemispherical Roughness

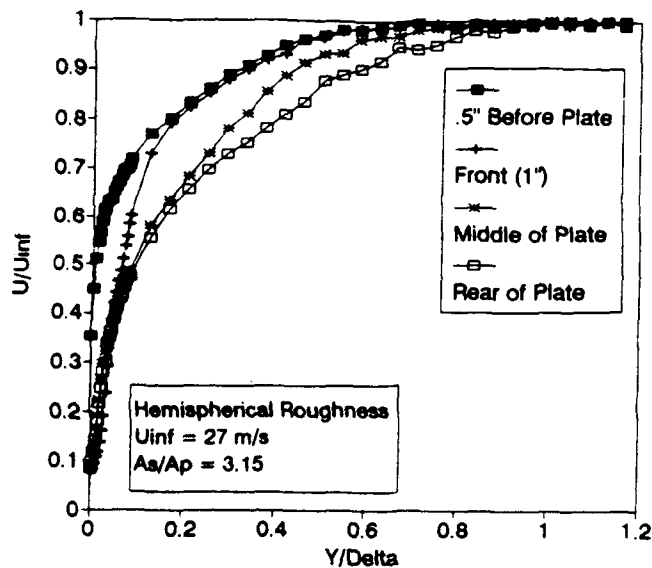


Figure 36 - Velocity Profiles for Plate H1

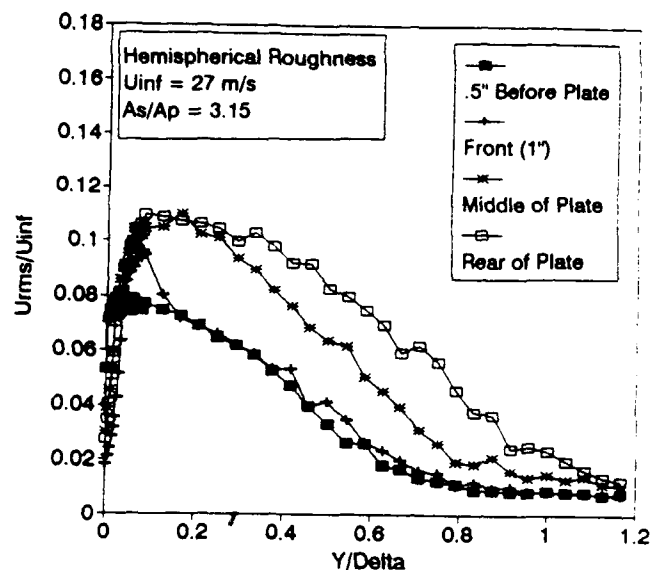


Figure 37 - Turbulence Profiles for Plate H1

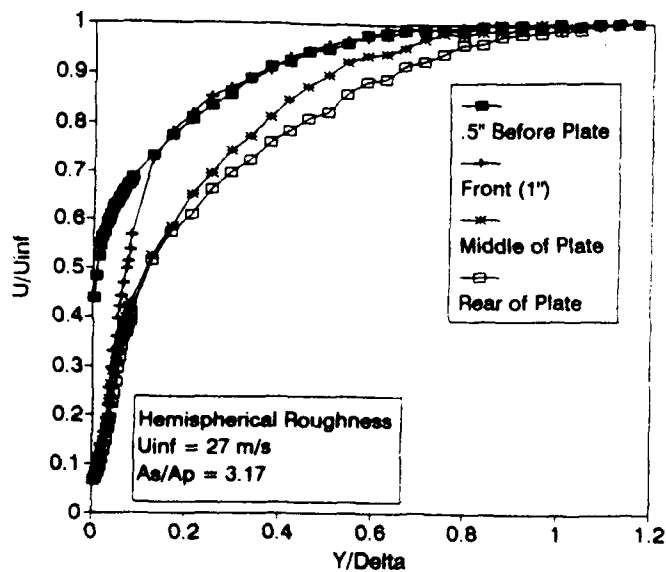


Figure 38 - Velocity Profiles for Plate H2

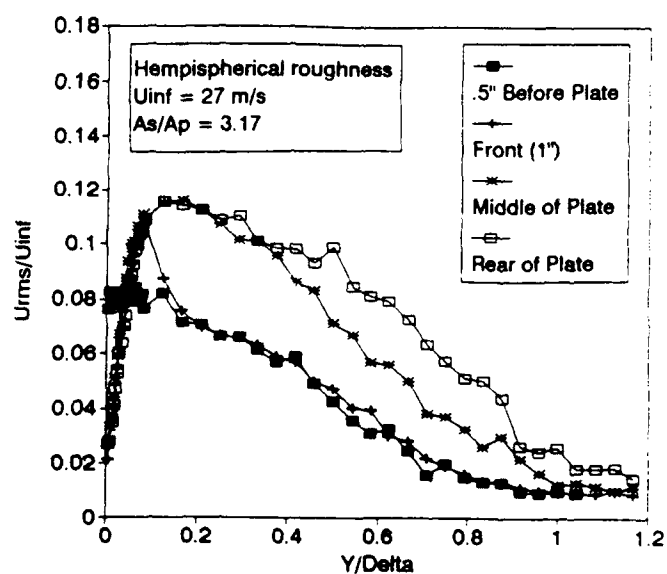


Figure 39 - Turbulence Profiles for Plate H2

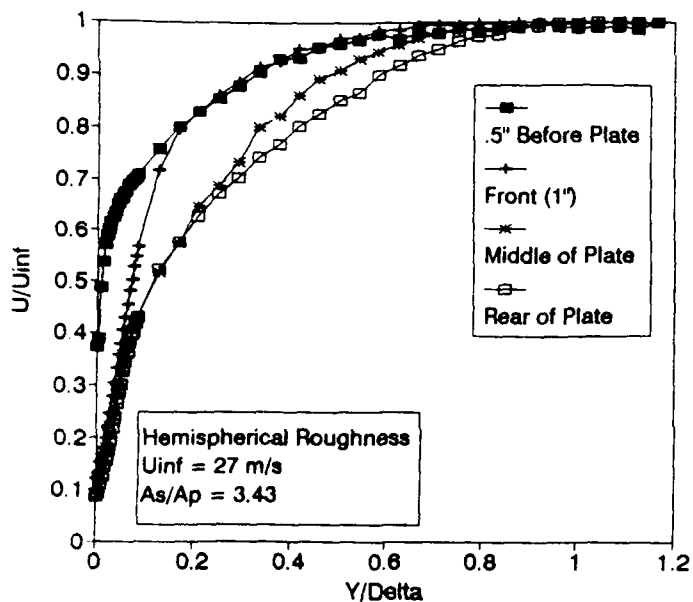


Figure 40 - Velocity Profiles for Plate H3

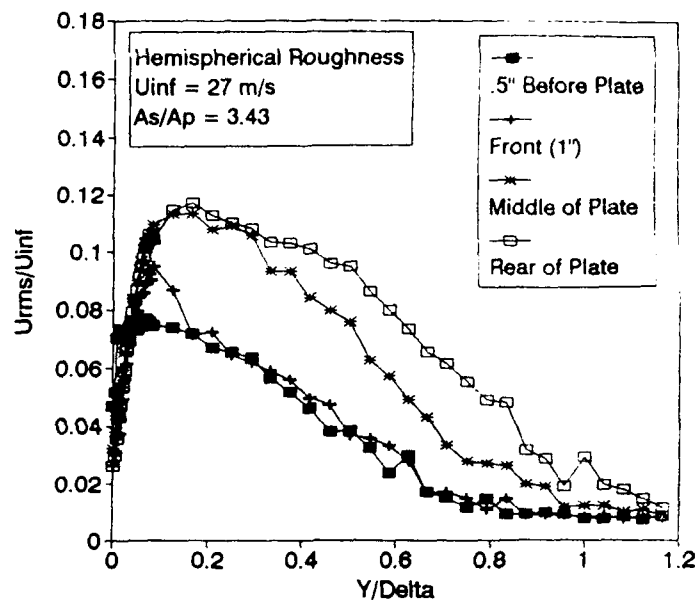


Figure 41 - Turbulence Profiles for Plate H3

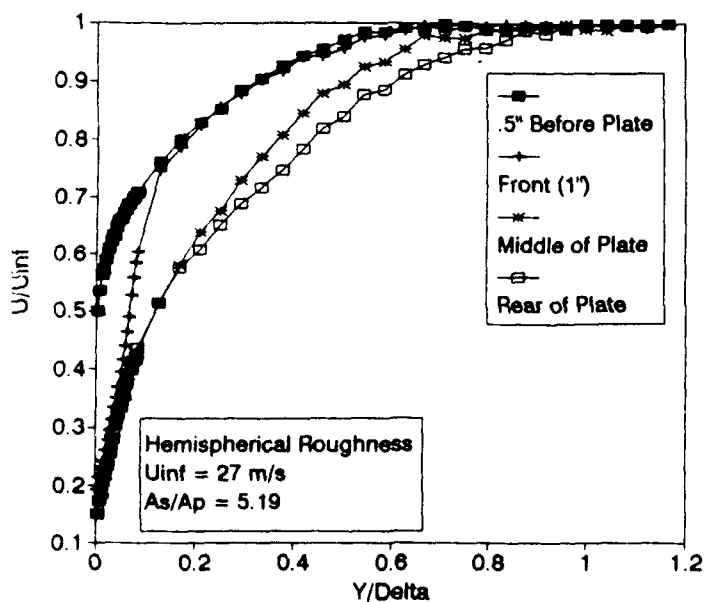


Figure 42 - Velocity Profiles for Plate H4

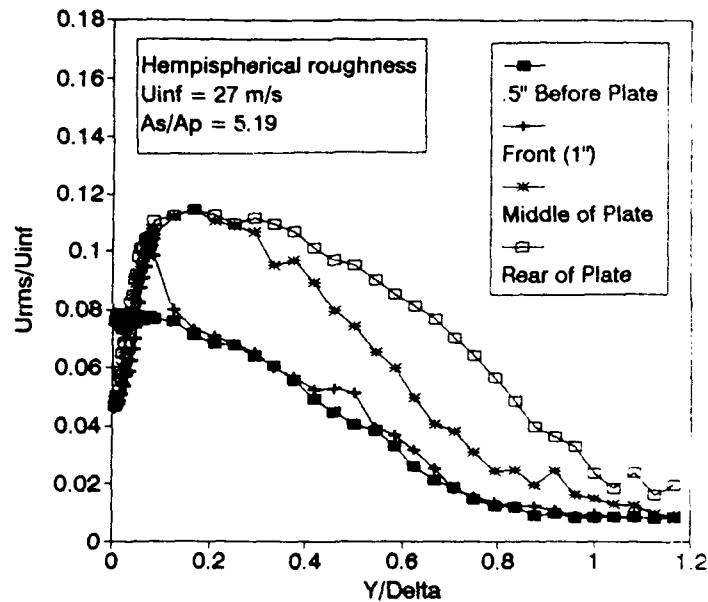


Figure 43 - Turbulence Profiles for Plate H4

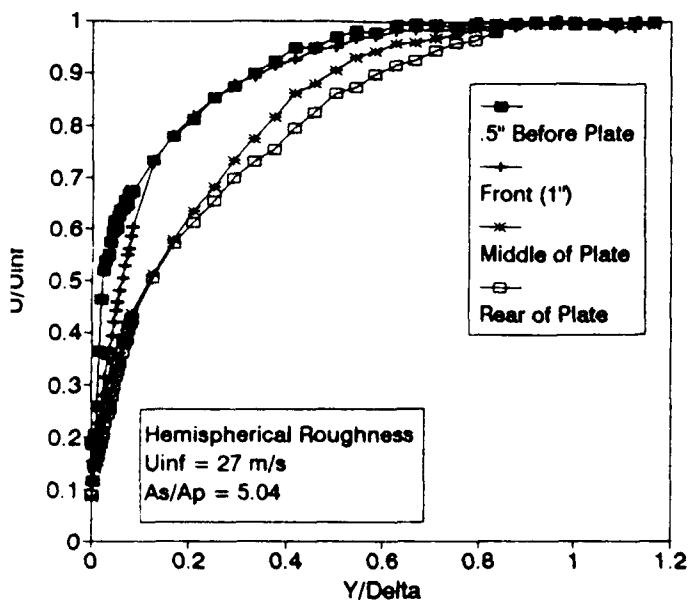


Figure 44 - Velocity Profiles for Plate H5

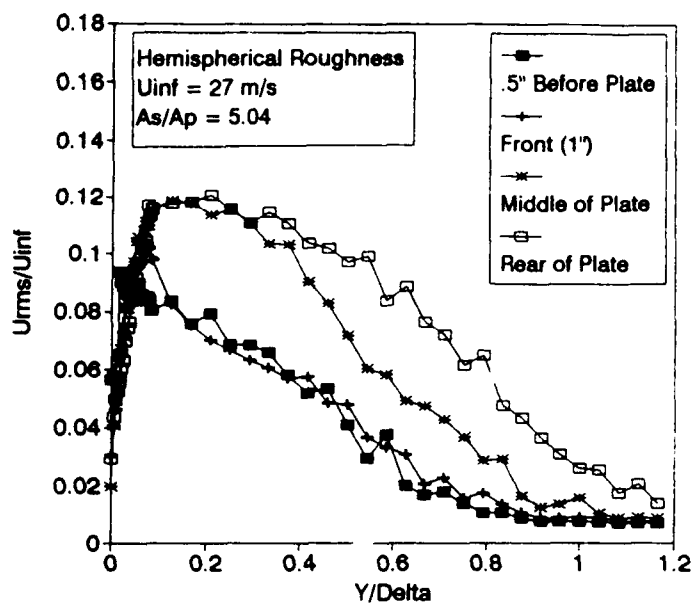


Figure 45 - Turbulence Profiles for Plate H5

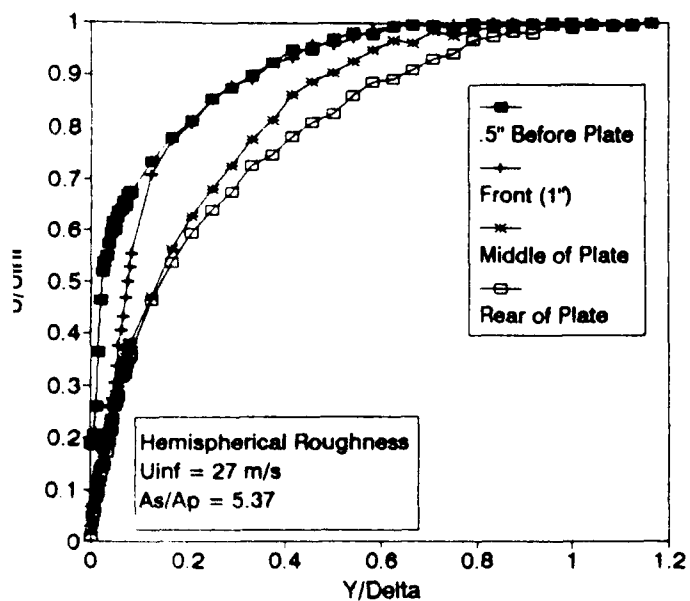


Figure 46 - Velocity Profiles for Plate H6

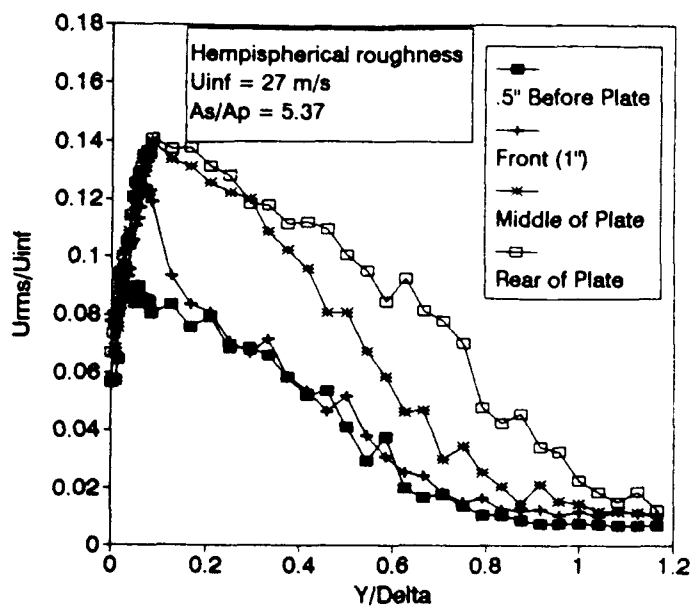


Figure 47 - Turbulence Profiles for Plate H6

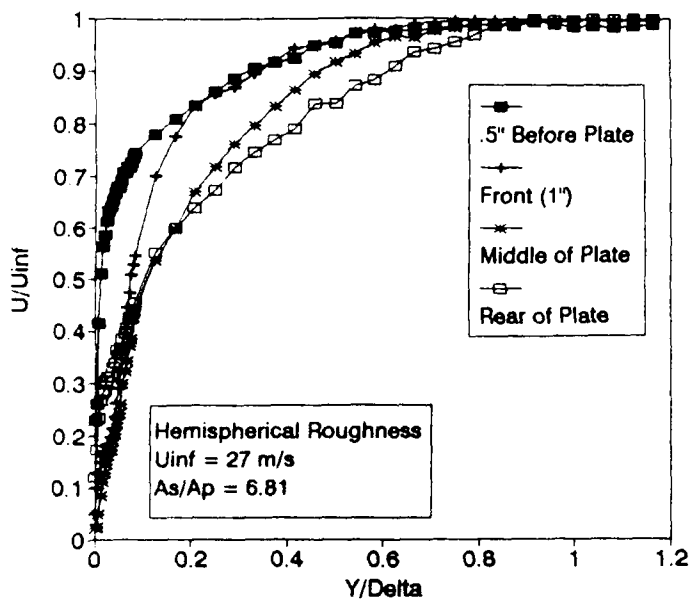


Figure 48 - Velocity Profiles for Plate H7

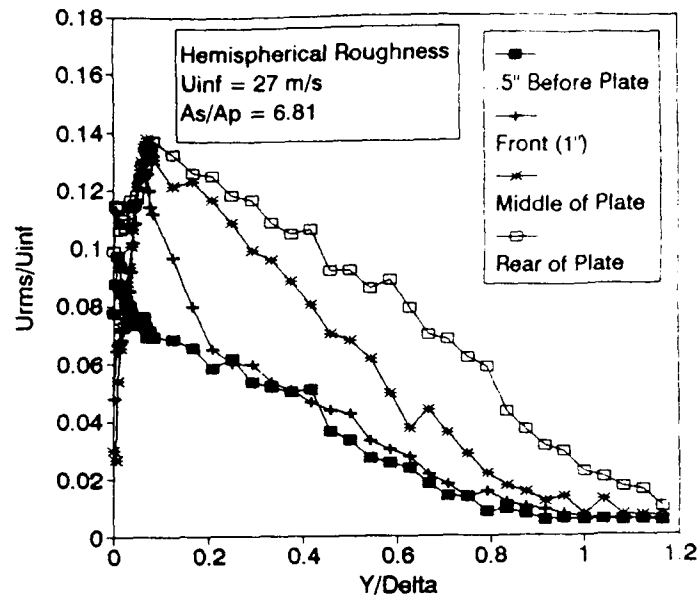


Figure 49 - Turbulence Profiles for Plate H7

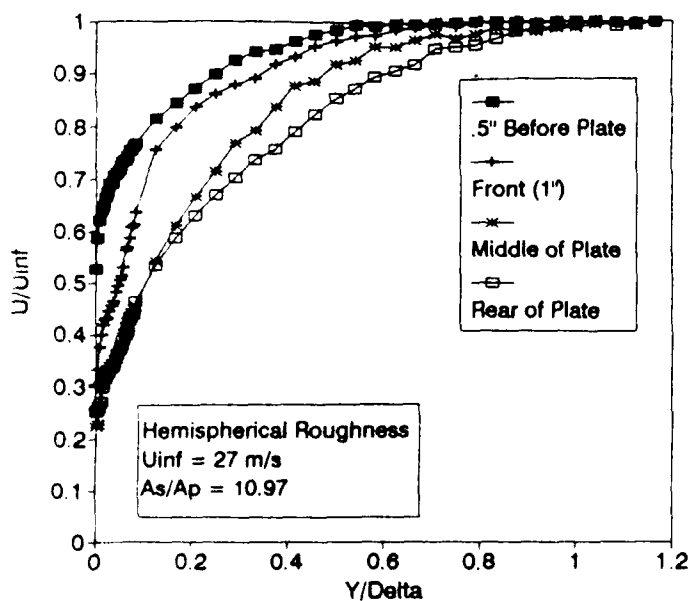


Figure 50 - Velocity Profiles for Plate H8

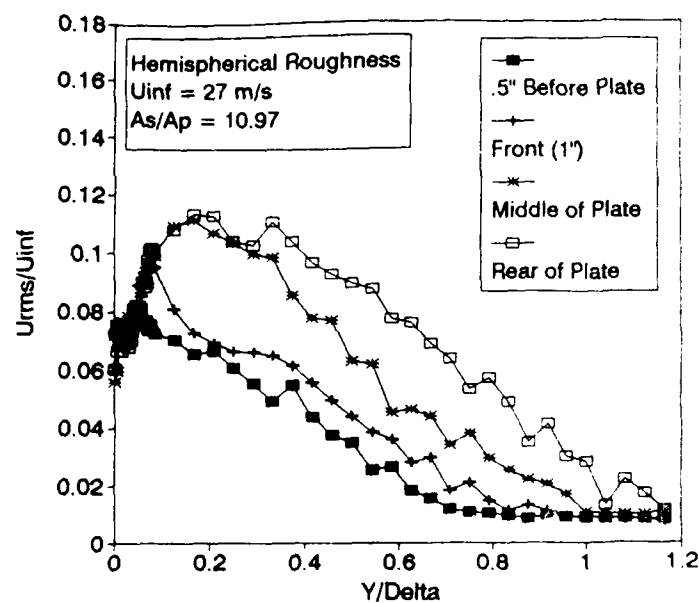


Figure 51 - Turbulence Profiles for Plate H8

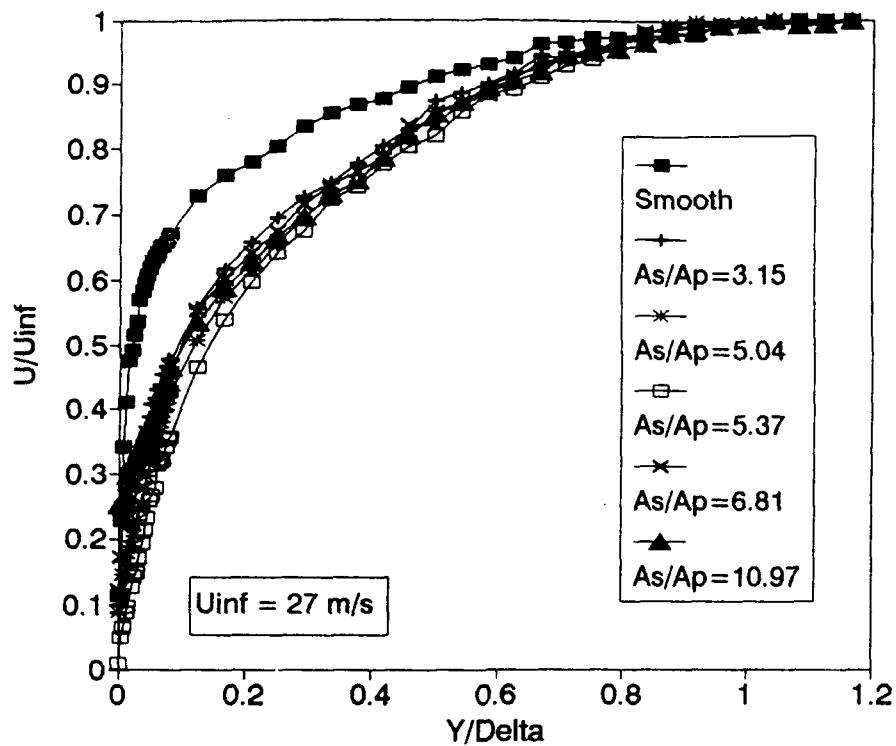


Figure 52 - Comparison of Velocity Profiles at Rear of Hemispherical Roughness Plates

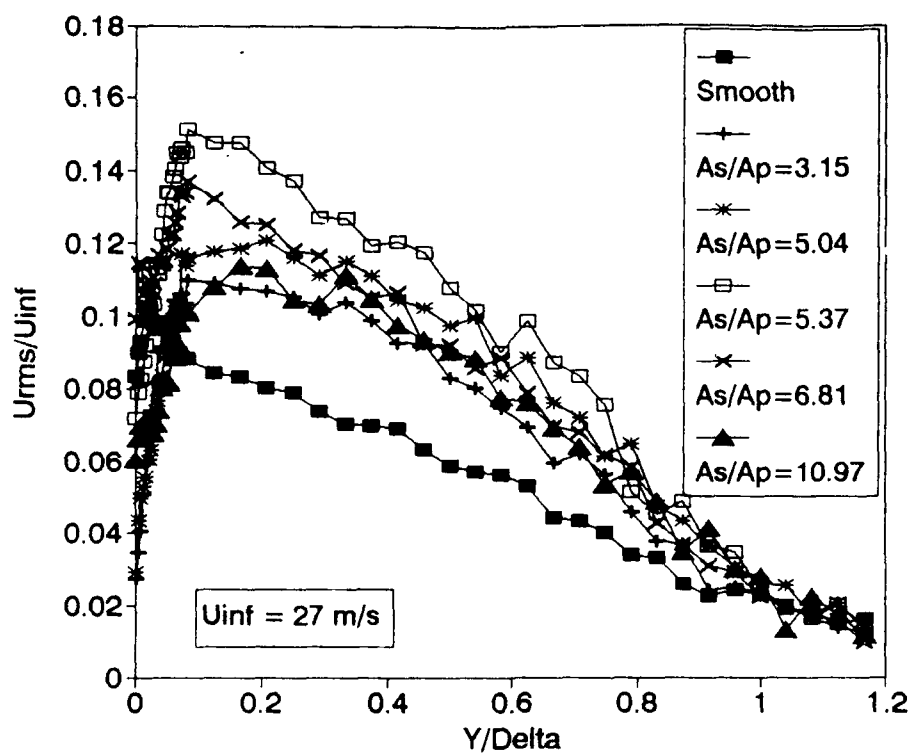


Figure 53 - Comparison of Turbulence Profiles at Rear of Hemispherical Roughness Plates

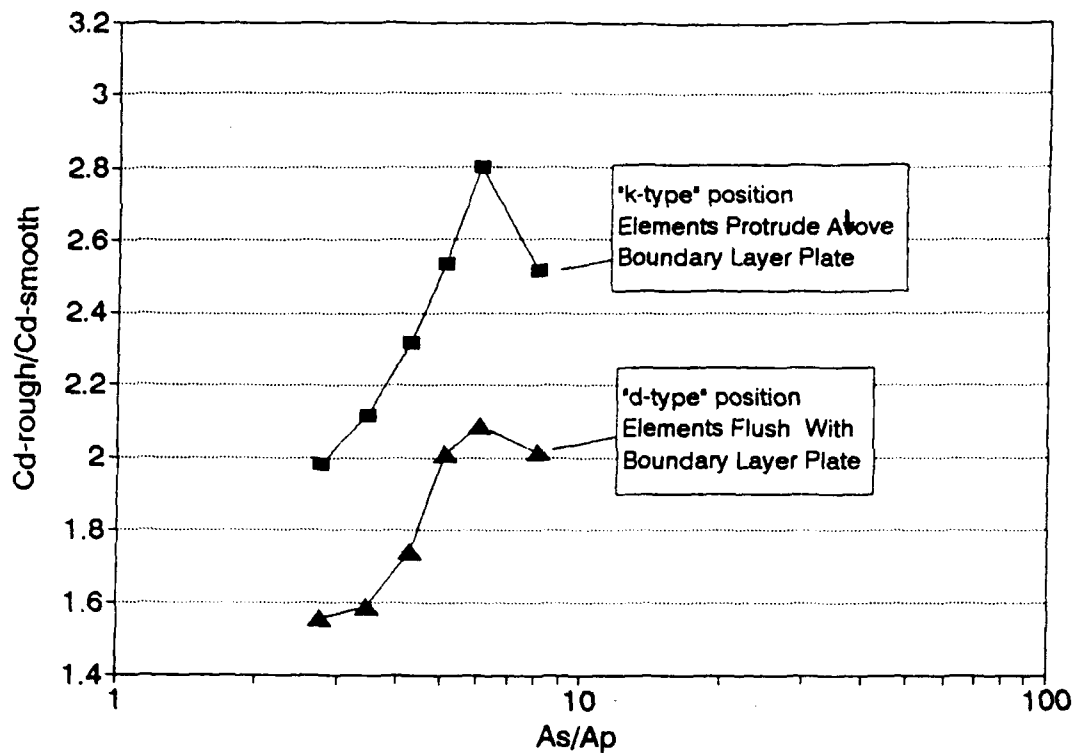


Figure 54 - Drag Augmentation for Rectangular Roughness

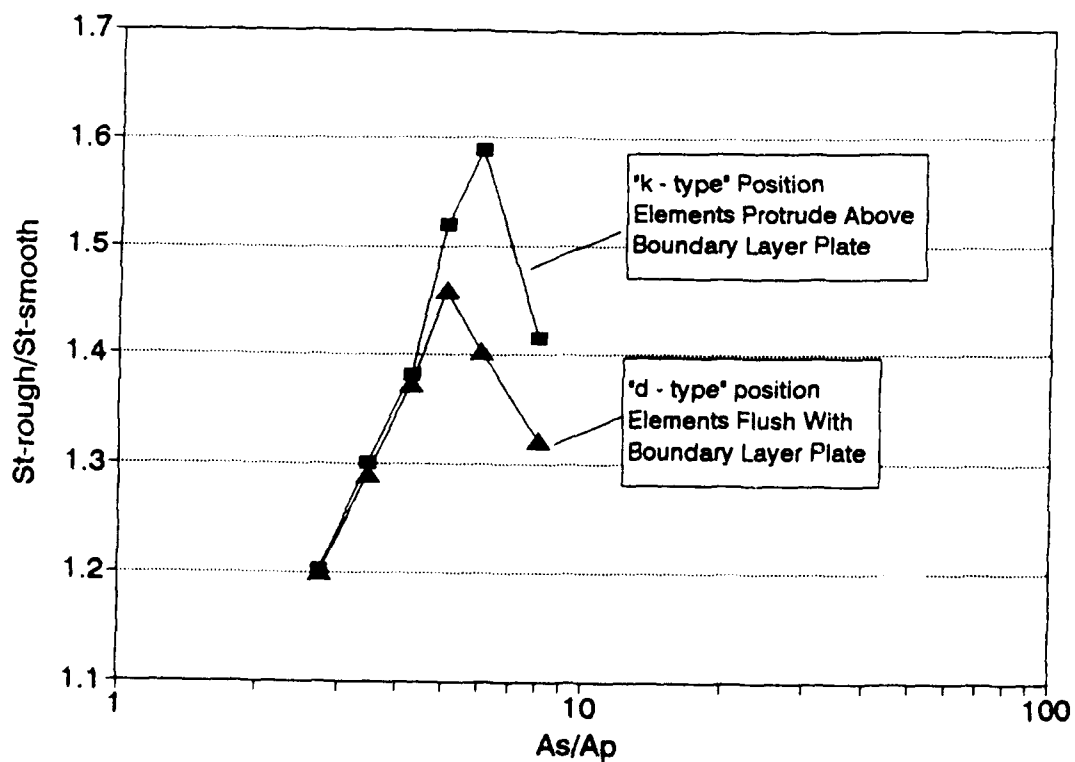


Figure 55 - Heat Transfer Augmentation for Rectangular Roughness

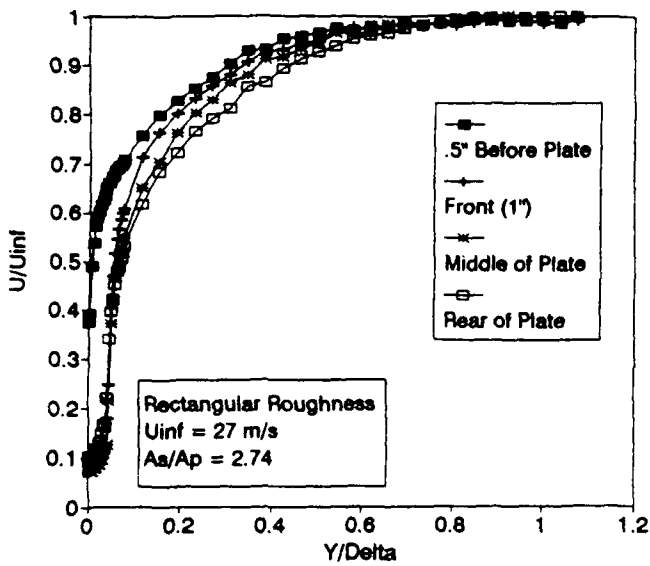


Figure 56 - Velocity Profiles for Plate R1
with the Elements Flush with the Boundary Layer Plate

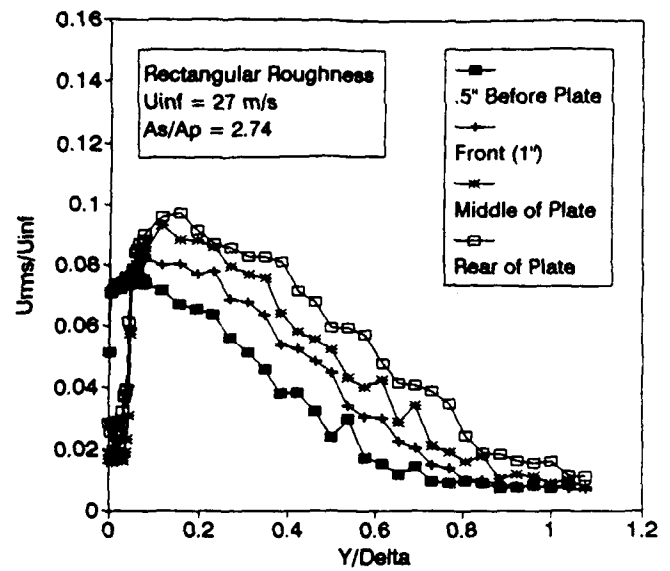


Figure 57 - Turbulence Profiles for Plate R1
with the Elements Flush with the Boundary Layer Plate

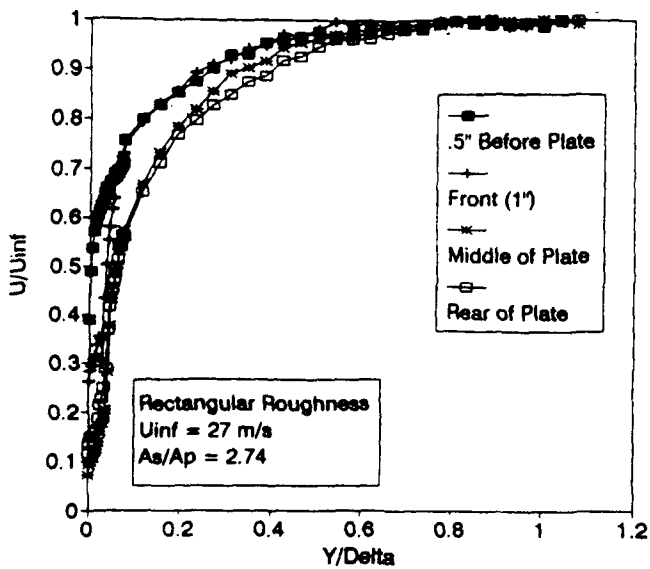


Figure 58 - Velocity Profiles for Plate R1
with the Elements Above the Boundary Layer Plate

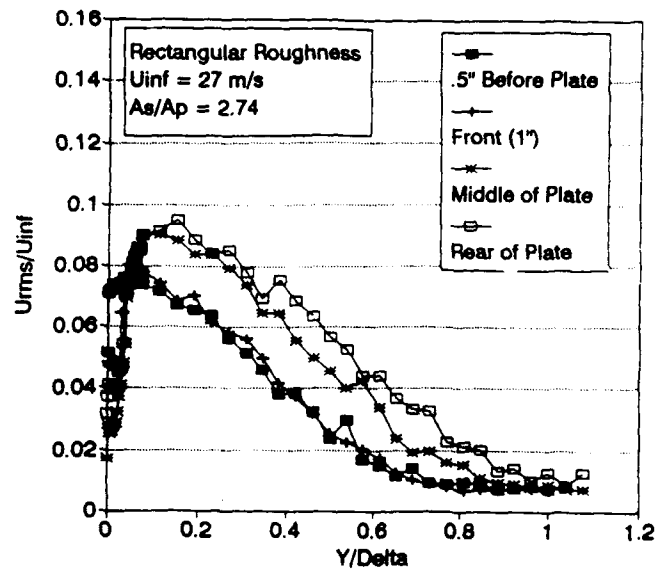


Figure 59 - Turbulence Profiles for Plate R1
with the Elements Above the Boundary Layer Plate

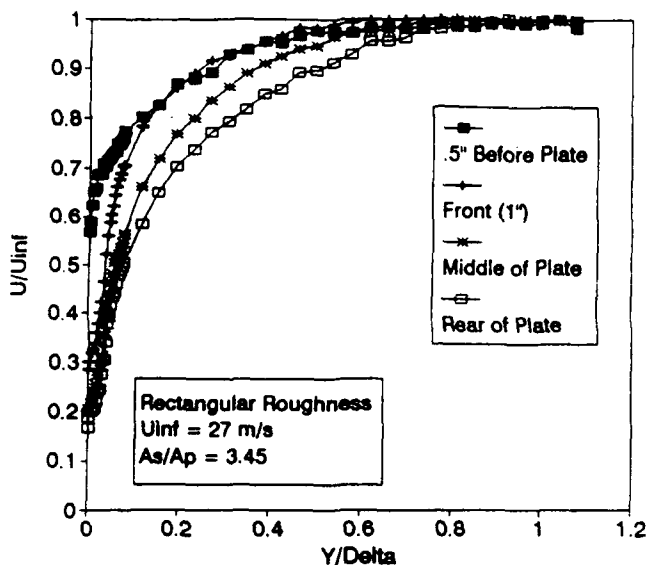


Figure 60 - Velocity Profiles for Plate R2
with the Elements Flush with the Boundary Layer Plate

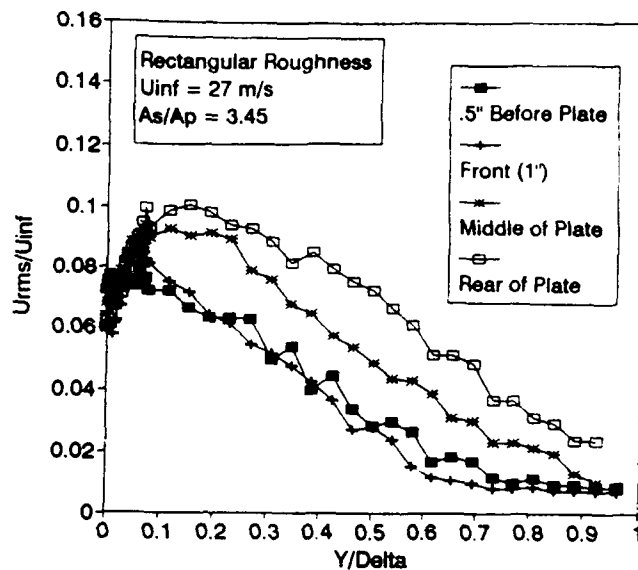


Figure 61 - Turbulence Profiles for Plate R2
with the Elements Flush with the Boundary Layer Plate

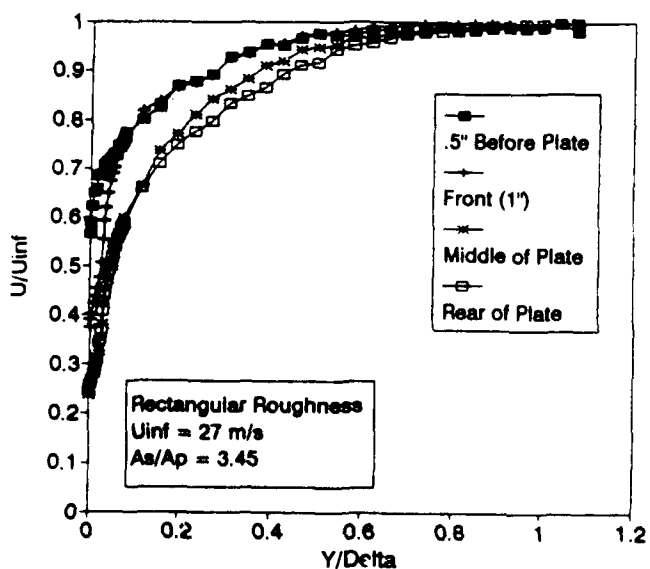


Figure 62 - Velocity Profiles for Plate R2
with the Elements Above the Boundary Layer Plate

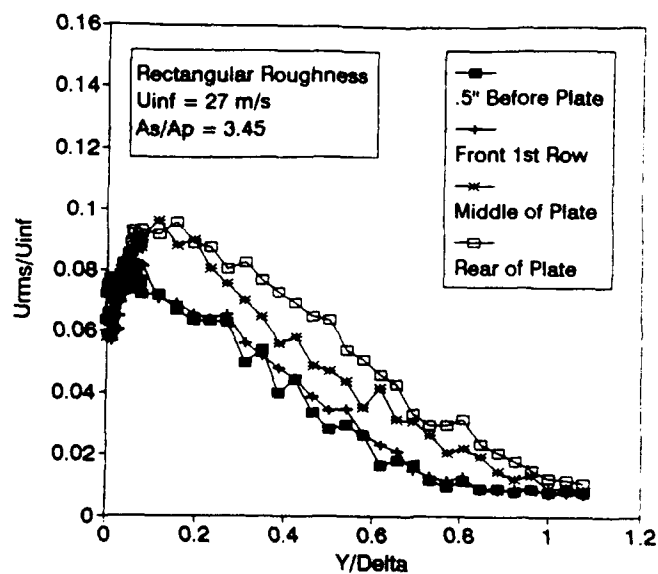


Figure 63 - Turbulence Profiles for Plate R2
with the Elements Above the Boundary Layer Plate

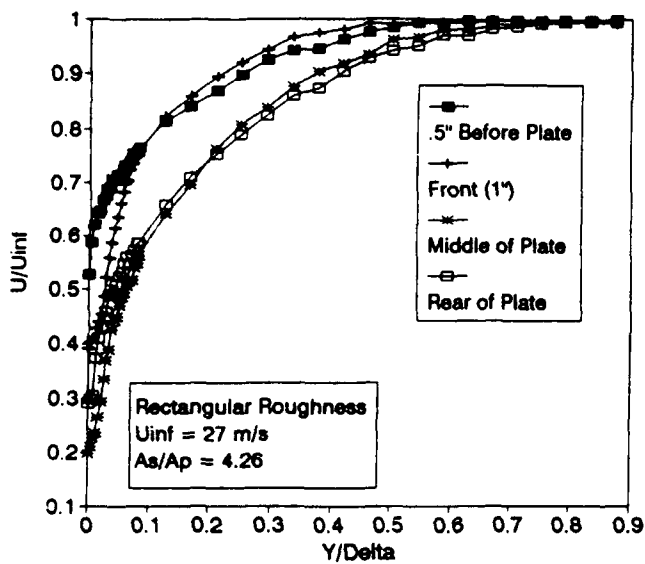


Figure 64 - Velocity Profiles for Plate R3 with the Elements Flush with the Boundary Layer Plate

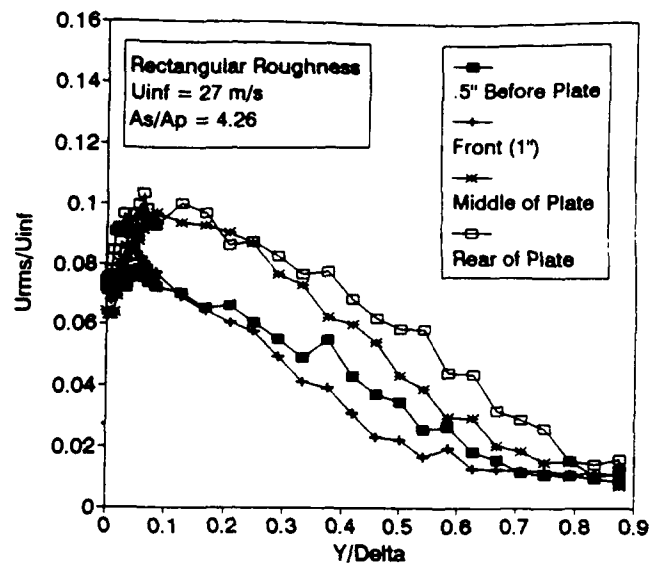


Figure 65 - Turbulence Profiles for Plate R3 with the Elements Flush with the Boundary Layer Plate

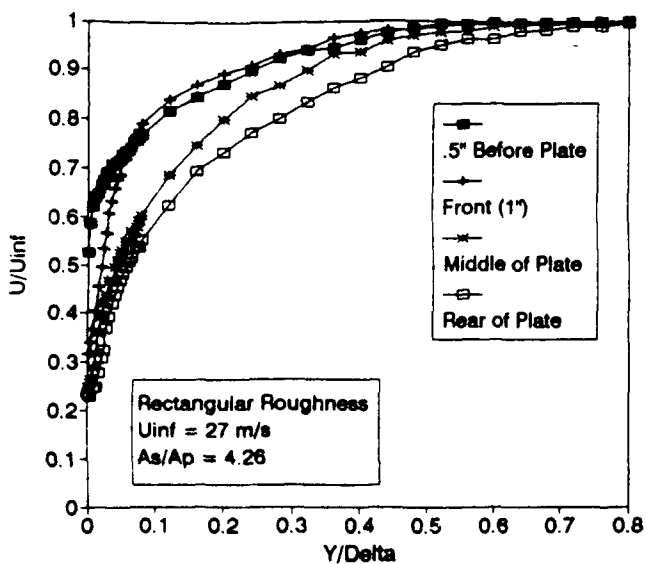


Figure 66 - Velocity Profiles for Plate R3 with the Elements Above the Boundary Layer Plate

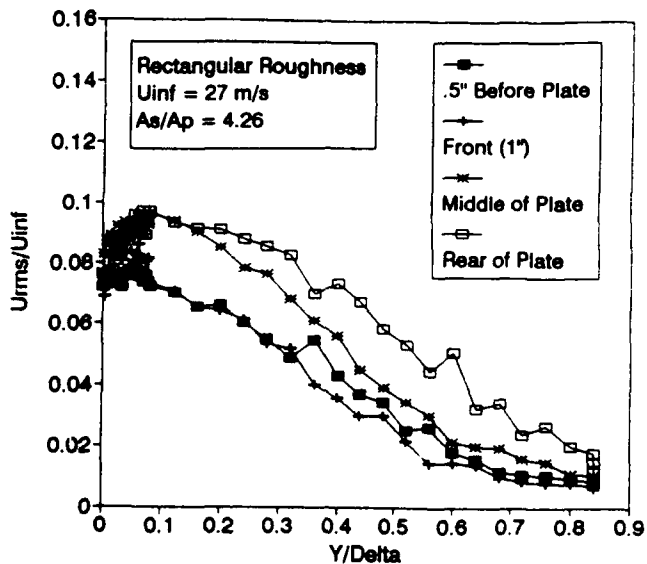


Figure 67 - Turbulence Profiles for Plate R3 with the Elements Above the Boundary Layer Plate

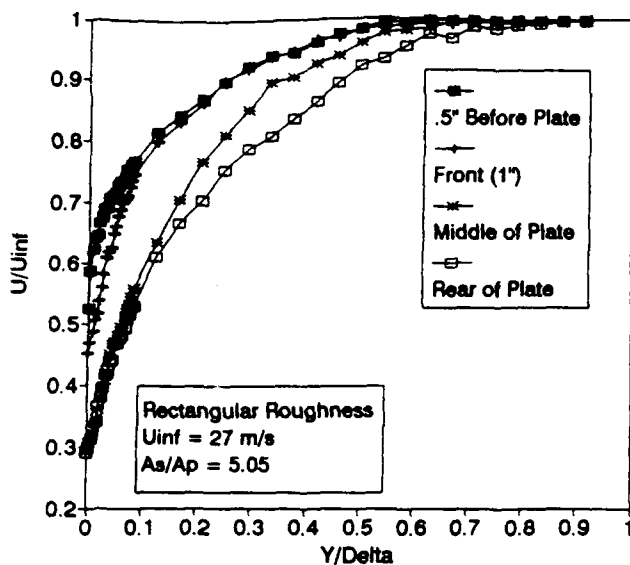


Figure 68 - Velocity Profiles for Plate R4
with the Elements Flush with the Boundary Layer Plate

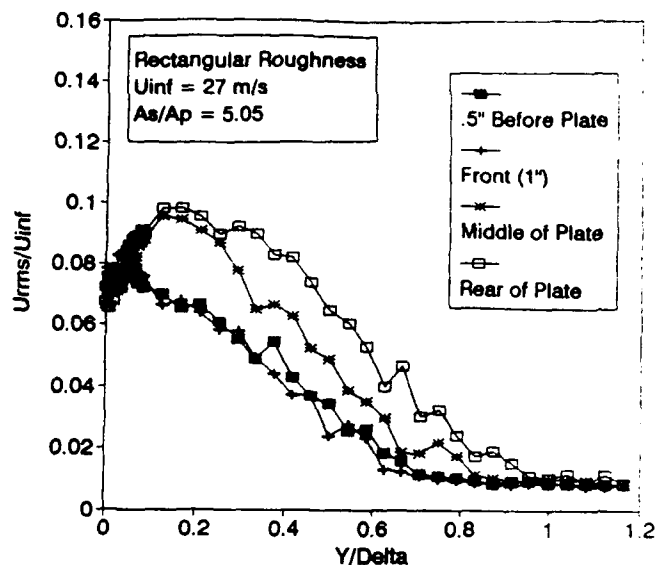


Figure 69 - Turbulence Profiles for Plate R4
with the Elements Flush with the Boundary Layer Plate

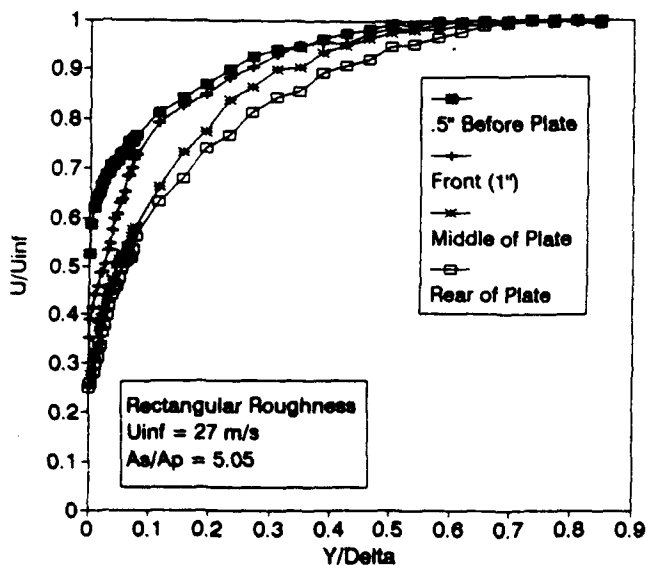


Figure 70 - Velocity Profiles for Plate R4
with the Elements Above the Boundary Layer Plate

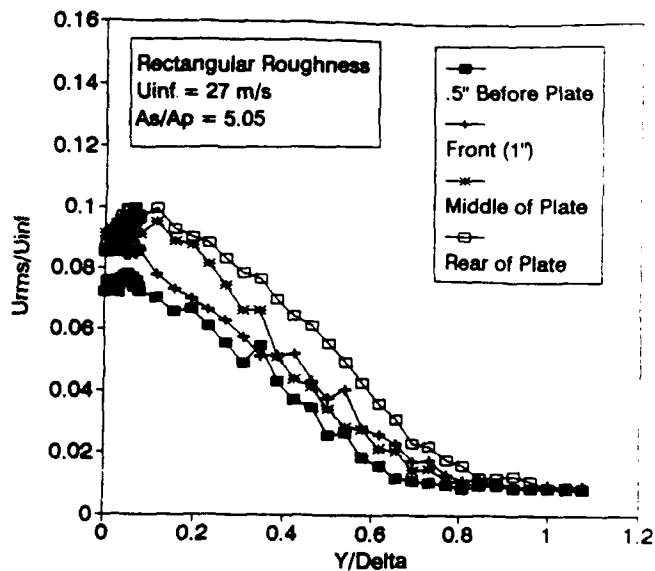


Figure 71 - Turbulence Profiles for Plate R4
with the Elements Above the Boundary Layer Plate

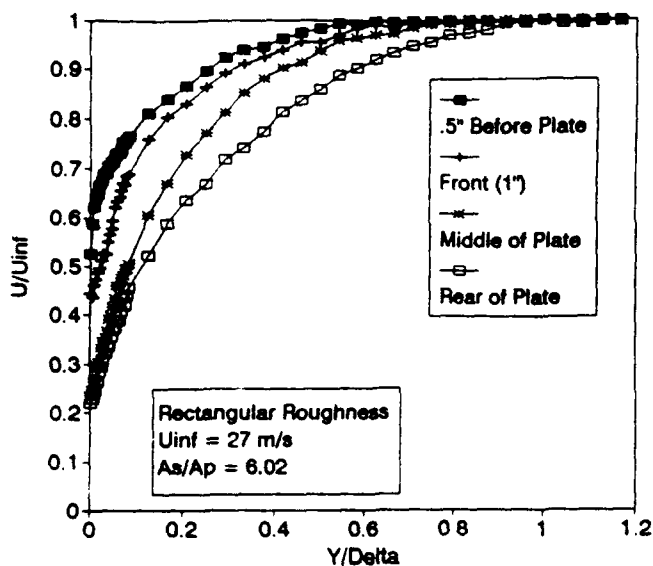


Figure 72 - Velocity Profiles for Plate R5
with the Elements Flush with the Boundary Layer Plate

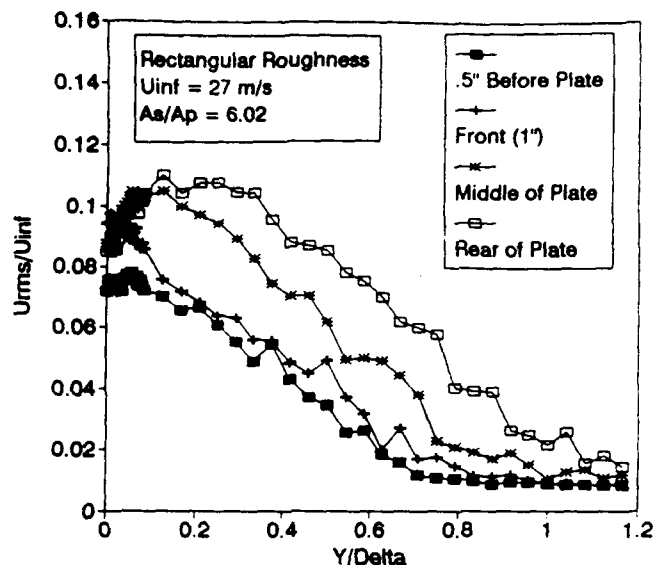


Figure 73 - Turbulence Profiles for Plate R5
with the Elements Flush with the Boundary Layer Plate

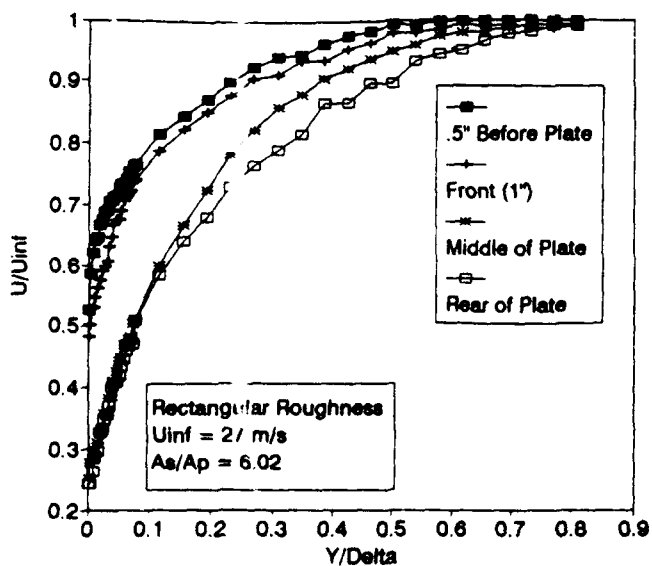


Figure 74 - Velocity Profiles for Plate R5
with the Elements Above the Boundary Layer Plate

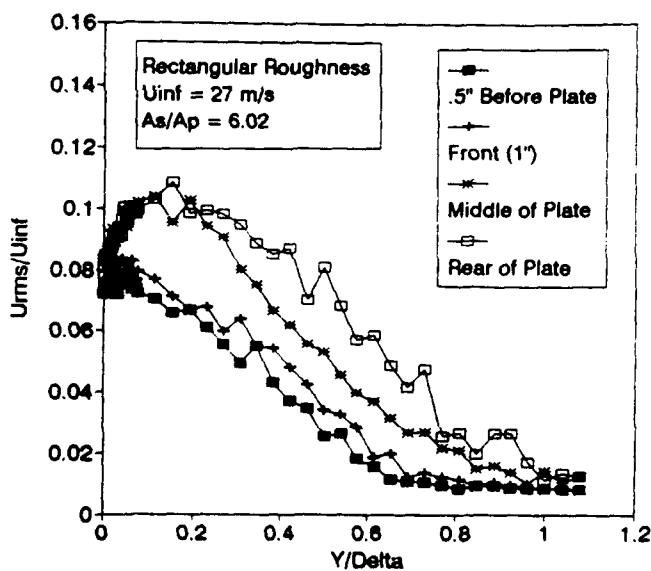


Figure 75 - Turbulence Profiles for Plate R5
with the Elements Above the Boundary Layer Plate

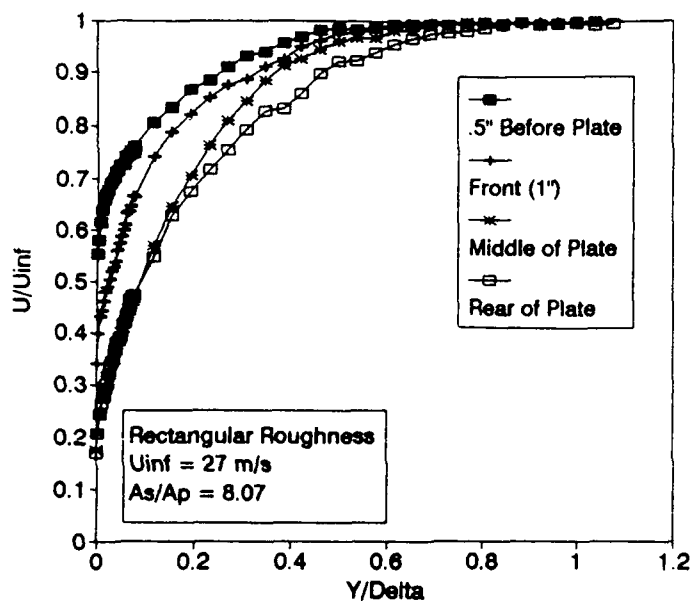


Figure 76 - Velocity Profiles for Plate R6 with the Elements Flush with the Boundary Layer Plate

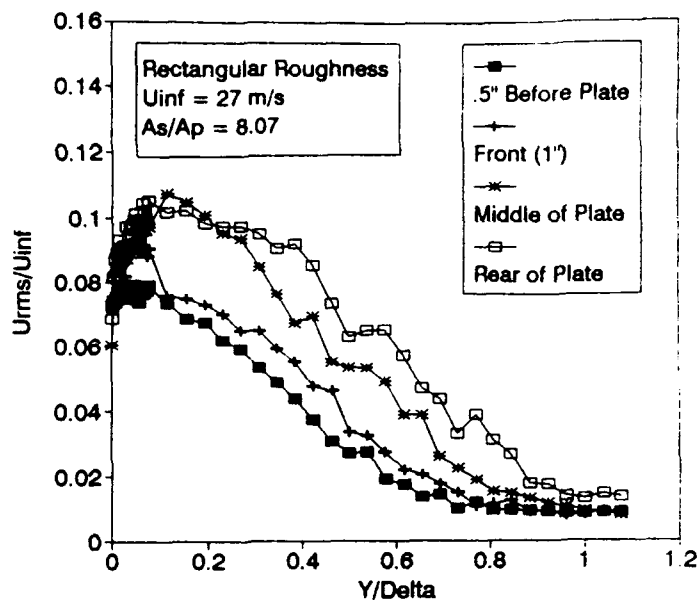


Figure 77 - Turbulence Profiles for Plate R6 with the Elements Flush with the Boundary Layer Plate

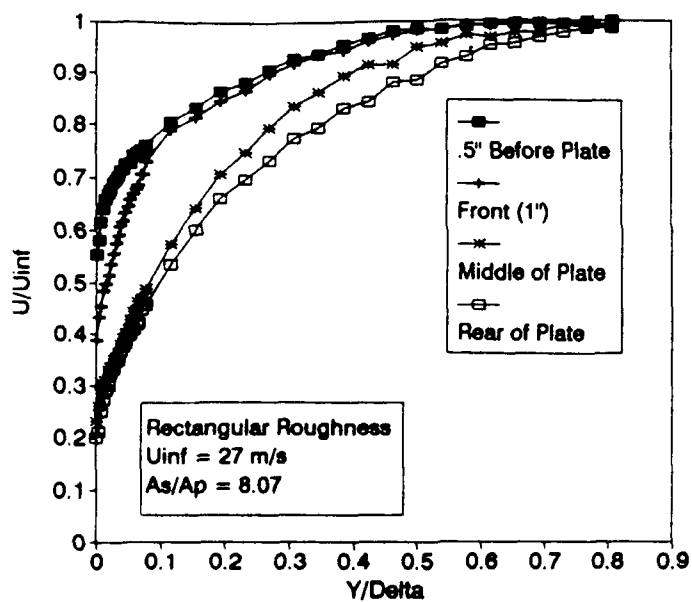


Figure 78 - Velocity Profiles for Plate R6 with the Elements Above the Boundary Layer Plate

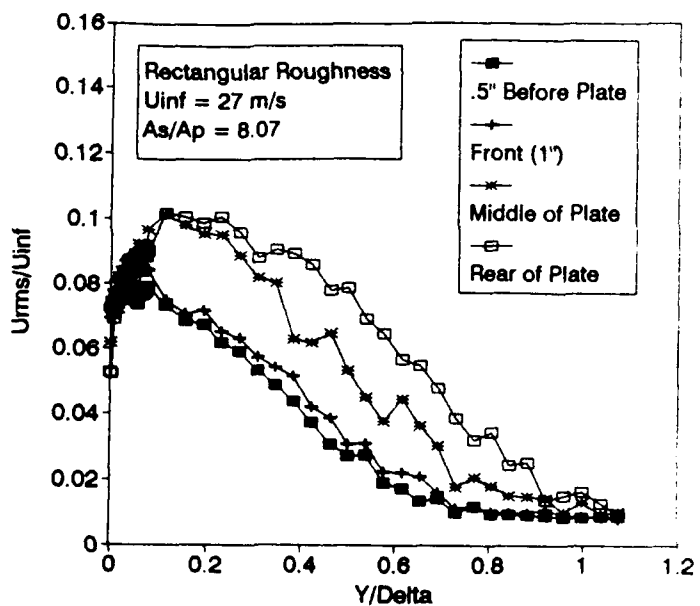


Figure 79 - Turbulence Profiles for Plate R6 with the Elements Above the Boundary Layer Plate

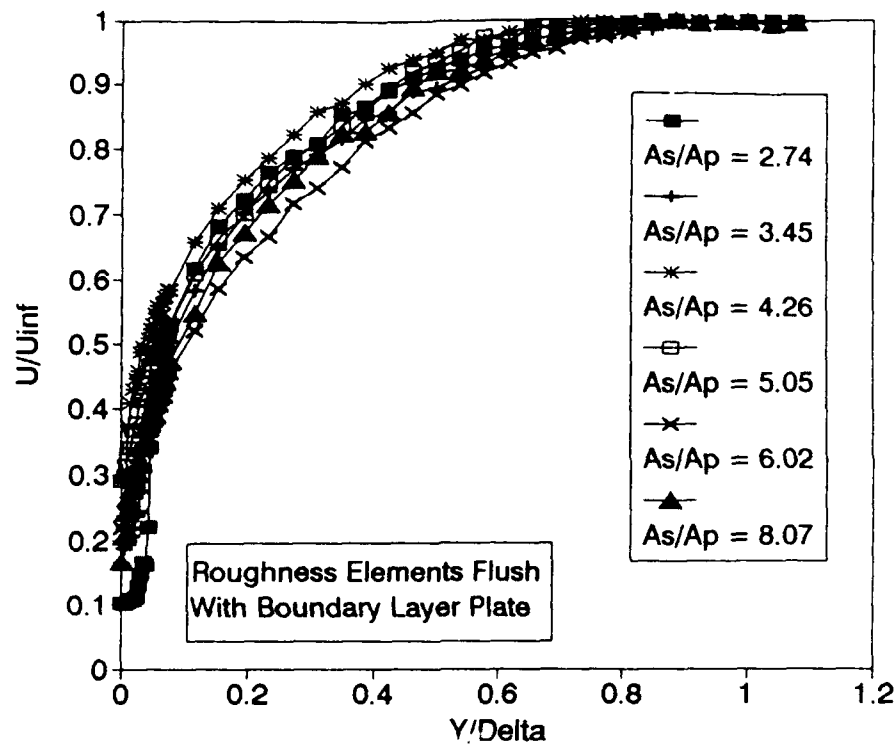


Figure 80 - Comparison of Velocity Profiles at Rear of Rectangular Roughness Plates with the Elements Flush with the Boundary Layer Plate

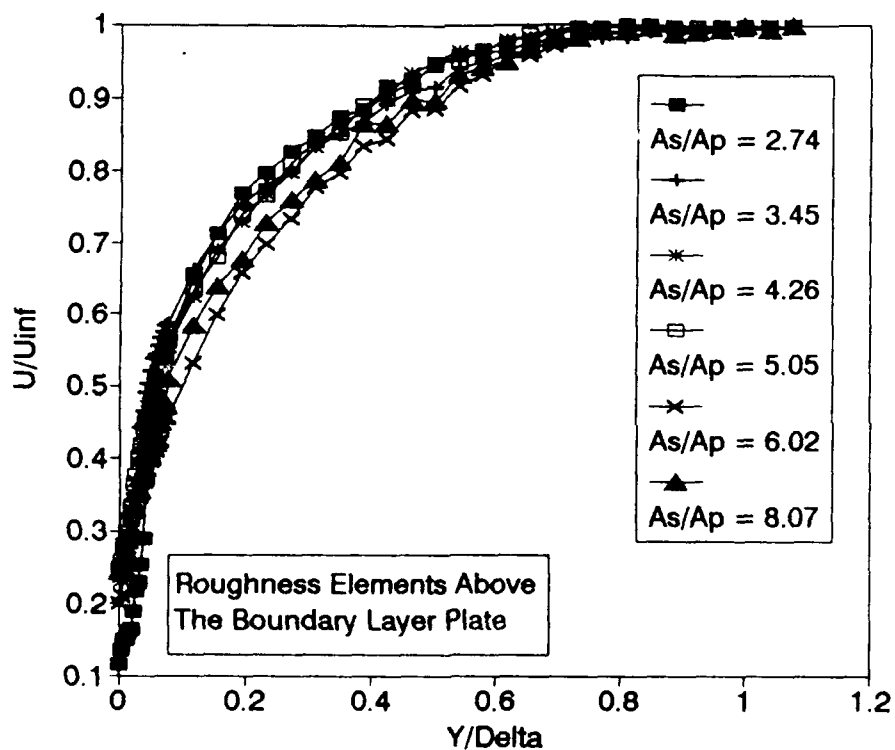


Figure 81 - Comparison of Velocity Profiles at Rear of Rectangular Roughness Plates with the Elements Above the Boundary Layer Plate

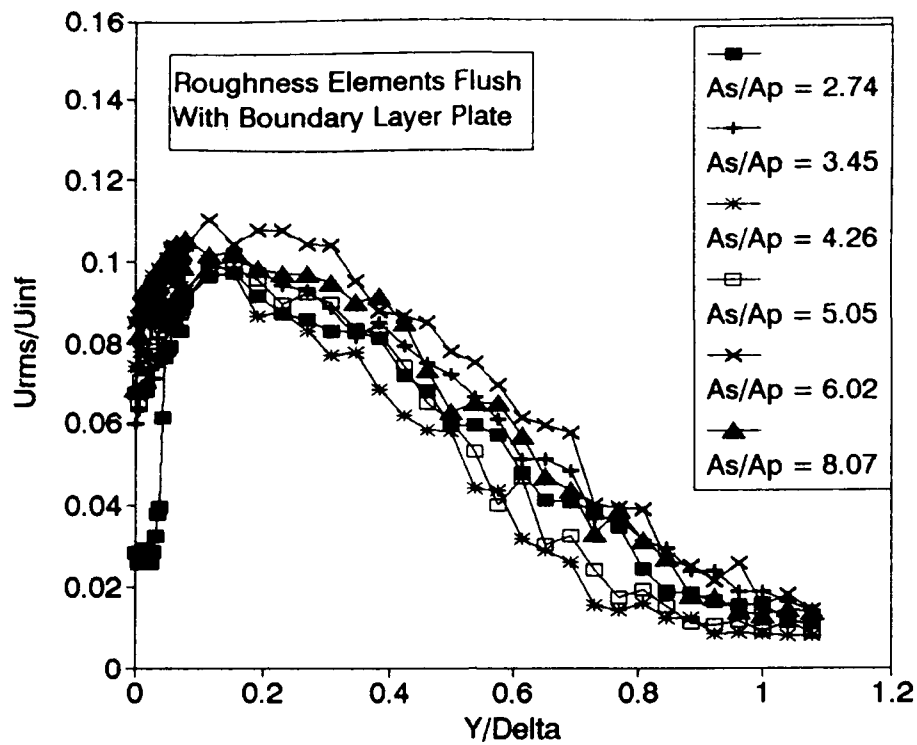


Figure 82 - Comparison of Turbulence Profiles at Rear of Rectangular Roughness Plates with the Elements Flush with the Boundary Layer Plate

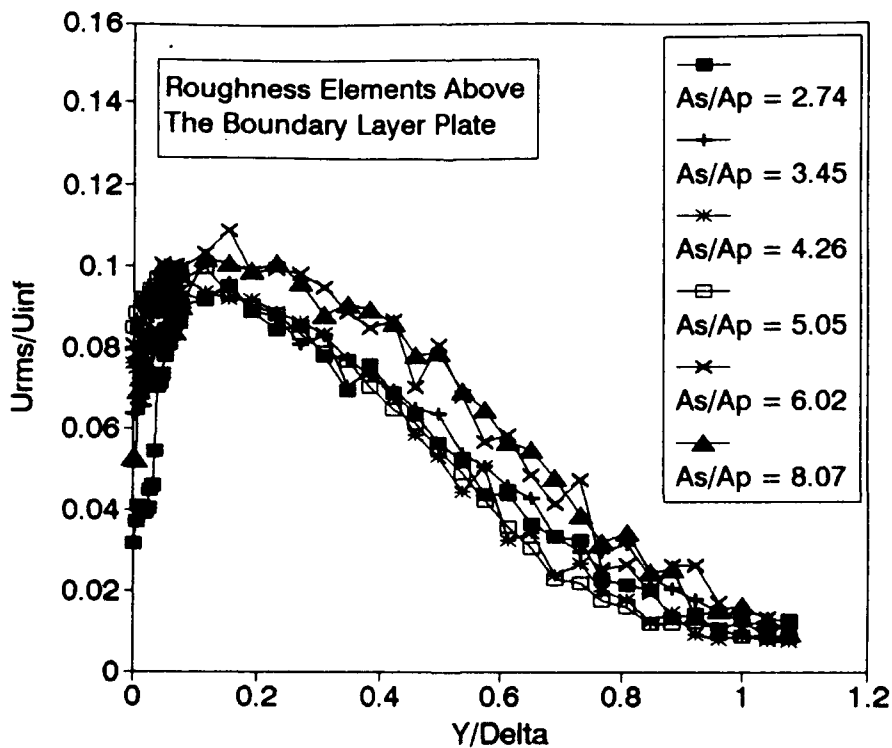


Figure 83 - Comparison of Turbulence Profiles at Rear of Rectangular Roughness Plates with the Elements Above the Boundary Layer Plate

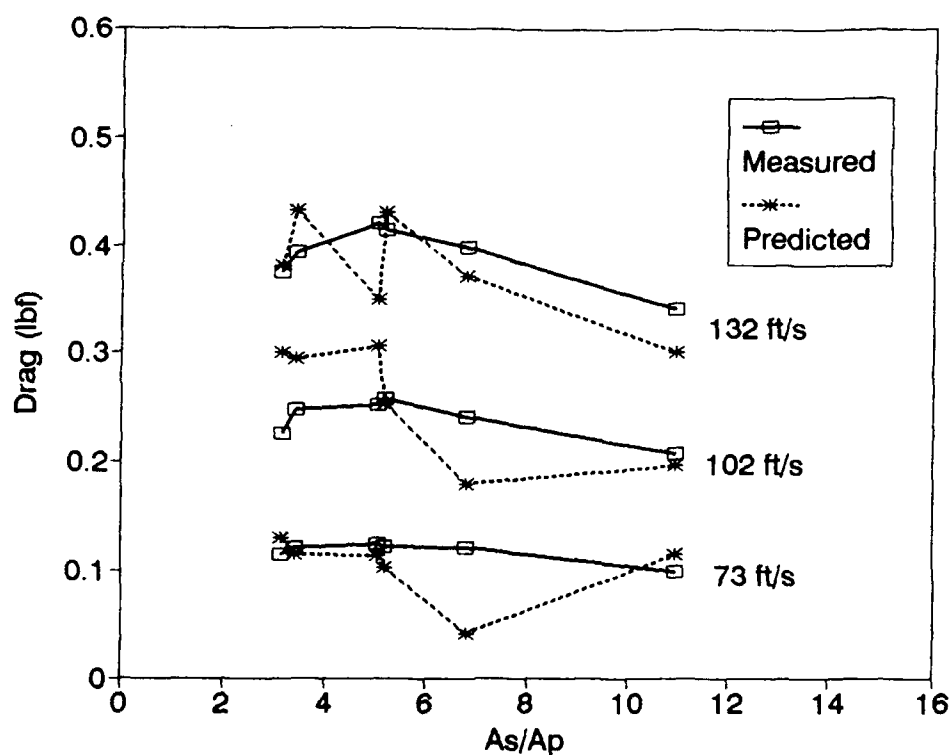


Figure 84 - Comparison of Measured and Predicted Drag Using the Original TCH C_d Correlation

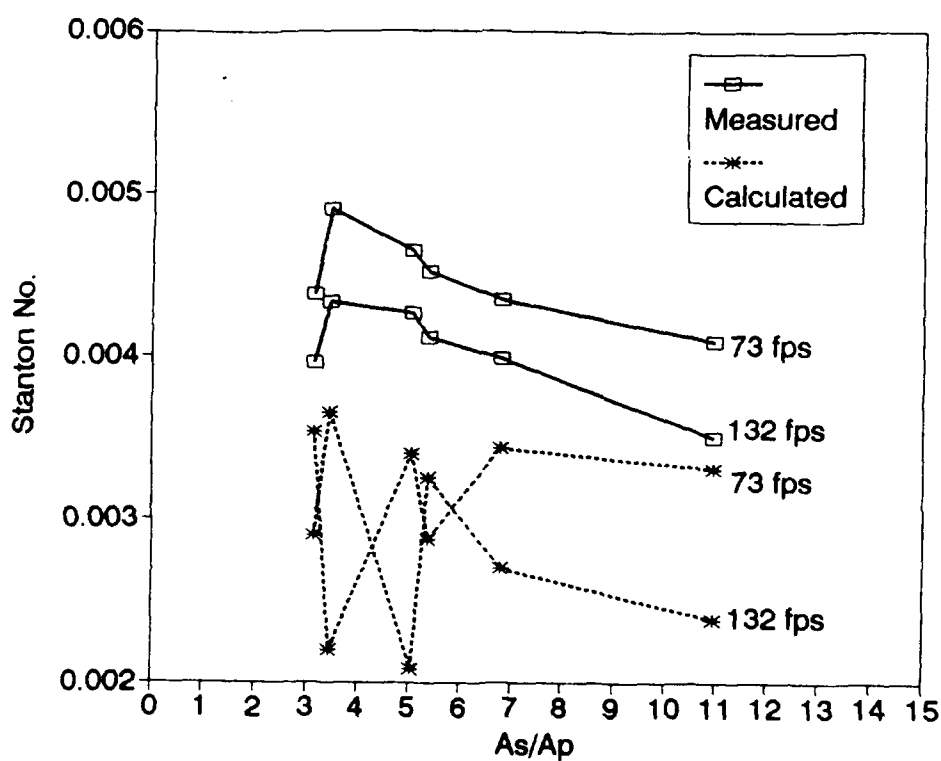


Figure 85 - Comparison of Measured and Predicted Heat Transfer Using the Original TCH Nusselt No. Correlation

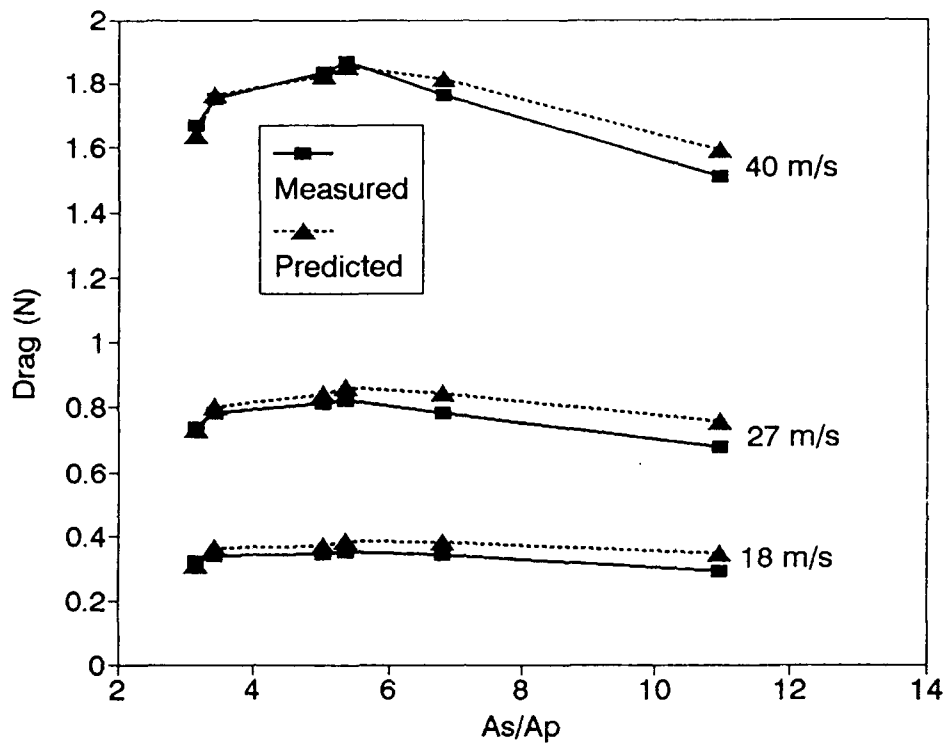


Figure 86 - Comparison of Measured and Predicted Drag Force Using Eqn (4) and Variable Initial Step Size

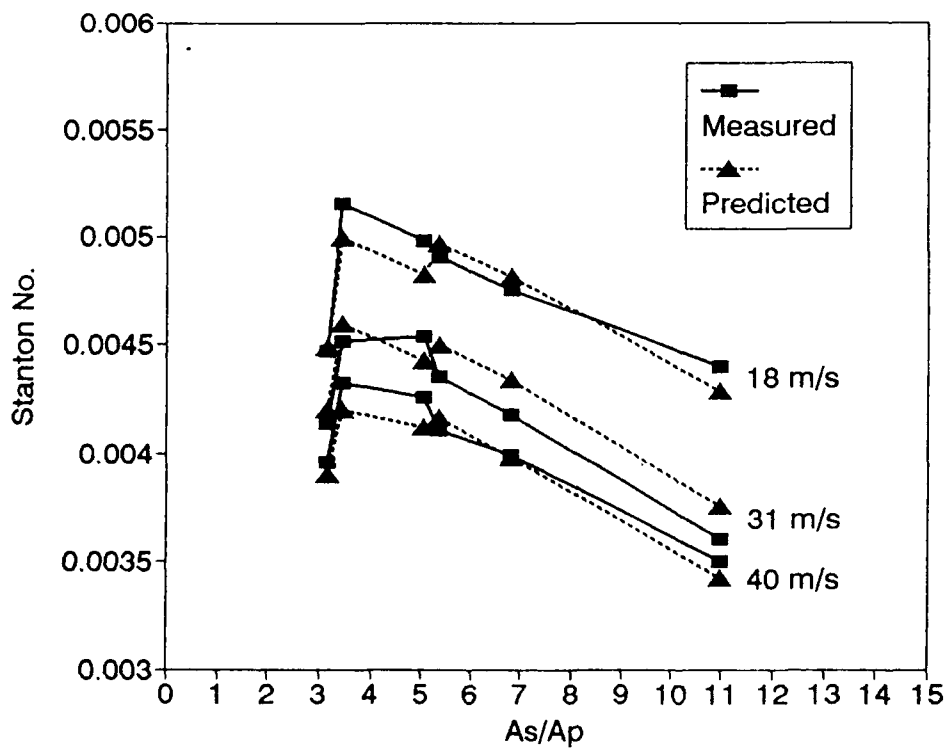


Figure 87 - Comparison of Measured and Predicted Heat Transfer Using Eqn (5) and Variable Initial Step Size

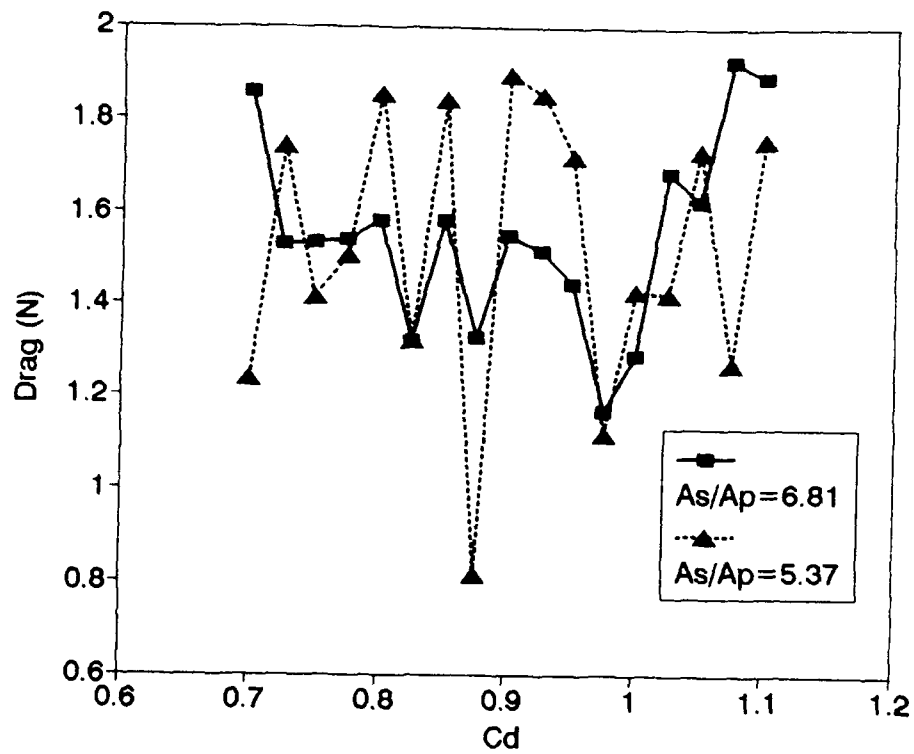


Figure 88 - Variation of Predicted Drag with Constant Cd Value

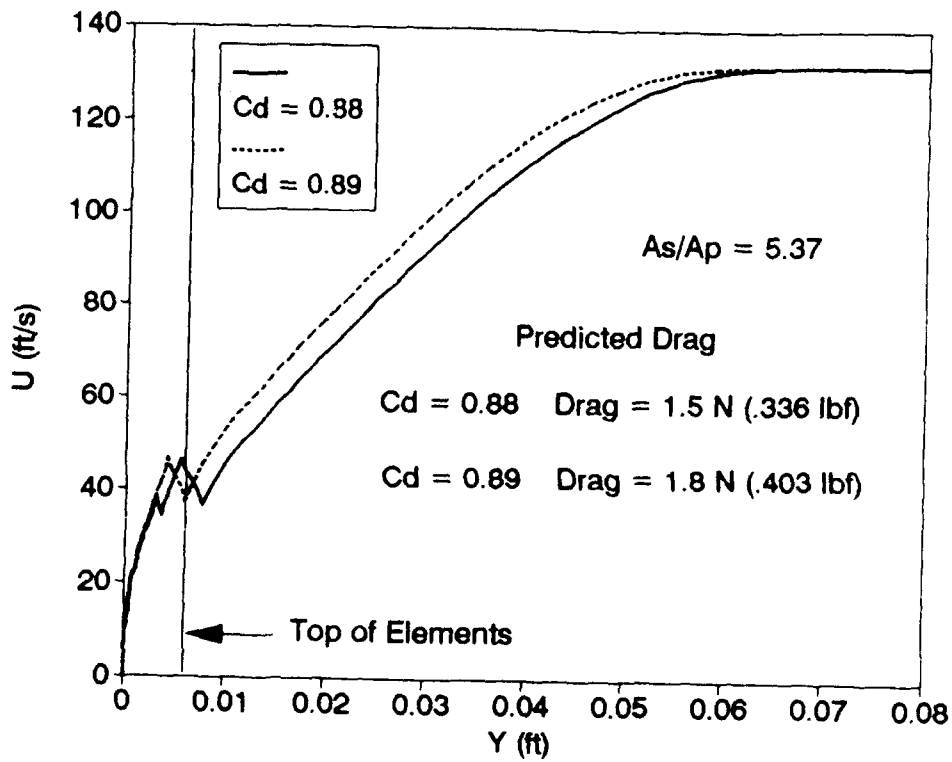


Figure 89 - Velocity Profiles Predicted with ROUGH Near Front of Plate

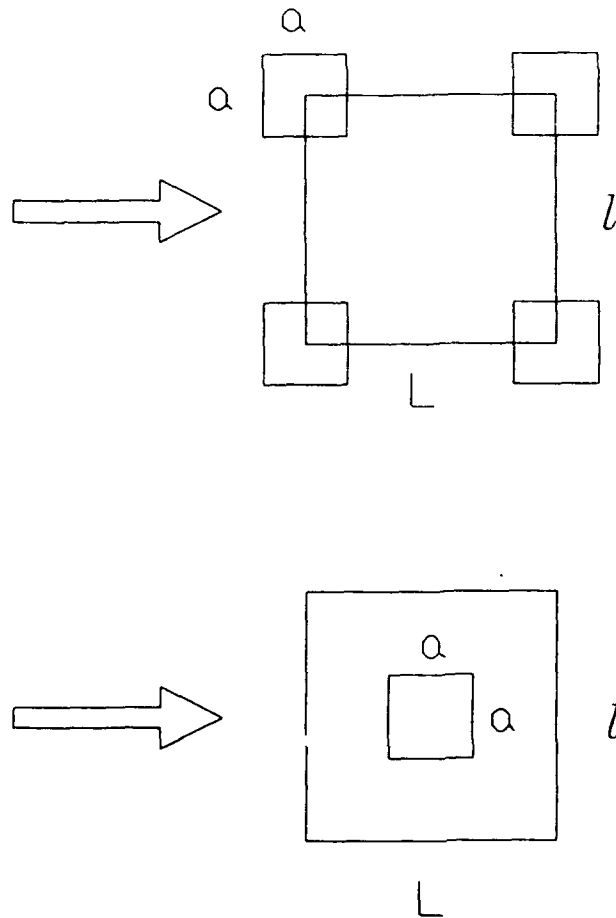


Figure 90 - Definition of Dimensions for Square Roughness Elements

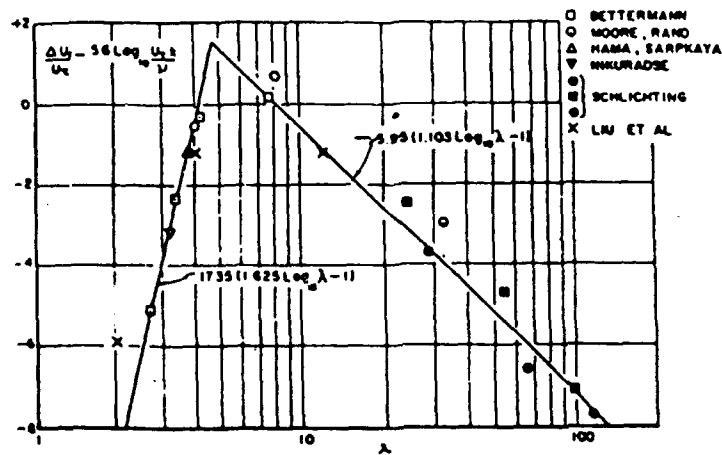


Figure A1 - The Effect of Roughness Density on the Law of the Wall Intercept. From Ref 4.

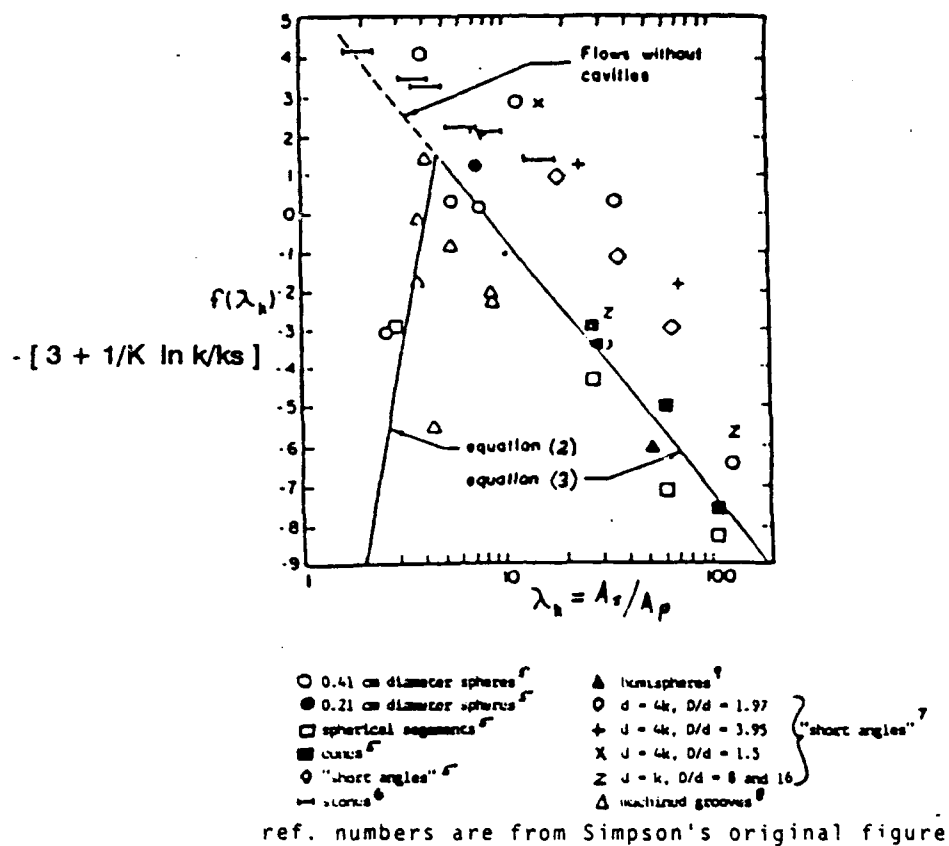


Figure A2 - Simpson's Equivalent Sand-Grain Correlation
From Ref 6.

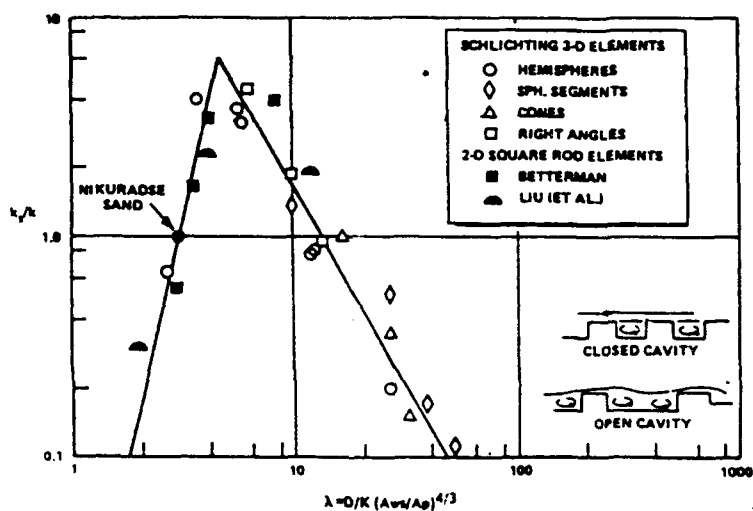


Figure A3 - Dirling's Equivalent Sand-Grain Correlation
From Ref 5.